THE HONG KONG
POLYTECHNIC UNIVERSITY
香港理工大學
Pao Yue-kong Library
包玉剛圖書館

Copyright Undertaking

CAPACITIVE DEIONIZATION OF BRACKISH WATER WITH CARBON-BASED MATERIALS

LI BEI

PhD

The Hong Kong Polytechnic University

2020

The Hong Kong Polytechnic University

Department of Electrical Engineering

Capacitive Deionization of Brackish Water with Carbon-based Materials

LI Bei

A thesis submitted in partial fulfilment of the requirements for the degree of Doctor of Philosophy

Jan 2020

CERTIFICATE OF ORIGINALITY

I hereby declare that this thesis is my own work and that, to the best of my knowledge and belief, it reproduces no material previously published or written, nor material that has been accepted for the award of any other degree or diploma, except where due acknowledgement has been made in the text.

_____ (Signed)

_____LI Bei_____ (Name of student)

Abstract

Capacitive deionization (CDI) is a novel and economical water desalination technology with merits such as energy-saving capabilities and environmental friendliness. This technology can be an alternative for traditional expensive desalination technologies and holds great promise for future applications. Through applying a voltage between two porous electrodes of a CDI cell, charged ions in water can be adsorbed because of the formation of electrical double layers; hence, the water is desalinated. One problem hindering the commercialization of this technology is the long-term operational stability of the carbon-based electrodes. To alleviate this problem, this thesis studies the underlying mechanisms behind the stability degradation. During the long-term operation of CDI cells, Faradaic reactions occur on both electrodes, and the anode is gradually oxidized. The oxidation of the anode shifts its potential of zero charge, increases its resistance, and thus is responsible for the performance degradation. Meantime, different concentrations of Na^+ and Cl^- are trapped in aged positive and negative electrodes, respectively. The trapped ions may then act as surface charges and occupy the active adsorption sites in the porous electrodes, thereby decreasing the salt adsorption capacity. A schematic illustration based on the classical Gouy–Chapman–Stern model is made to present the dynamic movement of ions near degraded electrodes, such that the performance degradation is well-understood.

Through the revealed degradation mechanisms, practical methods are explored to extend the electrode lifetime. We propose that thermal treatment can precisely remove the acidic oxygen-containing groups formed in an aged anode by modulating temperatures. Accordingly, the lost pore volume, shifted potential and the increased resistance of the

anode are recovered during the thermal treatments. As a result, the performance of the CDI cell is recovered to its initial level by optimizing the treatment temperature. The understanding of the rigorous regeneration mechanism offers insights into strategies for minimizing electrode degradation or in situ regeneration. The fabrication processes of carbon-based electrodes are also evaluated for their potential to industrial application. The fabrication processes are proven to have neglectable effect on salt adsorption capacity but have obvious effect on charge efficiency and energy consumption, in which the resistance is the determining factor. Furthermore, the performance of intercalation material (MXene) is compared with porous carbon. The studied MXene is more energy-efficient in constant current mode, although it has similar desalination capacity with carbon-based electrode. The energy-efficiency may be contributed by the ion-selectivity and high conductivity of intercalation materials. Benefit from the advance of materials, CDI technology may be further developed and stand out among various desalination technologies in the near future.

Acknowledgements

As my long research journey at HK PolyU approaches completion, I would like to thank this good university, and also the special people I encountered here.

I would like to first express my deepest gratitude to my supervisor, Dr. Steven Boles, who has guided me throughout the project. He taught me how to solve problems, for both small questions and big questions. He is always accessible and responsive when I or other groupmates need help. His patience and positive attitude give me great support and confidence during the research period. Due to his kindness, wisdom and creativity, I was fortunate to enhance both my research and life skills. Special thanks also to my co-supervisor, Dr. Po-heng Lee. He is very generous to share his ideas and provides much help to my research.

Many thanks to my dear colleagues: Ms. Sijia Ran and Mr. Tianye Zheng, not only for their inspiring discussion, suggestions and great help to my research, but also for their sincerest friendship. My research journey is full of encouragement and happiness because of their accompany. I would also like to thank my other group members: Dr. Glen Tom, Dr. Mohammed Tahmasebi and Mr. Virag Raut. They are very nice, diligent and willing to offer their help, building up a good research atmosphere in our group. I am also grateful to Dr. Koko Lam, Dr. Baojun Liu, Dr. Haibo hu, Dr. Jin Shang and Ms. Mingzhe Sun, for their kind help and support to my research work.

Lastly, I would like to thank to my dearest family, my parents (Mr. Jun Li, Mrs. Feiqiu Sun), four grandparents (Mr. and Mrs. Li, Mr. and Mrs. Sun) and boyfriend (Mr. Xin Gao). They give me best love and trust. I wish I could spend more time with them in the coming future. I love my family.

Table of Contents

Chapter III

Role of metastable-adsorbed charges in the stability degradation of carbon-based electrodes for capacitive deionization

Chapter IV

Performance recovery in degraded carbon-based electrodes for capacitive deionization

List of Figures

x

List of Tables

List of Abbreviations

AC	Activated carbon
ACF	Activated carbon fiber
BOD	Biochemical oxygen demand
BWRO	Brackish reverse osmosis
CDI	Capacitive deionization
COD	Chemical oxygen demand
CV	Cyclic voltammetry
CVD	Chemical vapor deposition
DI	Deionized water
EDL	Electric double layer
EIS	Electrochemical impedance spectroscopy
EST	Electrosorption technology
FWHM	Full width at half-maximum
GAC	Granular activated carbon
GCD	Galvanostatic charge-discharge
GCS model	Gouy-Chapman-Stern model
HK model	Horvath-Kawazoe model
IC	Ion chromatography
ICP-OES	Inductively coupled plasma optical emission spectrometry
IHP	Inner Helmholtz plane
LLNL	Lawrence livermore national laboratory
MCDI	Membrane capacitive deionization
mD model	Modified Donnan model

MED	Multiple-effect distillation
MSF	Multistage flash distillation
NMP	N-methyl pyrrolidinone
OHP	Outer Helmholtz plane
PBA	Prussian blue analogues
PVDF	Polyvinylidene Fluoride
PZC	Potential of zero charge
RO	Reverse osmosis
SAC	Salt adsorption capacity
SEM	Scanning electron microscopy
STW	Sewage treatment works
SWRO	Seawater reverse osmosis
TDS	Total dissolved solids
VC	Vapor compression
WSD	Water supplies department
XPS	X-ray photoelectron spectroscopy

Chapter I

Introduction

1.1 Water supply and drainage system in Hong Kong

1.1.1 Dual water supply system

Dual water supply system indicates that there are two separate water distribution networks employed for water supply in a city. Water in one network is strictly treated to portable standards, while water in another distribution network is poorly treated and functions as non-portable water. Non-portable water can be used for toilet flushing, fire-fighting, agricultural irrigation, etc. The main advantage of this dual water supply system is the reduction of water treatment cost as the fresh water can be very expensive in water shortage areas. This system has already been used in some costal places such as Caribbean islands, U.S. Virgin Island and Hong Kong.[1]

The dual water supply system in Hong Kong was built in the 1950's.[2] In this distribution networks, fresh water is bought from East River (Dongjiang) in Guangdong province (~4 billion HKD/year). The raw water is treated by traditional water treatment processes (mixing – coagulation – flocculation – sedimentation – filtration – disinfection), before being supplied to Hong Kong residents for daily water consumption (e.g. washing, drinking). The other water stream (seawater) is pumped from local seas and mainly used for toilet flushing. The treatment processes of seawater are much simpler, which usually comprise only screening and disinfection. As shown in Figure 1.1, red points are seafront pumping stations, from where seawater is pumped, simply treated and then transported to shaded areas as toilet flushing water. There is ~70% population in shaded area and

flushing water accounts for ~30% of total water used in Hong Kong.[3-5] After being used, these two streams of water are mixed in water treatment works which are yellow points in Figure 1.1. That means water in wastewater treatment works in shaded area is the mixture of fresh water and salt water, which is also called brackish wastewater (with moderate salinity).[6]

The dual water supply system employed in Hong Kong is estimated to be ~28% less expensive than the single fresh water system.[7] Although it saves much money, it causes some problems. On the one hand, the high salinity water causes a severe corrosion problem in sewer pipes and the leaking seawater in a building can accelerate deterioration of concrete and metal window frames.[3] To alleviate this problem, the Water Supplies Department of the Hong Kong Government (WSD) started to replace the old sewer pipes with polyethylene or polyvinyl chloride pipes for water supply system in 2000. On the other hand, the saline wastewater makes the traditional wastewater treatment process become inefficient, which is discussed in details in the following section.
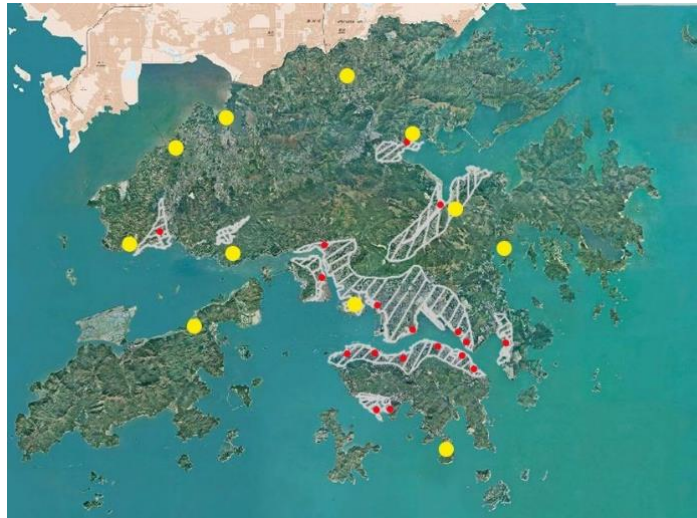
Figure 1.1 Distribution of seawater flushing areas and sewage treatment works

in HK, from ref [3, 8]

1.1.2 The effect of saline water on wastewater treatment process

At present, most sewage treatment works (STW) in Hong Kong use traditional wastewater treatment processes. One typical example is presented in Figure 1.2, which is used by Yuan Long Sewage Treatment Works.[9] The design flow of this works is 70,000 m^3/d. In preliminary treatment, relative bigger solids are removed by screening and degritting, where about 50% of suspended solids are settled out and removed as primary sludge. In this stage, the high salinity increases the amount of total suspended solids as the biodegradation of the suspended fractioned is retarded.[10] Then water is sent to secondary treatment where the growth of micro-organism (activated sludge) will assimilate pollutants in the sewage. In this stage, the biochemical oxygen demand (BOD) and chemical oxygen demand (COD) removal efficiency, and the denitrification process is not affected by the saline conditions, while the nitrification process is inhibited by the high salinity, which causes the increase of sludge age. At the last stage, treated sewage and activated sludge are separated in the final sedimentation tanks. The sludge from primary and final sedimentation is digested, dewatered and finally sent to landfill, meanwhile the treated water is discharged into nearby river. Furthermore, seawater also increases the sulphate concentration in the wastewater and causes the production of H_2S after any anaerobic processes, releasing hazardous gas to the STW.

On the other hand, considering that solids and organics in wastewater are removed during the treatment process, the effluent water is relatively cleaner and of lower salinity than seawater. Therefore, it can be a supplement of non-portable water for Hong Kong residents. The Ngong Ping Sewage Treatment Works and Shek Wu Hui Sewage Treatment Works have already built reclaimed water facility and produced recycled water

for nearby residents in recent years.[11] Further treatment processes (tertiary treatment and disinfection) and a comprehensive testing are adopted for the effluent water to ensure the safety. Moreover, Hong Kong government also tried the seawater desalination to offer fresh water but the project has not been finished for many years, which caused by many reasons such as high cost and complexity of the project.[11] This implies that cheap and simple desalination technologies/processes are needed for the water-shortage areas like Hong Kong.
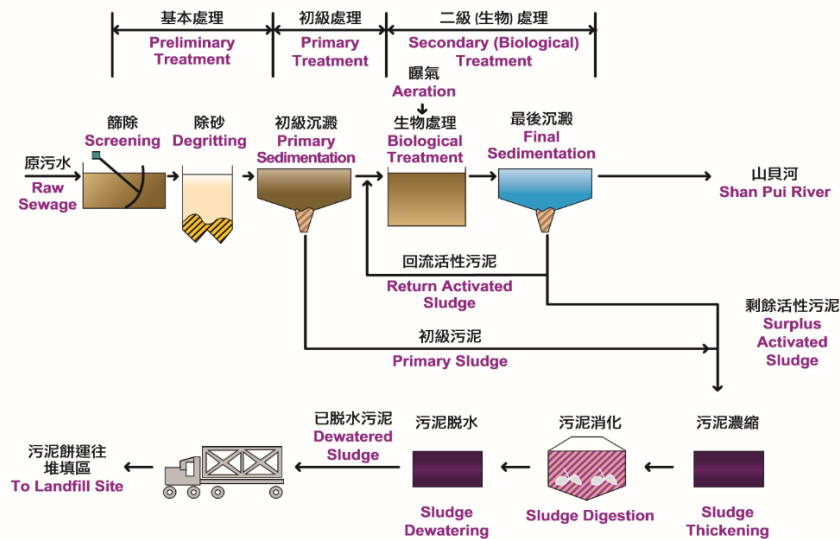
Figure 1.2 Sewage treatment process flowchart, from ref [9]

1.2 Overview of existing desalination technologies

1.2.1 Thermal evaporation

Present desalination technologies can be divided into two main categories. One is thermal evaporation method and the other is membrane separation method. Thermal evaporation methods include multistage flash distillation (MSF), multiple-effect distillation (MED) and vapor compression. Membrane separation methods consist of

reverse osmosis (RO), forward osmosis (FO), nanofiltration (NF) and so on. Other common desalination technologies are electrodialysis (ED), ion exchange, etc. Their global capacity shares are shown in figure 1.3.
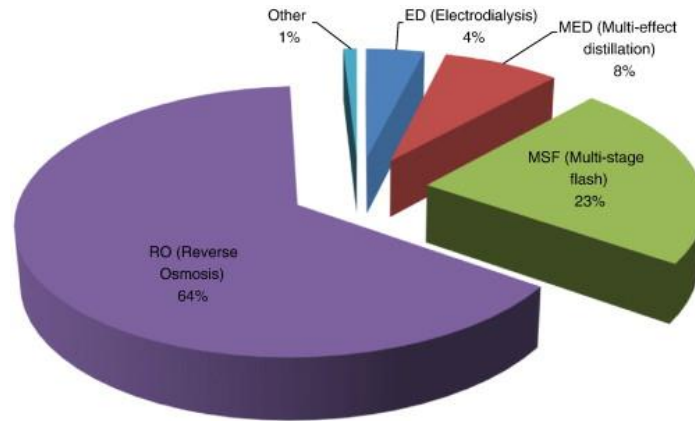
Figure 1.3 Global desalination technologies share by capacity, adapted from ref [12]

Thermal evaporation is the oldest desalination method, and its industrial application started from 1950s.[13] This technology functions based on that fresh water is heated and separated from saline water in the form of water vapor. The most popular thermal evaporation technologies are multistage flash distillation (MSF) and multiple-effect distillation (MED). MSF method comprises a series of stages, where the pressure and the temperature at each stage is lower than those at the former stage. The salt water is heated before entering the first stage. As the pressure and the temperature are lower in the first stage, the fast evaporation (flash) occurs and the vapor is collected as product (fresh water). Similarly, the fast evaporation occurs and the fresh water is produced at each following stage.[14] A typical MSF plant usually consists of 4-40 stages. As for MED, the main components in each single effect or chamber are the evaporator and the preheater (condenser).[13] The feed seawater is preheated in the condenser, then spayed at the top of

the evaporator and heated by parallel heating steam tubes. The vapor collected in the evaporator is sent back to the condenser again, and is used to heat the feed seawater and also condensed as the product. MED usually consists of 2-5 effects with successive lower pressures and temperatures, and the vapor formed in one effect is employed in the following effect to efficiently use its latent heat.[15]

Thermal evaporation plants occupy around 30 percent of world's desalination system.[6] Since the energy consumed in thermal evaporation methods is used to heat water, which is not affected by the water salinity, thermal evaporation is more efficient for treating salt water with high concentration compared with membrane methods. This is the reason why thermal treatment technologies are widely adopted by Middle Eastern countries such as Saudi Arabia, Oman, Qatar, where have some of the most saline water bodies on the planet for water supply. Furthermore, thermal evaporation can be combined with power generation that provides low-cost stream for distillation process in these countries. This combination also helps save total cost of thermal desalination.

1.2.2 Membrane separation methods

In membrane separation methods, fresh water is separated from saline water by using membrane, which only allows water molecules to go through so ions can be removed. The most widely employed membrane method is reverse osmosis (RO), which accounts for over 60% of installed capacity.[15] The development of RO is mainly based on the development of membrane. The conventional cellulose diacetate membrane was developed in 1960s, since when this technology was transferred from lab-scale to industrial process. The invention and progress of polyamide membranes with even higher

flux and salt rejection prompted RO to be gradually widely adopted in the industry since 1990s.[16] A typical RO system usually comprises 4 processes. (1) Pretreatment steps (screening, chlorination, acid treatment, filtration etc.) are employed to remove contaminants with big size such as sands, dissolved solids, and colloidal suspension. The pretreatment steps are usually complex because RO membrane is sensitive to various contaminants. (2) High pressure pumps are used to pump the pretreated water through the RO membrane, which is a noisy step and requires high mechanical strength of RO membrane. (3) In the third separation step, semipermeable RO membrane separates most salt ions from the water molecules, but some salt ions and dissolves gas still exist in produced water. (4) Post-treatment steps usually consist of pH adjustment (from acid to neutral), gas removal, remineralization etc. to finally make the produced water meet the portable standards.

The comparison of energy consumption and water production costs between thermal evaporation and RO are presented in Table 1.1. Seawater reverse osmosis (SWRO) requires much lower energy and cost than those of thermal evaporation, and the numbers for brackish reverse osmosis (BWRO) are even lower. This is the reason why RO is the most popular desalination technology. However, RO still has some limitations. Scaling problems always accompany with membrane separation, affecting its productivity. RO process also has less effectiveness to remove Boron. This limitation requires the extra treatment process for Boron removal. Furthermore, the brine produced by RO process is hard to tackle and may causes environmental problems.

Table 1.1 Energy and water production costs for desalination technologies, from ref [6]

Energy Type	MED	MSF	VC	BWRO	SWRO
Steam pressure, ata	0.2–0.4	2.5–3.5	Not needed	Not needed	Not needed
Electric energy equivalent, kWh/m³ (kWh/1000 gal)	4.5–6.0 (17.0–22.7)	9.5–11.0 (35.9–41.6)	NA	NA	NA
Electricity consumption, kWh/m³ (kWh/1000 gal)	1.2–1.8 (4.5–6.8)	3.2–4.0 (12.1–15.1)	8.0–12.0 (30.3–45.4)	0.3–2.8 (1.1–10.6)	2.5–4.0 (9.5–15.1)
Total energy use, kWh/m³ (kWh/1000 gal)	5.7–7.8 (21.5–29.5)	12.7–15.0 (48.0–56.7)	8.0–12.0 (30.3–45.4)	0.3–2.8 (1.1–10.6)	2.5–4.0 (9.5–15.1)
Water production costs, US$ per cubic meter (US$ per 1000 gal)	0.7–3.5 (2.6–13.2)	0.9–4.0 (3.4–15.1)	1.0–3.5 (3.8–13.2)	0.2–1.8 (0.8–6.8)	0.5–3.0 (1.9–11.3)

Note: NA=Not applicable. BW=brackish water, SW=sea water, VC=vapor compression

Although RO has limitations, it is still the most advanced desalination technology around the world. Due to the advances of RO, Hong Kong government has also been attempted to employ this technology for water desalination since 2003 to decrease their reliance on East River. The Water Supplies Department of the Hong Kong Government (WSD) conducted a two-years pilot plant study of RO technology at two separate locations (Tuen Mun and Ap Lei Chau) from later 2004 to early 2007. Although the pretreatment systems met the minimum objectives, they still faced problems such as irreversible membrane fouling.[17] WSD keeps investigating RO technology in recent years,[18] and started Tseung Kwan O Desalination Plant Project last year (2019),[19] even though the predicted cost of RO water is higher than that of the water from East River. This implies that although RO is mature and widely employed, it is still an expensive and complex desalination technology, which have not been employed successfully in Hong Kong with several trials. The exploration of novel and cheap desalination technology is important for water-shortage cities just like Hong Kong.

1.3 Capacitive deionization technology

1.3.1 Brief introduction

Apart from abovementioned two main kinds of traditional desalination methods, capacitive deionization (CDI) is a novel, promising and membrane free desalination method. Capacitive deionization technology started from 1960s when the concept was first proposed by Caudle et al.[20] and then it developed slowly in the later four decades. The interest of this technology resumed in the beginning of 21st century, since when the number of related publications has increased remarkably[21-23] and several companies started to sell their CDI products.[24, 25] CDI consists of two processes, as shown in figure 1.4: charging phase for purification and discharging phase for electrodes regeneration. In the charging phase, two electrodes are polarized by applying the voltage (0.8-1.2 V), so cations and anions can be adsorbed by two oppositely charged electrodes respectively and the water can be desalinated. Usually, charging phase ends when electrode's surface is fully occupied by salt ions. In discharging phase, another stream (discharge water) is used and the electrodes are short-circuited. In this case, ions adsorbed in the charging phase can release from electrode into the bulk fluid, thereby the electrodes are regenerated. Carbon-based materials with high salt adsorption capacity (SAC) are usually employed as electrodes. Since both the working principle and electrode materials of CDI technology are similar with those of supercapacitor technology, the developments in supercapacitor offer many references for CDI technology.
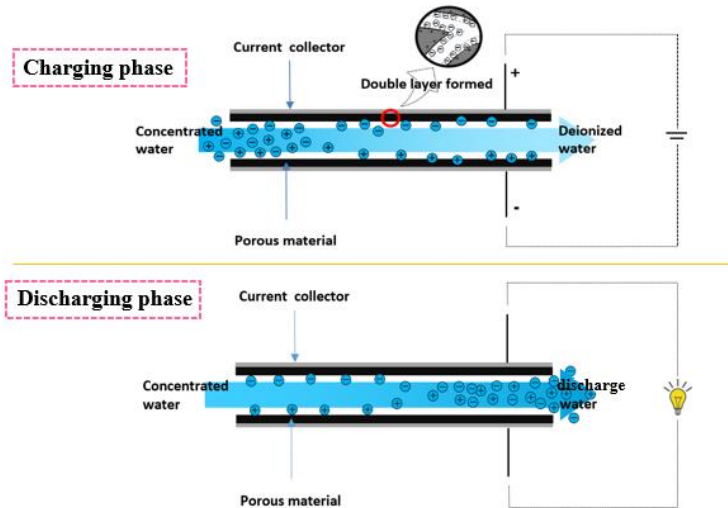
Figure 1.4 Schematic illustration of capacitive deionization technology

Compared to RO, CDI extracts ions from water rather than pushes all water molecules go through the membrane. Theoretically, the energy consumption of RO is a constant as a function of salt concentration, while that of CDI is proportional to salt concentration, as shown in figure 1.5. Compared with RO, CDI is more energy efficiency in desalinating brackish or water with low salinity, with the energy consumption of around 0.1-1 kWh/m^3.[26-29] Furthermore, CDI can work without membrane, so membrane fouling problem can be avoided. Another merit of CDI is that the concentration of produced water can be tunable, with the lowest concentration of drinking water level.[30] Since CDI is energy-saving and environmentally friendly, it holds great promise to share more desalination market in the future. This technology is also promising to be employed in Hong Kong. One example is to recycle the brackish wastewater, providing low-cost freshwater supplement to HK residents.
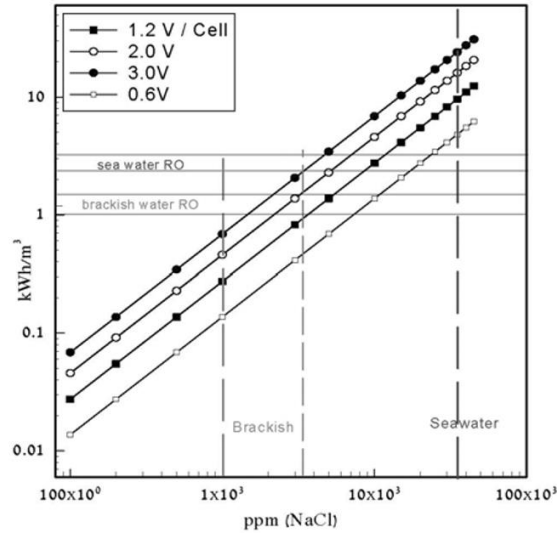
Figure 1.5 Specific energy consumption for CDI as a function of NaCl concentration and for different voltages, as compared with brackish and seawater RO desalination, from ref [25]

1.3.2 State-of-the-art of capacitive deionization technology

To date, some big research groups (Michael Stadermann et al. in USA, Doron Aurbach et al. in Israel, P.M. and Biesheuvel in The Netherlands etc.) have built big CDI modules, focusing on performance and operation study. Most other research groups study CDI technology in a lab scale, focusing on electrode materials, cell architecture, modelling, working mechanism and so forth.

CDI architectures have been developed rapidly over last two decades. As shown in figure 1.6a, the typical CDI architecture is very simple, consisting of a pair of electrodes separated by a spacer where feed water flows. This architecture is called "flow-by" or "flow-between" and is suitable for investigating novel materials or performing basic studies.[31, 32] On the condition that the feed flow is pumped perpendicularly through the electrodes, the architecture is so-called "flow-through" (figure 1.6b), which has faster

11

desalinating rate and also requires higher pressure input compared with flow-by cell.[33] Some CDI systems also employ ion exchange membranes placed in front of the electrodes and this is called membrane CDI (MCDI), as illustrated in figure 1.6c.[34, 35] Membrane improves the selectivity of electrodes, thereby giving rise to the charge efficiency. However, the employment of membrane increases the cost and may introduce membrane fouling problem. Furthermore, the inverted CDI (i-CDI) is proposed by Gao Xin et al,[36, 37] who modified the anode with negative charges via chemical surface treatment, causing that cell desalination occurs at discharging phase while electrode regeneration is at charging phase (figure 1.6d). This operation method contributes to a much better stability of electrodes, but its desalination capacity is relatively low. Moreover, hybrid CDI system combines a battery electrode and a capacitive electrode (figure 1.6e). By employing battery electrode, CDI cell is able to reach a high desalination ability and a high selectivity. However, battery electrode usually faces stability problem and is more expensive than capacitive electrode. Battery electrode can also be employed for both electrodes of CDI cell, which is called desalination battery (figure 1.6f). The desalination capacity of this battery architecture is even higher. All above architectures can be classified as static electrode architecture. The other popular architecture is flow-electrode CDI (FCDI), which uses flowing slurry electrodes and can be continuously operated, as shown in figure 1.6g.[38, 39] This system has an advantage of continuity and a disadvantage of low charge efficiency. The low charge efficiency is caused by the high resistance of flowing electrode. All these architectures show their unique properties, providing many selections for CDI applications.
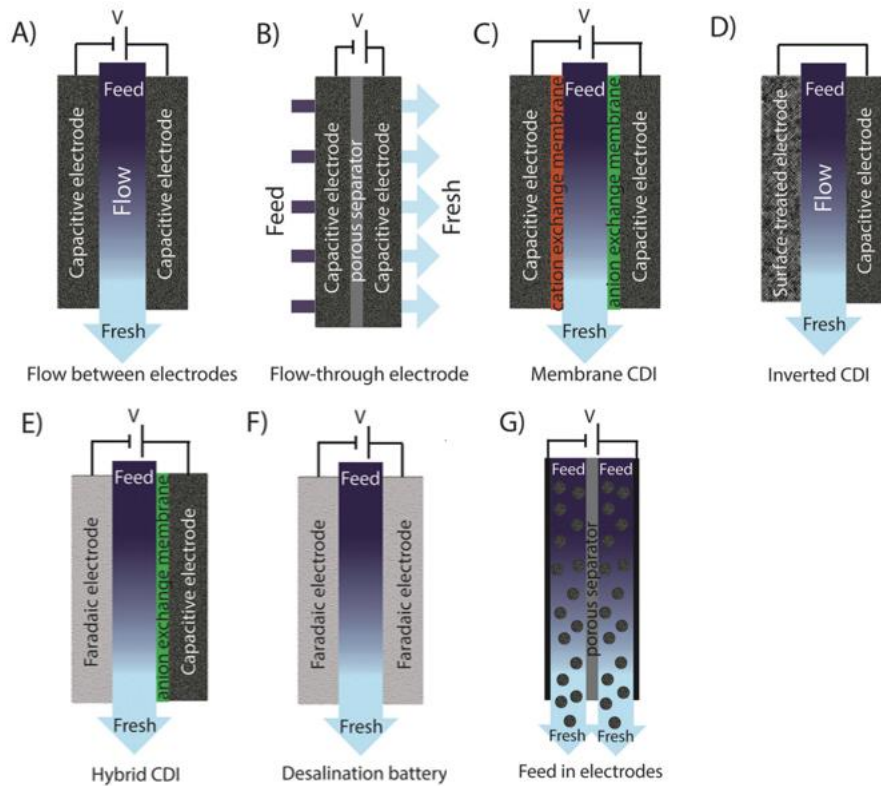
Figure 1.6 Typical cell architectures of CDI: (a) flow-by CDI, (b) flow-through CDI, (c) membrane CDI, (d) inverted CDI, (e) Hybrid CDI (f) desalination battery, and (g) flow-electrode CDI, from ref [27]

The materials for CDI electrode can be divided into two main categories. One is conventional carbon-based materials and the other is battery electrodes. Since carbon-based materials function based on the formation of electric double layer (EDL), the key properties influencing performance include but are not limited to (1) high surface area (the capacity is proportional to surface area according to EDL theory), (2) high conductivity (to decrease resistance loss) and (3) high stability (to ensure the working lifetime). Commercial activated carbon is the most widely used electrode material because it is economic and well-understood.[40-42] Compared to activated carbon, activated carbon

fiber has finer pore structure and higher price, and also be studied thoroughly.[43, 44] Other advanced carbon-based materials are carbon aerogels,[45, 46] carbide-derived carbon,[47] graphene,[48, 49] ordered mesoporous carbons,[50, 51] carbon nanotube[52] and so on. Those carbon-based materials have differences in properties such as pore structure, carbon density, and conductivity. Carbon electrodes usually have salt adsorption capacity (SAC) between 4-15 mg/g, as shown in figure 1.7. Unlike carbon-based materials, battery electrodes work based on the Faradaic reactions with specific ions (Na^+ or Cl^-), thereby removing these specific ions from water. One typical example is the work done by Fuming chen et al.[53] who use $BiOCl$ for Cl^- adsorption and $Na_{0.44}MnO_2$ for Na^+ adsorption, achieving the SAC and charge efficiency as high as 68.5 mg g^{-1} and 0.977, respectively. Other battery electrodes such as $Na_4Mn_9O_{18}$ (metal oxides), [54] $Ag/AgCl$,[55] NiHCF (Prussian blue analogs)[56, 57] and MXenes[58, 59] have also shown their desalination potential. The maximum desalination capacities achieved by various kinds of materials are illustrated in figure 1.7. Although the SACs of battery electrodes are usually higher than those of carbon electrodes, the stability of battery electrodes is lower and the price is higher. On the other hand, carbon-based electrode and battery electrode can be combined as composite electrode, which also show good performance (~15 mg/g SAC).[60] At this stage, only carbon-based materials are commercialized for CDI technology, while most novel materials are still being studied in the research. As for the performance metrics, aside from SAC, average salt adsorption rate (ASAR) also needs to be considered during the operation. Usually, the Kim-Yoon plot (similar to Ragone plot used in supercapacitor) is referred. As shown in Figure 1.8, the operational optimum should be achieved at high (but not the highest) values of both ASAR and SAC.
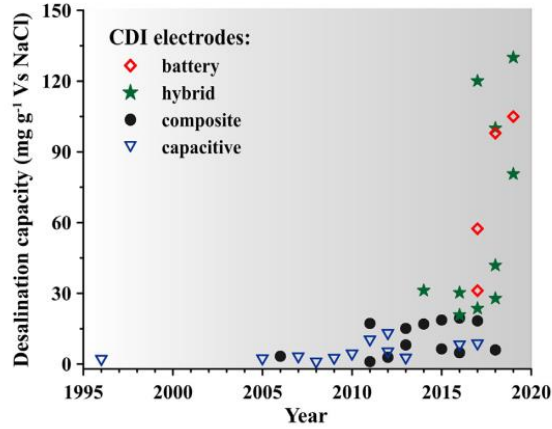
Figure 1.7 Historical evolution of maximum desalination capacity for capacitive,

composite, hybrid and battery electrode, from ref [61]
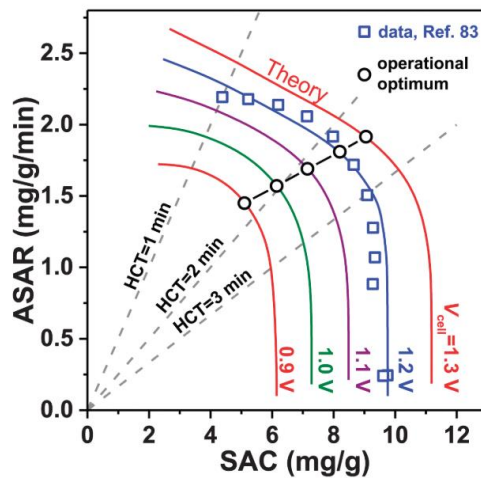
Figure 1.8 Kim–Yoon plot for average salt adsorption rate (ASAR) in a flow-by CDI

cell with static film electrodes vs. the salt adsorption capacity (SAC) as function of

charging voltage, from ref [27]

In research work, two operation modes are commonly employed, namely batch mode

and single-pass mode. Their layout (especially the location of the conductivity meter) for

a CDI experiment is different. In single-pass experiments (Figure 1.9a), a large water

reservoir is used (usually larger than 1L) and the concentration of inflow is constant. After the water passing the CDI cell, the outflow is discarded, or recycled to the large feed water reservoir. In the latter case, since the reservoir is large enough, its concentration can still be viewed as constant. The effluent conductivity is measured directly at the exit of the CDI cell. The calculation of SAC needs to integrate the effluent concentration vs. time data. Different from single-pass experiments, the water is recycled between reservoir and CDI cell in the batch-mode method (Figure 1.9b). The conductivity is measured in the recycling reservoir (small beaker). Since the water reservoir is small enough, the variation of its salt concentration caused by the outflow can be tracked. The measured conductivity is the mixture of outflow and reservoir water. The calculation of SAC in batch-mode is simpler, where salt amount decreased in the reservoir equals to the salt amount adsorbed by the CDI cell. In comparison, batch mode is simpler and easier, while single-pass mode can provide more data information for a single charging/discharging cycle. Both of these modes are widely employed and can satisfy most research purposes.
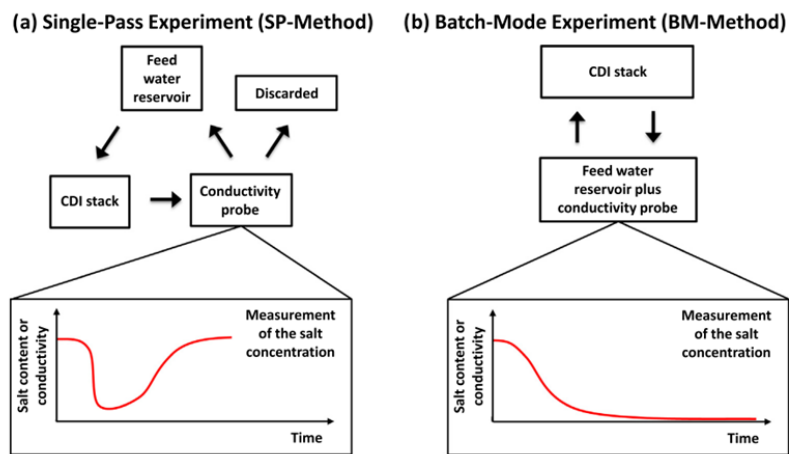
Figure 1.9 Schematic illustration of two designs for CDI experiments. (a) Single-pass experiment. (b) Batch-mode experiment (BM-method), from ref [62]

16

1.3.3 Limitations

Although CDI is a promising desalination technology, it still has some limitations. (1) Compared with RO, CDI is only more efficient in treating brackish water and is inefficient in treating seawater, as shown in Figure 1.5. This means that the TDS of feed water to CDI should be less than 2000 ppm. This precondition limits the application of CDI technology, with the targeted water such as rainwater, domestic water, industrial water and wastewater etc. (2) Based on the desalination mechanisms of CDI, this technology can only remove charged species in water. Unlike RO or thermal desalination methods, it is difficult for CDI to remove uncharged but common contaminates such as organics, bacteria, neutral particles and so on. In the case that the requirement of produced water is high, some pretreatment or posttreatment processes are required. (3) The performance of CDI is limited by the electrode materials. Carbon-based materials are the most promising materials for CDI commercialization, but their theoretical SAC is only around 4-15 mg/g (as shown in Figure 1.7). Although battery electrodes have higher SAC, their poor stability hinders their industrialization. In addition, the achieved maximum average salt adsorption rate (ASAR) of CDI cell is ~2.5 mg/g/min. To summarize, CDI has its own advantages and limitations. The application of CDI technology depends on the real water situation and the overall water treatment process.

1.3.4 Commercial application of CDI technology

1.3.4.1 Voltea company, Netherlands

Voltea company is found by Bert van der Wal and Hank Reinhoudt in 2006, selling membrane capacitive deionization (MCDI) module globally. Their MCDI (named

"CapDI") module consists of parallel carbon-based electrodes and aims to remove the total dissolved solids (TDS) from brackish water. CapDI module has different configurations and sizes, aiming at various scales and categories of targeted water. For example, the "CapDI DiEntry" module can achieve the performance of: produced flow rate 2-12 L/min, salt removal 20-90%, water recovery 40-90% and energy consumption 0.4-0.8 kWh/m^3, with the feed water properties of TDS ≤ 2000 ppm and prefiltration of 5 µm.[63] Furthermore, the CapDI module uses acid to clean the facility after a certain period of operation.

Voltea's CapDI modules have been employed for several different applications.[63] One typical example is for irrigation in agriculture and horticulture. In Mexico, agriculture accounts for 77% of the total water consumption. The big consumption of water makes the water salinity and price are gradually high. Voltea provided their CapDI system to a tomato grower in Mexico. Since tomato is sensitive to water salinity and CapDI functions in decreasing TDS of irrigation water, the tomato's field is promoted. Furthermore, their CapDI has tunable salt removal capacity, fitting the different sodium levels required by each particular crop such as peppers and berries, who are also sensitive to salinity. Another application of Voltea's CapDI is commercial laundry, where high temperature water is employed. Since RO is sensitive to high temperature, the extra steps (cool and reheat) are needed if RO is used. CapDI do not have much limitations and recovers up to 95% of the treated water at high temperature (60℃). Moreover, CapDI also shows its strength for water softening, wastewater reuse and so forth. Due to the advantages of CDI technology and successful operation of the company, Voltea company has expanded and opened an advanced robotic production facility in Texas in 2016 for automatically

producing their CDI modules. Voltea's global commercial growth implies that CDI technology is gradually competing with other desalination technology in the market.

1.3.4.2 EST company, China

EST (Electrosorption technology) company is found by Sun Xiaowei in 2001, who studied CDI technology and graduated from Michigan Technological University in 1990s. His company have studied CDI technology for nearly 20 year and updated their CDI module for over 7 generations until now. They have installed more than 30 industrial systems in mainland China, including applications in treating municipal groundwater and petrochemical industry wastewater.[64]

The process of their CDI (namely, EST) technology is shown in Figure 1.10. Generally, the pretreatment process of CDI is simpler than that of RO, only including biochemical treatment and filtration processes. This is because that CDI module can tolerant more kinds of contaminants while RO membrane is sensitive to oil or big particles. In the next step, two CDI (EST) modules are employed so that high water recovery can be achieved. Furthermore, thermal treatment (MED) is used to treat concentrated water, and thereby solids are separated from the concentrated water and the condensed water from water vapor can be further reused. There is no discharge water of the whole process due to the employment of thermal treatment. The cycle performance of their CDI module is: salt removal 50-98%, water recovery 80-98% and energy consumption 0.3-6 kWh/m^3. The feed water requires TDS $\leq$ 4000 ppm and COD $\leq$ 100 mg/L. The lifetime of their CDI module is more than 5 years. They also use chemicals to clean the aged electrode after a certain period of operation. Furthermore, the reported cost for produced water is 0.5-1.75 RMB/m^3, which is very competitive. The excellent performance may be also

caused by that their CDI module is actually the combination of CDI and ED technologies, which is not mentioned in their website but claimed by Xiaowei Sun in 2019 CDI international conference.[65]
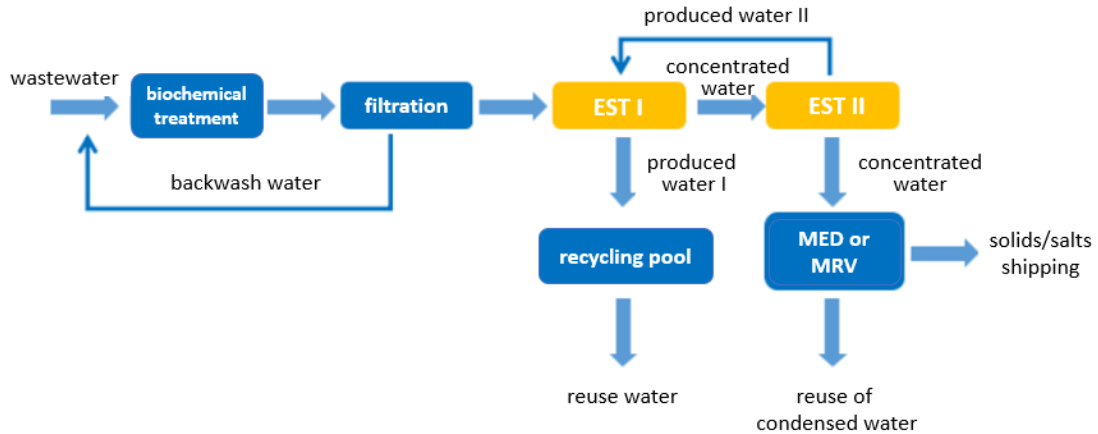
Note: MED = multiple-effect distillation, MRV = mechanical vapor recompression

Figure 1.10 EST module treatment process, from ref [64].

Although the specific materials and structures of CDI module used by Voltea and EST companies are unknown to the public, the success of these two companies gives confidence to the CDI community that CDI technology can be commercially used in treating various of water and indeed saves energy/cost compared to other desalination methods. Therefore, CDI technology hold great promise to be employed in Hong Kong (reclaim wastewater, rainwater, domestic water and so forth). As it is still a young technology and only has limited application information, it deserves to be further explored.

1.4 Motivations and importance

Since the emergence of this technology in the 1960s, most research has focused on improving salt adsorption capacity (SAC) of electrodes by exploring novel electrode materials or cell architectures.[48, 60, 66] Aside from SAC, the long-term stability is the other essential factor that determines the success of future realization, implementation, and commercialization. However, the study regarding to the mechanism of stability degradation is insufficient. Current study mainly focuses on Faradaic reactions: Carbon oxidation reactions occur on the anode during cycling, causing properties (pore volume decrease, surface area decrease, etc.) degradation of the anode.[67, 68] Meantime, oxygen reduction reactions occur on the cathode, leading to the fluctuation of dissolved oxygen (DO) concentration and pH value.[69] To make supplementary to the current stability study, this thesis aims to explore the effect of trapped salt ions on CDI stability. Salt ions carry charges and are the main composition inside the CDI cell. Therefore, it is necessary to explore their interaction with aged electrode and to clearly elaborate their effect on stability degradation during cycling.

Furthermore, there are several methods adopted by researchers to extend the lifetime of CDI electrodes at this stage. The most commonly-used method is to employ ion-exchange membrane in front of electrodes, such that the oxygen is limited to contact electrodes and unexpected Faradaic reactions can be avoided.[70] Another popular method in the lab research is to pump N_2 into the reservoir continuously during the CDI operation, so that dissolved O_2 can be removed.[68] In addition, acid is used to remove foulant from the electrodes after a certain time of operation in the industry.[63, 71] However, although these methods are able to extend the lifetime of the electrodes to some extent, the

electrodes will degrade and lose their SACs eventually due to irreversible carbon oxidation. Therefore, it is essential to study the regeneration methods. This thesis is the first to demonstrate that the degraded performance of aged electrodes can be recovered through an industrially scalable method: thermal treatment. Moreover, the regeneration mechanism is well-elaborated. The study of regeneration methods can not only enhance the comprehension of CDI technology, but also provide technical support to CDI industrial application.

On the other hand, novel electrode materials are always hot spots and various advanced electrode materials have been developed in recent decades. Although standard performance metrics have been established, it still lacks of accuracy when comparing different materials among different study as their operation parameters are different.[62, 72] Therefore, it is necessary to compare typical electrode materials under same operation conditions. Among carbon-based materials, both activated carbon (AC) and activated carbon fiber (ACF) are widely employed as CDI electrodes.[73, 74] Activated carbon electrode is very thin and conductive as it is made in slurry form, while activated carbon fiber electrode has the advantage of freestanding. Although they are both popular, there lacks of direct comparison between these two conventional materials. Furthermore, MXenes gain much attention recently as a novel intercalation material, which has excellent conductivity and high capacitance. It is of interest to compare advanced intercalation materials and traditional carbon materials under same conditions. Therefore, two groups of materials (AC vs. ACF, and AC vs. MXenes) are compared in this thesis. This study aims to provide more reference about electrode selection and electrode fabrication for CDI technology.

1.5 Thesis outline

Chapter 1 first summarizes the present desalination technologies and point out their limitations (high energy and high cost). Then, we introduce capacitive deionization technology, which is promising to be cheap and easy-to-operate. The present study and the state-of-the-art about the CDI technology are reviewed, including aspects of architecture, electrode materials, operation modes, limitations and industrial development. Finally, we list three key problems hindering the development of capacitive deionization technology, and specify the motivations and objectives of this thesis.

Chapter 2 introduces the double layer theory for capacitive deionization technology. Gouy-Chapman-Stern (GCS) model is a classic double layer theory which is normally used for supercapacitor. Modified Donna (mD) model is derived from GCS model considering that the lower electrolyte concentration is employed in CDI compared with supercapacitor. GCS model is mature and well-known, while mD model have been developing in recent years. Therefore, the updates of mD model are reviewed and concluded. The effect of key factors (such as surface charges, operation modes and applied voltages) on CDI performance is analyzed based on the mD model.

In Chapter 3, the stability degradation mechanism of CDI is explored. Based on ion extraction method (which has not been employed by CDI community before) and batch-mode long-term cycling operation, the dynamic movement of salt ions and their relationship with surface charges near the aged electrode is studied. Therefore, the performance degradation of aged electrode can be well-understood. Furthermore, a novel testing method is proposed to describe the degradation extend of the aged electrode based on the proposed degradation mechanism.

Chapter 4 demonstrates that the lost performance of aged electrode can be recovered by thermal treatment. Materials characterization technologies (X-rag photoelectron spectroscopy, N_2 adsorption-desorption, scanning electron microscope, etc.) are used to explore the mechanism. This study found that the thermal treatment can burn off the extra formed surface functional groups on the aged carbon surface, thus the properties (resistance, potential of zero charge, surface area, etc.) of aged electrode can be recovered accordingly. This proposed regeneration method (thermal treatment) can be industrially applied and the revealed regeneration mechanism can also facilitate the development of other regeneration methods.

Chapter 5 compares the desalination performance of different electrodes under the same electrode specifications and operation conditions. Two carbon-based electrode materials are first compared (AC versus ACF). Then, traditional material is compared with novel intercalation material (AC versus MXene). The result illustrates that the resistance and the ion-selectivity are two important considerations among various electrode properties.

Chapter II

Electric double layer (EDL) theory for CDI

2.1 Gouy-Chapman-Stern (GCS) model

2.1.1 Brief introduction of GCS model

The principle of electric double layer is the fundamental mechanism by which CDI technology desalinates and extracts ions. When applying a voltage on electrodes, the electrode/solution interface will form a parallel double layer by static force. One layer is on the surface of electrode and the other layer formed by opposite ions is on the solution at a small distance to electrode as shown in Figure 2.1. The layer formed near electrode surface is termed Helmholtz layer and the width of this layer is the largest radii of solvated ions in this line. Usually, the thickness of Helmholtz layer is about 0.2 nm. Theoretically, the Helmholtz layer can be viewed as a capacitor and potential drop in this layer is linear. The potential distribution (φ) in the Helmholtz layer derived from Poisson equation is,[75]

$$\varphi = \varphi_M - 2(\varphi_M - \varphi_S)x/a \qquad \text{(Equation 2.1)}$$

For the region $0 \leq x \leq$ a/2, as shown in Figure 2.1, where φ_M and φ_S are the potential in the metal and solution, respectively, x is the distance from the electrode/solution interface, and a is the diameter of the solvated counter ion. The specific derivation process can be found in electrochemistry books.[75, 76] Helmholtz model itself is incomplete to describe the double layer as it doesn't consider the thermal motion of ions. To compensate the double layer model, Gouy and Chapman describe the diffuse layer. The potential distribution of diffuse layer model is expressed as,

$$\varphi(\zeta) - \varphi_S = (\varphi_{OHP} - \varphi_S)e^{-\kappa\zeta} \qquad \text{(Equation 2.2)}$$

For the region $x \geq a/2$, where ζ is the distance from the outer Helmholtz plane (OHP) ($\zeta = x - a/2$), φ_{OHP} is the potential at OHP, and $1/\kappa$ is the thickness of the diffuse layer. Stern combines the Helmholtz layer model and diffuse layer model, so the EDL model is more realistic. Figure 2.1 shows the curves of potential drop of EDL model. The thickness of double layer depends primarily on the ionic strength. In dilute solutions, the diffuse layer may extend more than 10nm, while in concentrated solutions, the diffuse layer can be neglected and the thickness of double layer equals to the thickness of the Helmholtz layer.
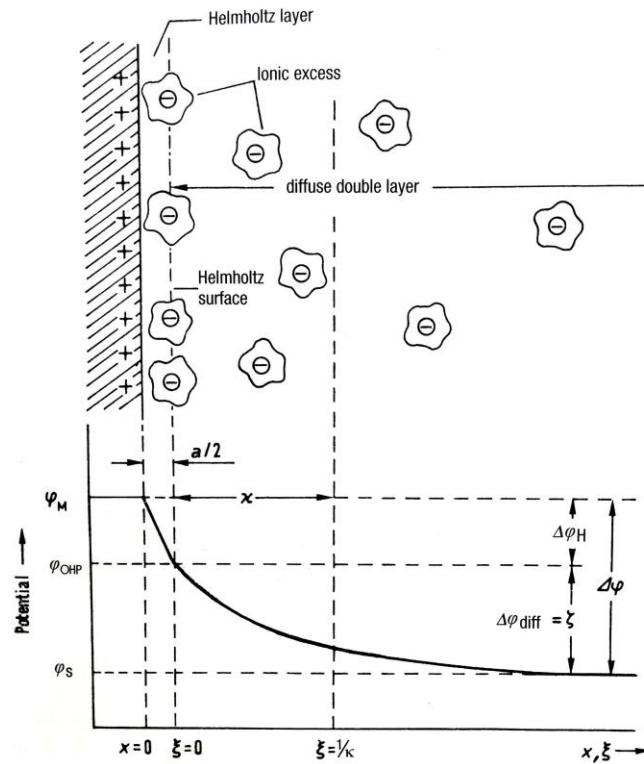
Figure 2.1 Potential distribution at the region of double layer, from ref [75]

2.1.2 Differential capacitance

One difference between plate capacitor and the double layer formed in solution is that the capacitance for a plate capacitor is usually a constant, while that for a real formed double layer changes with the applied potentials and the electrolyte concentrations. Therefore, the differential capacitance (C_d) is used to distinguish from the integral capacitance (C). D.C.Grahame[77] measured variations of differential capacitance at different electrode potentials for mercury electrode in various concentrations of aqueous NaF (Figure 2.2a). In dilute solutions, the value of C_D is the lowest at the point of zero charge (PZC) while this phenomenon disappears in high concentration electrolytes. This also means that double layer performs similar with plate capacitor in high concentration electrolyte. In GCS model, the Helmholtz layer and diffuse layer can be viewed as two capacitors in serial, so total capacitance of the double layer can be expressed as,

$$\frac{1}{C_d} = \frac{1}{C_H} + \frac{1}{C_D}$$ (Equation 2.3)

Where C_H is the capacitance of Helmholtz layer and is a constant, C_D is the capacitance of diffusion layer and varies according to real conditions such as applied potential and electrolyte concentration. At potential of zero charge, C_D has the minimal value and increases dramatically in either side, showing a V-shape. The total differential capacitance C_d is determined by the smaller value of these two components. As shown in Figure 2.2b, the calculated value of C_d from GCS model has the similar trend with the measured value (Figure 2.2a).

One of the biggest differences between CDI and electrochemical capacitor is the difference of electrolyte concentration. The electrolyte in electrochemical capacitor is very dense so it provides more charges (ions) during working, while the electrolyte used

in CDI technology is usually brackish water with much lower salinity. We should pay attention on that since the electrolyte concentration in CDI is low, electrochemical tools such as cyclic voltammetry (CV) or electrochemical impedance spectroscopy (EIS) cannot be directly employed in CDI technology. This is because that during the test, the resistance of the solutions changes a lot and the equivalent circuit behind these electrochemical tools is not suitable anymore. Electrochemical tools can only be applied when considering the change of the electrolyte concentration.
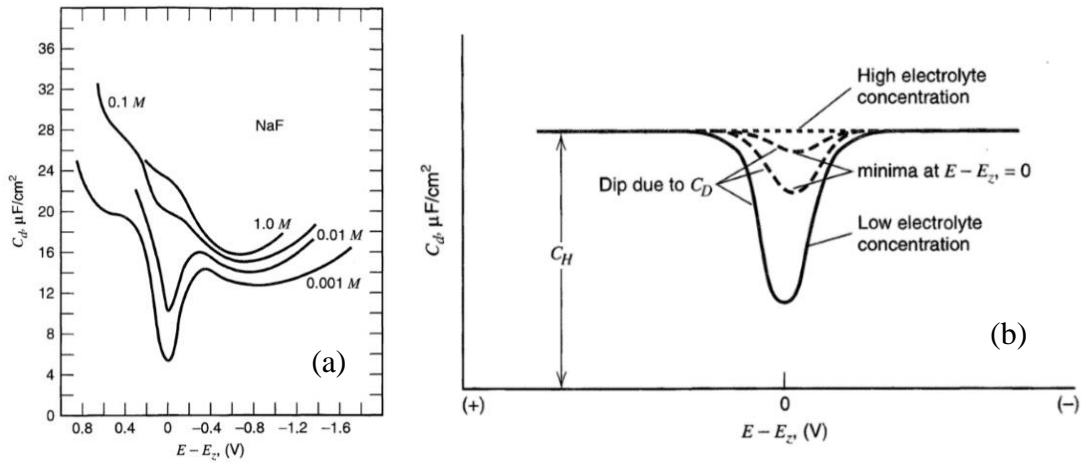
Figure 2.2 (a) Differential capacitance vs. potential for NaF solutions in contact with mercury at 25°C, from ref [77] (b) Expected behavior of C_d according to GCS theory as the electrolyte concentration changes, from ref [76].

2.1.3 Brief introduction of potential of zero charge (PZC)

The value of PZC is first measured through dropping mercury electrode by Lippmann in 19th century.[76] As shown in Figure 2.3a, when a mercury droplet is covered with a layer of dilute sulfuric acid, an electric double layer forms at the metal-electrolyte phase boundary. Then the repulsion between oppositely charged ions flatten the droplet

surface, lowering the surface tension of mercury. The relationship between surface tension and electrode potential can be tested by a well-designed dropping mercury electrode, which is connected with an external adjustable voltage source. The details of the experiment and equations derivation can be found in book electrochemistry, chapter 3.[75] The tested relationship between surface tension and electrode potential is called electrocapillary curve (Figure 2.3b). The plot illustrates that at the potential value of -0.52 V vs. normal calomel electrode (NCE), the surface tension is the maximum, which means the mercury surface is free of charge at this potential. Therefore, this potential is defined as potential of zero charge (PZC). The negative value of PZC, as shown in Figure 2.3b, also implies that the electrode has positive charges at potential of 0 V vs NCE .
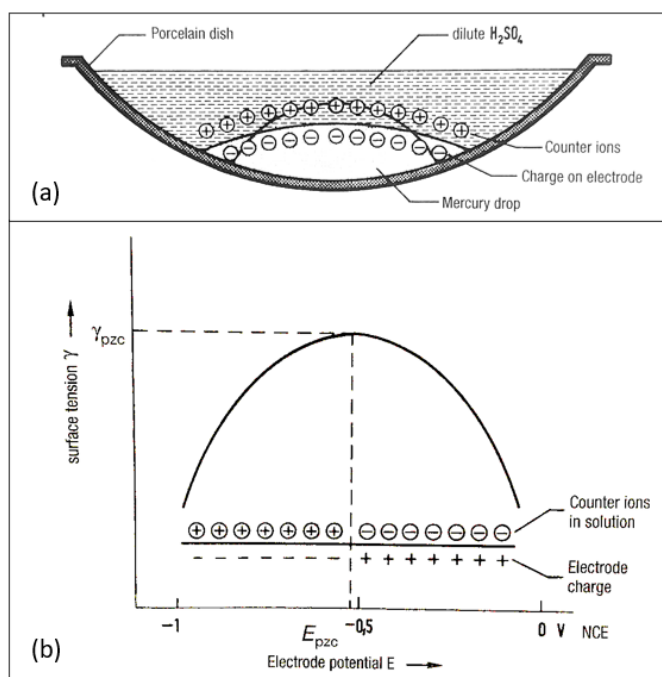
Figure 2.3 (a) Flattening of the surface of mercury on formation of an electrolytic double layer, represented for negative charging of the metal with respect to the solution. (b) Electrocapillary curve, E_{pzc} is the potential of zero charge and γ_{pzc} the surface tension at the zero-charge potential, from ref [75]

PZC is an important electrochemical property of the electrode, implying the sign and amount of its surface charges. Since the setup of dropping mercury electrode is complex and toxic, PZC is currently measured by an easier electrochemical method: electrochemical impedance spectroscopy (EIS). In EIS method, the dilute solution is used and then the frequency is scanned from high to low at different potentials. The impedance of the system comes from the resistance (R) and the capacitance (C) (A simple equivalent circuit is RC series circuit). Therefore, the real part of the impedance is correlated with resistance, while the imaginary part of the impedance is used to calculate the capacitance. The low scan rates are usually used to calculate the capacitance, at which the impedance is mainly from the capacitance. As mentioned in the former section: on the condition of dilute solution, the differential capacitance is minimal at PZC. Therefore, the potential, from which the calculated capacitance is the minimum, can be viewed as the PZC of the electrode.

2.2 modified Donnan model

From GCS model, the thickness of double layer is ~3 nm at 10 mM NaCl (the normal salt concentration used in CDI). However, since carbon-based materials with micropore (pore diameter < 2 nm) are commonly employed as electrodes, GCS model is not suitable in this situation as there is a strong overlap in the diffuse layer in micropore. Therefore, the modified Donnan (mD) model is widely employed in CDI area,[78-80] which is derived from the GCS model and considers the overlap of the diffuse lay in GSC model.

The mD model was first developed by Biesheuvel P.M. et al. at 2011.[81, 82] Up to now, many researchers have contributed to the development of the mD model. On the one hand, the mD model is simplified during these years to only satisfy basic data fitting purpose,

so that the simplified mD model can be widely employed by researchers. On the other hand, theoretical researchers keep developing the mD model to follow up the development of CDI technology, as well as to improve the accuracy of mD model. In this section, the simplified mD model at the equilibrium and the advanced transport mD model to describe the dynamics of ions transportations are organized and concluded from the literature review, so that the data in the following chapters of this thesis can be theoretically studied.

2.2.1 mD model at equilibrium

As illustrated in Figure 2.4, in mD model, the Stern potential ($\Delta\phi_{St}$ or $\Delta\phi_S$) in mD model is the same as the Stern potential in GCS model, illustrating the potential drop through the Stern layer (also named Helmholtz layer).[83, 84] The Stern potential ($\Delta\phi_S$) relates to the net charges (σ_{mi}, mM) in micropore by,

$$\Delta\phi_S \cdot C_s \cdot V_T = -\sigma_{mi} \cdot F \qquad \text{(Equation 2.4)}$$

Where C_s is the Stern capacity (0.145 GF/m^3), V_T is the thermal voltage (0.0256 V), and F is Faraday's number (96485 C/mol). $\Delta\phi_S$ is dimensionless and can be multiplied by the thermal voltage V_T to arrive at voltages (with units of V).[83]

The Donnan potential ($\Delta\phi_D$, dimensionless) refers to the potential difference between outside and inside the micropore. Different from GCS model, since the micropore diameter is less than 2 nm and the diffuse layer is overlapped, a distance term is excluded and the Donnan potential is directly used to indicate the potential drop from the Helmholtz surface to the external solution. The Donnan potential relates to the concentration of specific salt ions in micropore ($C_{i,mi}$, mM) and in macropore/external solution ($C_{i,\infty}$, mM) by,

$$C_{i,mi} = C_{i,\infty} \times exp(-Z_i \cdot \Delta\phi_D) \qquad \text{(Equation 2.5)}$$

Where Z_i is the number of charges of specific salt ions. For example, when NaCl is used as the only salt in the solution, from the above equation, the concentrations of Na$^+$ and Cl$^-$ in micropore can be described as,

$$C_{Na,mi} = C_{Na,\infty} \times exp(-\Delta\phi_D) \qquad \text{(Equation 2.6)}$$

$$C_{Cl,mi} = C_{Cl,\infty} \times exp(\Delta\phi_D) \qquad \text{(Equation 2.7)}$$

Therefore, the total salt concentration (C_{mi}, mM) in micropore and the net charges (σ_{mi}, mM) in micropore can be deduced as follows,

$$C_{mi} = C_{Na,mi} + C_{Cl,mi} = 2 \cdot C_\infty \cdot cosh(\Delta\phi_D) \qquad \text{(Equation 2.8)}$$

$$\sigma_{mi} = C_{Na,mi} - C_{Cl,mi} = -2 \cdot C_\infty \cdot sinh(\Delta\phi_D) \qquad \text{(Equation 2.9)}$$

Where C_∞ is the ion concentration in macropore/external solution (mM).
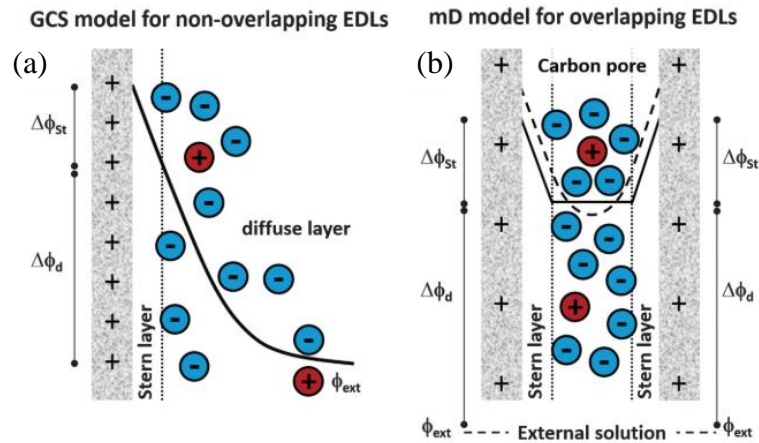
Figure 2.4 Classic GCS EDL model (a) vs. modified Donnan model (b) to describe ion storage in carbon pores, from ref. [27]

When the external voltage is applied to a CDI cell (V_{cell}, V), assuming the applied voltage is equally distributed on the two electrodes,

$$V_{Cell} = 2 \cdot V_T \cdot (\Delta\phi_D + \Delta\phi_S) \qquad \text{(Equation 2.10)}$$

There are four variables (C_{mi}, σ_{mi}, $\Delta\phi_D$, $\Delta\phi_S$) in four equations (Equation 2.4, 2.8, 2.9 and 2.10). Therefore, these four equations can be couples and solved given the two inputs (C_∞, V_T). After solving these variables, the stored charges in micropore (Σ_F, C/g), the salt adsorption capacity (SAC, Γ_{salt}, mg/g) of the electrode, and charge efficiency of the CDI cell (Λ) can be solved accordingly,

$$(\sigma_{mi,ch} - \sigma_{mi,disch}) \cdot v_{mi} \cdot F = \Sigma_F \qquad \text{(Equation 2.11)}$$

$$(C_{mi,ch} - C_{mi,disch}) \cdot v_{mi} \cdot M_{NaCl} = \Gamma_{salt} \qquad \text{(Equation 2.12)}$$

$$\frac{\Gamma_{salt}}{\Sigma_F} = \frac{(C_{mi,ch} - C_{mi,disch})}{(\sigma_{mi,ch} - \sigma_{mi,disch})} = \Lambda \qquad \text{(Equation 2.13)}$$

Where v_{mi} (mL/g) is the micropore volume of the electrode and M_{NaCl} (58.44 g/mol) is the molar mass of the NaCl. When combine Equation 2.8 and 2.9,

$$C_{mi}{}^2 = \sigma_{mi}{}^2 + 4 \cdot C_\infty{}^2 \qquad \text{(Equation 2.14)}$$
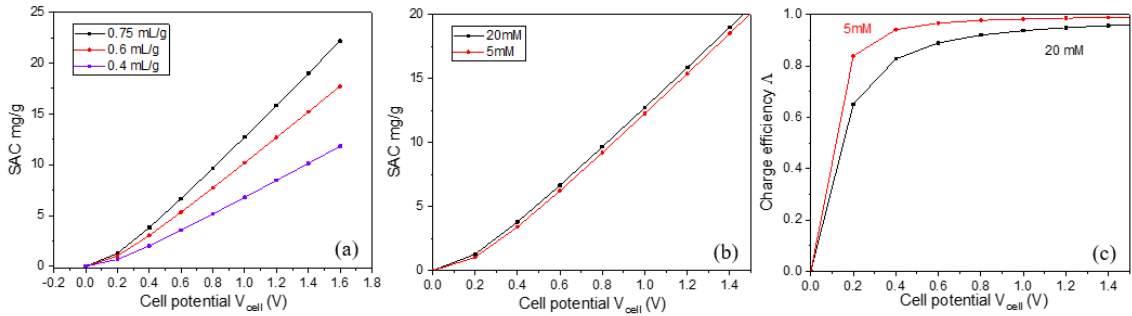
Figure 2.5 Equilibrium data for capacitive deionization (a) SAC (mg/g) as function of cell potential and micropore volume (at salt concentration of 20 mM) (b) SAC (mg/g) as function of cell potential and salt concentration (at micropore volume of 0.75 mL/g) (c) charge efficiency as function of cell potential and salt concentration.

SAC and charge efficiency are the two most important parameters in CDI operation. According to Equation 2.12, SAC is affected by micropore volume of the electrode and the adsorbed salt ions during the charging phase. The latter is determined by the cell potential. As seen from Figure 2.5a, the SAC increases approximately linearly with the increased cell voltage. Since water molecule decomposes at ~1.23 V,[85] the applied voltage in CDI is normally smaller than this number. Otherwise, the charge efficiency decreases dramatically as the applied voltage is consumed on water decomposition. Furthermore, the SAC is proportional to the micropore volume. As the micropore volume increases from 0.4 to 0.75 mL/g, the SAC increases from ~ 8 to ~15 mg/g at V = 1.2V, which voltage is commonly used in CDI studies.[86-88] This is why many researchers are trying to improve the properties of the electrode materials.[47, 89] However, the SAC value is usually smaller in the experimental studies because problems such as Faradaic reactions or cell resistance can affect the performance.[66, 90] Aside from micropore volume, the effect of salt concentration on SAC is also studied. As seen in Figure 2.5b, the SAC does not vary much at salt concentrations of 5 mM and 20 mM, this implies that the normal salt concentration range (5 to 20 mM) used in CDI study has less effect on SAC. On the other hand, SAC itself can only describe the salt adsorption ability of the electrode material rather than a CDI cell. Therefore, a new parameter is proposed to describe the performance of the CDI cell recently, namely, the average concentration reduction of the feed over a cycle (Δc).[72] By this way, not only the properties of the electrodes are important, but also the loading amount of the electrode material and the cell design also matter when evaluating the CDI system.

As for the charge efficiency, it also increases with the applied voltage as shown in Figure 2.5c. At the voltages higher than 0.8 V, the charge efficiency is higher than 90%. According to mD model, the extra applied voltage is spent on co-ion expulsion, thus the charge efficiency is always less than the unity.[83] However, although the charge efficiency is high theoretically, it can be much lower in the real case. Faradaic reactions which can cause leaking current,[69] and the internal resistance which consumes applied voltage in the CDI cell[91] are not considered by this simplified mD model. Therefore, cell design is important and deserves to be studied considering that most of the current studies only focus on the electrode materials and adsorption mechanism. Combining Figure 2.5 a, b and c, it can be speculated that 0.8 to 1.4 V is a suitable potential window for CDI operation.
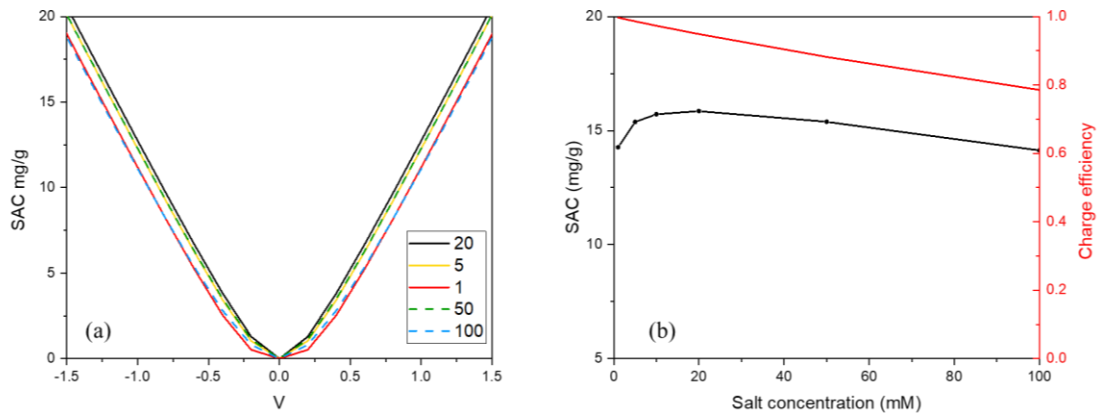
Figure 2.6 The effect of salt concentrations on (a) SAC (mg/g), and (b) charge efficiency (on the condition of $V_{cell} = 1V$ and $v_{mi} = 0.61$ mL/g) calculated by mD model

Figure 2.6a implies that the effect of salt concentration on SAC is less evident than that of the cell potential. Figure 2.6b demonstrates that the SAC is at the range of 14 to

16 mg/g for a wide range of salt concentrations. SAC is of the highest value when the salt concentration is between 10 to 20 mM, which is commonly used as the electrolyte concentration in CDI. Since the purpose of CDI is to desalinate the salt water (electrolyte), sometimes a lower salt concentration (e.g. 5 mM) is also employed,[62] and thus the cleaner product water can be obtained at the outlet. Furthermore, the employment of higher salt concentration causes lower efficiency. This is another reason why the low salt concentrations (5-20 mM) are used in the CDI.

2.2.2 The impact of surface charges on mD model at equilibrium

When the carbon electrode is oxidized, the functional groups on carbon surface which carry charges cannot be neglected.[92, 93] Assuming that the charges of functional groups are immobile (σ_{chem}, mM) and balanced by the electronic charges (σ_{elec}, mM) and ionic charges (σ_{ionic}, mM) in micropore,[83]

$$\sigma_{elec} + \sigma_{ionic} + \sigma_{chem} = 0 \qquad \text{(Equation 2.15)}$$

Under this condition, the above equations are modified as follows,

$$C_{mi}{}^2 = \sigma_{ionic}{}^2 + 4 \cdot C_\infty{}^2 \qquad \text{(Equation 2.16)}$$

$$\sigma_{ionic} = -2 \cdot C_\infty \cdot sinh\,(\Delta\phi_D) \qquad \text{(Equation 2.17)}$$

$$\Delta\phi_S \cdot C_s \cdot V_T = \sigma_{elec} \cdot F \qquad \text{(Equation 2.18)}$$

Equation 2.10 is also applicable here. Therefore, there are totally 5 variables (C_{mi}, σ_{elec}, σ_{ionic} $\Delta\phi_D$, $\Delta\phi_S$) and 5 equations (Equation 2.15 to 2.18 and 2.10). With the three inputs (C_∞, σ_{chem}, V_{cell}), all variables can be solved.

When assuming $\sigma_{chem,A} = -\sigma_{chem,C} = 0.4$ M, where subscript "A" or "C" refers to either anode or cathode, we can calculate the relationship between SAC and applied

voltage, as shown in Figure 2.7. The curve of electrodes with surface charges shifts (red) parallelly compared with that of pristine electrodes. In this condition, the surface charges can adsorb salt ions spontaneously without applying voltage (V_{cell} = 0 V). When applying voltage at V_{cell} = 0.6 V, the SAC is the minimum. This is because that all the applied voltage is consumed to compensate the voltage provided by surface charges. At the positive working potential window (0.8 to 1.4 V), the performance of pristine electrodes is better than the charged electrodes, while at the negative working potential window (0 to -1.4 V), the performance of the charged electrodes is better. This is because the surface charges provide the extra voltage for attracting ions. During the long-term operation of CDI system, the surface charges are gradually formed on the electrode surface, meantime the operation curve shifts from the direction of the black curve to the red curve. Since the applied voltage is positive and constant, the SAC of the electrode decreases accordingly, causing the electrode degradation. On the other hand, modifying electrodes with surface charges can also be a possible method to improve the SAC. This can be achieved by either operating the CDI cell at the negative potential window or changing the sign of surface charges.
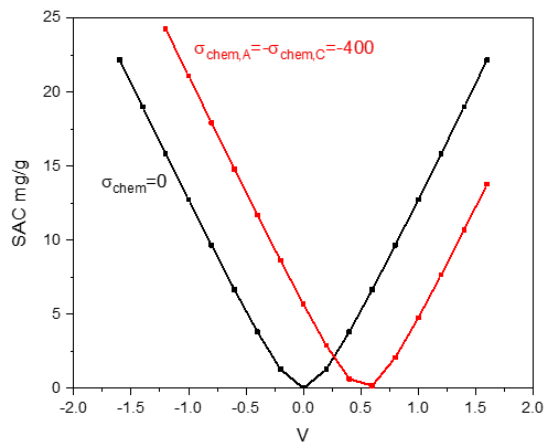
Figure 2.7 The effect of surface charges on SAC

2.2.3 Transport mD model for batch mode CDI

Different from the equilibrium model, C_∞ (the ion concentration in electrolyte) is a variable in the transport mD model. Also, the current (I, A) passing through the circuit is considered. All the variables are solved at each time interval (usually at t = 1 s). The equation 2.10 is changed to,

$$V_{Cell} = I \cdot (R_{ext} + R_{int}) + 2 \cdot V_T \cdot (\Delta\phi_D + \Delta\phi_S) \qquad \text{(Equation 2.19)}$$

Where R_{ext} is the external resistance and R_{int} is the internal resistance. $R_{ext} + R_{int}$ can be solved by fitting the mD model to the real data. In the real case, R_{ext} and R_{int} can also be evaluated by EIS test. The mass transfer between electrodes and reservoir is considered in the batch mode operation by,

$$V_{mi}\frac{\partial C_{mi}}{\partial t} + V_{st}\frac{\partial C_\infty}{\partial t} = 0 \qquad \text{(Equation 2.20)}$$

Where V_{mi} (mL) is the micropore volume of the electrode and V_{st} (mL) is the volume of the stirred tank. V_{mi} of the electrode material can be tested by N_2 adsorption-desorption method. However, not the entire micropore volume can be used efficiently in the real case, so an active ratio is multiplied by V$_{mi}$ in the theoretically calculation by fitting the model to the real data. The σ_{elec} relates I by,

$$V_{mi}\frac{\partial \sigma_{elec}}{\partial t} = -I/F \qquad \text{(Equation 2.21)}$$

Where F is the Faraday's number (96485 C/mol). Equations 2.8, 2.9, 2.14, and 2.19 to 2.21 can be couples together to solve the variables. (6 equations and 6 variables).
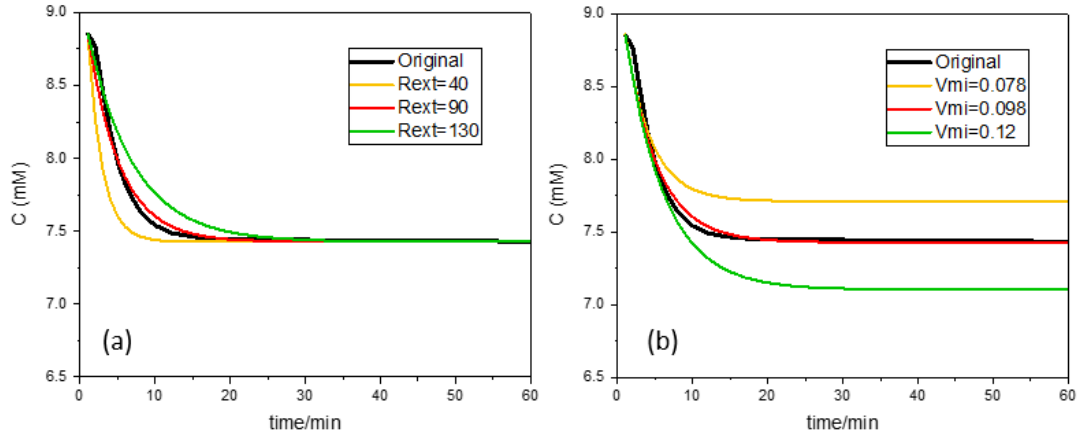
Figure 2.8 The fitting example of mD model to batch-mode data. The effect of (a) the external resistance, and (b) micropore volume on conductivity variation.

Parameters such as the R_{ext}, R_{int}, V_{mi}, and V_{st} affect the performance the CDI cell. Figure 2.8 shows two examples, e.g. R_{ext} and V_{mi}. As illustrated in Figure 2.8a, R_{ext} determines the slope of the desalination curve. With a lower resistance, faster desalination speed can be obtained in the beginning of the charging cycle. Figure 2.8b shows that V_{mi} affects the effluent concentration. As expected, electrodes with higher micropore volume contribute to the desalinated water with a lower salt concentration.

2.2.4 Transport mD model for single-pass mode CDI

The mass transfer in single-pass mode is different from that in batch-mode. The Equation 2.20 is changed to,

$$V_{mi}\frac{\partial C_{mi}}{\partial t} = \Phi(C_0 - C_\infty) - V_{sp}\frac{\partial C_\infty}{\partial t} \qquad \text{(Equation 2.22)}$$

Where Φ is the flow rate (mL/s), and V_{sp} is the volume of the spacer (mL).

Through only changing this Equation and keep other 5 coupled Equations the same as the batch mode (Equations 2.8, 2.9, 2.14, 2.19, and 2.21), all the variables can be solved for the single-pass mode.
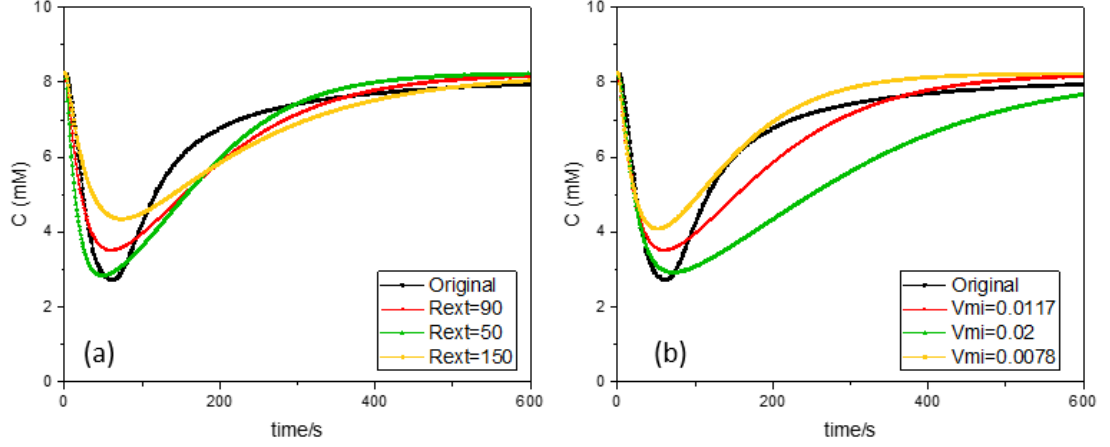
Figure 2.9 The fitting example of mD model to single-pass mode data. The effect of (a) the external resistance, and (b) micropore volume on conductivity variation.

Figure 2.9 shows how R_{ext} and V_{mi} affect the conductivity variation in the single-pass mode. With lower R_{ext} and larger V_{mi}, CDI cell has better desalination performance. Other important parameters also include Φ, V_{sp}, R_{int}, etc.

All the above models are the simplified mD model and only consider the potential drop of the Donnan potential and the Stern potential inside CDI cell. To make the model closer to the reality, the potential drop through the electrode ($\Delta\phi_{ele}$) because of its resistance and the potential drop consumed for ions transfer at spacer ($\Delta\phi_{sp}$) can also be included. In this case, the Equation 2.10 is changed to,

$$V_{Cell} = I \cdot R_{ext} + 2 \cdot V_T \cdot (\Delta\phi_D + \Delta\phi_S + \Delta\phi_{ele} + \Delta\phi_{sp}) \qquad \text{(Equation 2.23)}$$

$\Delta\phi_{ele}$ relates to R_{int} by,

$$\Delta\phi_{elec} \cdot V_T = I \cdot R_{int} \qquad \text{(Equation 2.24)}$$

$\Delta\phi_{sp}$ relates current (I) and electrolyte concentration by,

$$\frac{I}{A} = 4 \cdot D \cdot C_\infty \cdot \frac{\Delta\phi_{sp}}{L_{sp}} \cdot F \qquad \text{(Equation 2.25)}$$

Where A (m^2) is the projected area of the electrode, D is the transfer coefficient (1.68 × 10^{-9} m^2/s), L$_{sp}$ is the thickness of the spacer (m). Equation 2.24 and 2.25 can be coupled with above-mentioned 6 equations (Equations 2.8, 2.9, 2.14, 2.19, 2.21 and 2.22) to solve variables (two equations and two variables are added). Furthermore, researchers also include the ion-exchange membrane in their mD model.[94, 95] Factors such as the diffusion time,[80, 96] attractive forces,[97] the spacer length,[82] etc. are further considered in the advanced mD models. Although some equations are added or modified in each case, the basic logic behind modelling keeps unchanged. With basic mD model described in this chapter, most data in CDI operation can be modelled and further studied.

Chapter III

Role of metastable-adsorbed charges in the stability degradation of carbon-based electrodes for capacitive deionization*

*This chapter is published: Li, B.; Zheng, T.; Ran, S.; Lee, P.-H.; Liu, B.; Boles, S. T., Role of metastable-adsorbed charges in the stability degradation of carbon-based electrodes for capacitive deionization. Environmental Science: Water Research & Technology 2018, 4, (8), 1172-1180.

3.1 Introduction

As the global need for improved water infrastructure has grown in recent years, the stability issues of CDI technology have become ever more important. An increasing number of researchers focus on studying the underlying mechanisms which result in SAC fading over long-term operations.[98-100] Parasitic electrochemical reactions occurring at the electrode surface are most likely to be responsible for stability degradation.[70, 101] Cohen et al.[67, 102] claimed that anodes are gradually oxidized during long-term operations, resulting in the formation of oxygen-containing functional groups. Meanwhile, both pore volume and surface area of anode decrease, leading to the unstable performance. He et al.[69] proposed that oxygen reduction at cathode also contributes to stability deterioration though its effect is not as obvious as the oxidation reactions at the anode. The oxidation of anode also brings surface charges to it, shifting the potential of zero charge (PZC) of the electrode.[36] By modifying electrodes with counter surface charges, Gao et al.[36, 103] further improved the stability performance of the CDI system. Except for electrochemical reactions, some authors also proposed that the adsorbed salt ions may be incompletely

desorbed and trapped in the pores of the electrodes during the adsorption phase.[67, 104] As salt ions carry either positive or negative charges, they may also act as surface charges once they get trapped. However, the existence of trapped salt ions and their influences on stability have not been explored. Therefore, in this chapter, the role of trapped salt ions regarding stability degradation is elaborated.

The concentrations of trapped salt ions are quantified by employing acid/base extraction methods on the aged electrodes. A schematic illustration involving the salt ions based on the classical Gouy-Chapman-Stern (GCS) double layer model has been proposed to fit the result of the chemical analysis and the unstable conductivity changes during long-term operations. Through this extended double layer model, the role of surface charges in the stability degradation can be better understood. Based on the proposed model, a sweeping voltage test was developed to further evaluate the state of the electrodes in a non-destructive manner. This test is used to detect the active voltage window of a CDI device during long-term operations, which can be implemented between cycles and without involving additional electrodes.

3.2 Materials and methods

3.2.1 CDI reactor and set-up

The cell was designed as a flow-by architecture in which the feed solution flows between the two electrodes. As shown in Figure 3.1a, two electrodes (activated carbon fiber (ACF), CH900-20, Kuraray, Japan) were positioned in a parallel configuration and separated by a spacer, of which channels were made for the solution to flow evenly. Two pieces of polyethylene film (Celgard 3501, NC, USA) were placed between the two

electrodes. Two platinum-coated titanium plates were used as current collectors (Pt was used to decrease the contact resistance between the ACF and Ti plates). The whole cell was assembled by covering with two plexiglass panels. The size of these two electrodes was "90×90×0.5" mm^3, and the weight of each was 1.2 (± 0.1) g. The gap (thickness of the spacer) between the two electrodes was fixed at 1 mm. 20 holes were spaced equidistantly around the perimeter of each panel such that the entire cell could be assembled by screws and nuts. 1 mm is a commonly-used distance in a lab-scale CDI cell. At longer distances, CDI cell spends more time reaching the equilibrium, while at shorter distances, the self-discharging problem may become severe, and the SAC may decrease due to the shorter hydraulic retention time.

The layout of the experimental set-up is presented in Figure 3.1b. A beaker containing the salt solution served as a reservoir and was covered with Parafilm to limit water evaporation. A magnetic stirrer was used to ensure homogeneity. A conductivity meter (Jenway 4520, UK) was employed to track the change of conductivity and temperature. The solution was circulated through the CDI reactor using a peristaltic pump with a flow rate of 3 ml/min. A VMP potentiostat (VMP300, Biologic Technologies, France) was employed in chronoamperometry mode to control the potential between the two electrodes.
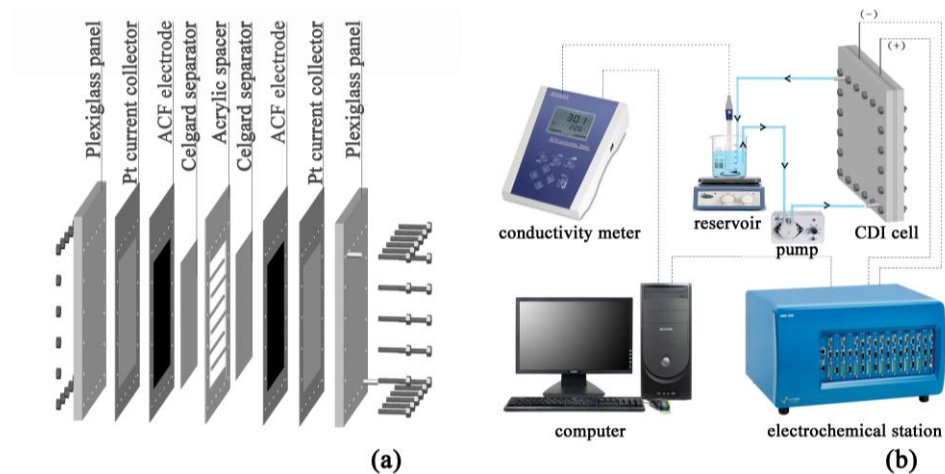
Figure 3.1 Schematic illustrations of (a) a flow-by CDI unit cell and (b) a batch-mode

CDI experiment setup.

The SEM pictures of ACF electrode from Kuraray company are shown in Figure 3.2. As shown in Figure 3.2b, the diameter of a single fiber is ~10 µm. Many single fiber are first spinned to a bundle of fiber, with the diameter of ~300 nm, as shown in Figure 3.2a. Then the fiber bundles are woven into the form of fiber cloth. Therefore, the ACF electrode is free-standing, which is different from normal activated carbon electrode using binder to hold together. Figure 3.2 c and d show the pore structure of carbon fiber surface. The majority of the pore is micropore, contributing to the surface area and the pore volume of ~2000 m^2/g and 0.75 mL/g, respectively.
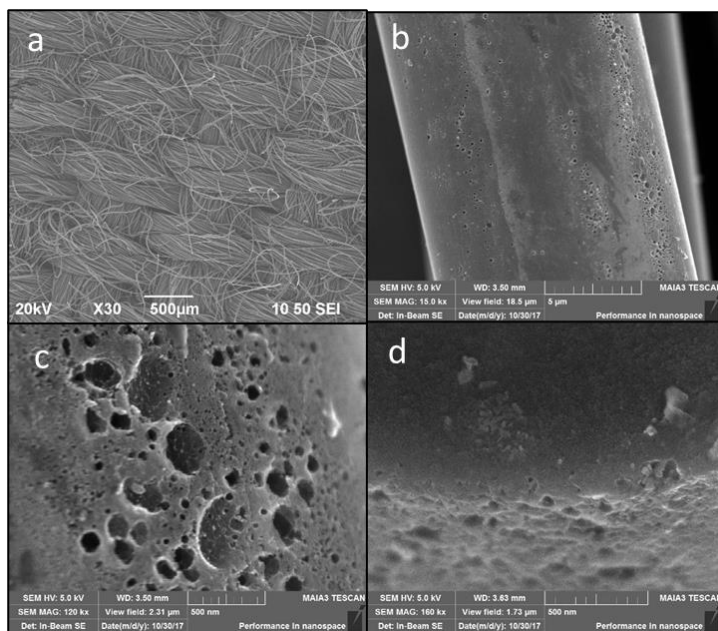
Figure 3.2 SEM pictures of ACF. (a) the overview of the electrode surface. (b) a single fiber of ACF. (c) and (d) pore structure of a single fiber surface.

3.2.2 Cycling tests and reverse-voltage tests

The experiments were conducted in batch mode, where the aqueous stream was continuously circulated between the CDI cell and the reservoir. The solution volume was kept at 100 ml and 2 mM NaCl was used as the electrolyte. A normal cycle consists of 2-hour charging at 1.0V and 2-hour discharging at 0V. The CDI cell was run for 64 normal cycles to study its long-term cycling behavior and degradation.

To evaluate the state of the aged electrodes, a negative voltage (-1.0 V) was applied to the electrodes, similar to the i-CDI method employed by Gao et al.[92, 103] In these investigations, the negative voltage was first applied following the normal charging phase (1.0 V), and for the second time, the electrode was washed, and the negative voltage was applied after the 0V phase.

3.2.3 Na^+/Cl^- extraction of aged electrodes

To quantify the trapped ion content in the electrodes, the CDI cell was run in batch mode with fresh ACF electrodes by using 10 mM NaCl as the electrolyte. Two pairs of electrodes were run for 30 normal cycles (1.0/0 V), of which, one pair was run for an additional 10 reversed cycles (-1.0/0V). After cycling, the aged electrodes were washed by pumping deionized (DI) water into the CDI cell until a conductivity of less than 5 μS/cm was reached at the outlet. In this way, all the salt ions are presumably removed other than those which were trapped in the surface of the electrodes. The ACF samples from both the anode and cathode were cut into pieces with a fixed weight of 0.13 (±0.005) g prior to ions extraction. The pH values of the electrolytes were measured with a pH meter (Orion 3 Star, Thermo Scientific, USA) before cycling, after 30 normal cycles, and after the additional 10 reversed cycles.

For Na^+ extraction, one piece of ACF (0.13 g) from either the anode or cathode was placed into a sample tube containing 13 mL extractants (0.5M HNO_3). Subsequently, all the sample tubes were shaken for 3 hours at 25 °C. The Na^+ concentrations were measured by inductively coupled plasma optical emission spectrometry (ICP-OES) (700 series, Agilent Technologies, US) after the filtration of the extractants. For Cl^- extraction, the same procedure (used for Na^+) was followed except 0.5M KOH was employed as the extractant instead. The Cl^- concentrations were measured by ion chromatography (IC) (Dionex ICS-2500, CA, USA).

3.2.4 V_{ncc} test and its application in long-term operations

To further evaluate the state of the electrodes in a non-destructive manner, a voltage step (0.1-0.8 V) was applied to an aged pair of electrodes (which has seen more than 30 normal cycles) and each step lasted for one hour. Conductivity changes under different voltage steps were recorded as a tool to determine the active voltage window of the CDI cell (voltage of null conductivity change (V_{ncc}) test). The active voltage window is calculated by Equation 3.1,

$$V_{active} = V_0 - V_{ncc} \qquad \text{(Equation 3.1)}$$

Where V_{active} represents the active voltage window of a CDI cell (V). V_0 and V_{ncc} are the applied voltage (V) and the voltage of null conductivity change (V), respectively. The CDI cell underwent long-term operations in four steps: (1) 30 normal cycles, (2) 10 reversed cycles, (3) 25 normal cycles, and (4) 10 reversed voltage cycles. V_{ncc} tests were conducted every 5 cycles to record the active voltage window during these long-term operations. 10 reversed voltage cycles were aimed to recover the SAC lost, similar to the rejuvenation method employed by Farmer et al.[105] The SAC (q) was calculated by following equation.

$$q = \frac{(C_0 - C)V}{M} \qquad \text{(Equation 3.2)}$$

where q (mg/g) represents NaCl removal amount by activated carbon fiber. C_0 and C (mg/L) are the initial and final NaCl concentrations respectively. V (L) is the volume of NaCl solution, and M (g) is the mass of the two electrodes.

3.3 Results and discussion

3.3.1 Salt ions extraction

The concentrations of Na^+ and Cl^- extracted from the electrodes during the initial cycle (fresh electrode), degraded cycle (30 normal cycles), and recovered cycle (30 normal cycles followed by 10 reversed cycles) are shown in Figure 3.3. The concentrations of both Na^+ and Cl^- are low in initial cycle, implying that the fresh electrodes are free of salt ions. After cycling, the concentrations of extracted Cl^- in the degraded cathodes increased dramatically (~35ppm) while those in the degraded anodes are nearly zero. The opposite feature is observed for Na^+ in the respective electrodes, ~4ppm in the anode and nearly zero in the cathode. However, after the recovered cycles, the relatively high concentrations of Cl^- in the cathode and Na^+ in the anode decrease to ~10 ppm and ~0.5 ppm respectively. Therefore, these salt ions are found to be metastable, implying that these ions cannot be removed by short-circuiting the cell in the discharge phase but can be removed by reversing or inverting the voltage during a recovery phase. This metastable behavior of adsorbed salt ions has also been revealed in previous work, although a variety of nomenclature has been employed. Cohen et al.[67] illustrated that the re-adsorptions of co-ions upon discharge gradually become a dominant phenomenon during cycling and the process is irreversible. Gao et al.[92] claimed that Na^+ can be adsorbed by the oxidized anode after alternating polarization. Farmer et al.[105] stated that ions can be removed through reversing the voltage by making the following statement: "the voltage reversal drives chemically bound ions from the surface of the carbon aerogel by imposing significant repulsive electrostatic force." Therefore, the adsorbed salt ions on the carbon surface are defined as metastable here to describe the intrinsic phenomena.
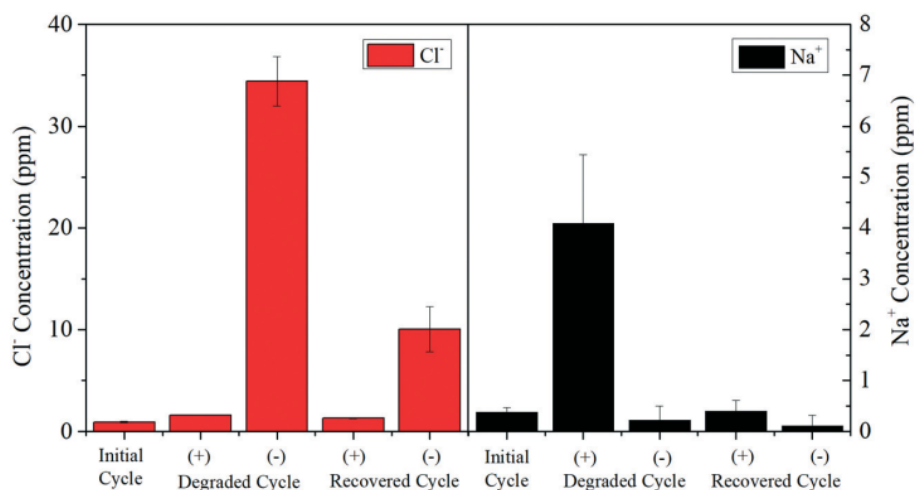
Figure 3.3 Concentrations of Na$^+$ and Cl$^-$ at both anodes and cathodes in the initial cycle (fresh electrode), the degraded cycle (after 30 cycles) and the recovered cycle (after 30 cycles + 10 reversed cycles)

The existence of Na$^+$ in the anodes can be readily explained. As illustrated by XPS O 1s result in Table 3.1, the oxygen content increases in the aged anode evidently after cycling. This implies that oxidation reactions are taking place in the anode during cycling, after which the oxygen-containing functional groups are formed in the anode. The anode oxidation phenomenon is also confirmed by other researchers, proving the formation of oxygen-containing functional groups such as hydroquinone groups and hydroxylic groups.[93, 101] These functional groups bring negative surface charges to the anode. To balance the negative surface charges, Na$^+$ ions behave as ionic charges and are fixed to the surface of the anode. Since Na$^+$ is attracted by Coulombic forces, Na$^+$ stabilizes in the anode and cannot be extracted completely by DI water during ICP preparation. As for Cl$^-$, however, there is no sufficient evidence for its existence in the cathode. One possible explanation from the classic GCS model is that Cl$^-$ may be specifically adsorbed on

electrode surface. The GCS model consists of a Helmholtz layer and a diffuse layer. Ions in the outer Helmholtz plane (OHP) and diffuse layer are solvated and considered as mobile, while ions at the inner Helmholtz plane (IHP) are de-solvated or partly de-solvated and are specifically adsorbed.[75, 76] As the interaction forces between the ions in the IHP and electrode surface are strong (van der Waals forces, hydrogen bonds, chemical bonds, etc), these ions are held more stably.[77, 106] In particular, anions are more likely to be specifically adsorbed on the electrode surface because of high polarizability.[75, 77] Generally, the results of ionic adsorption may be caused by the potentiometric response of carbon electrodes, which are correlated with the functional groups of the carbon surface, their interactions with solutions and the pH environment, etc.[106] As a result, the adsorption sites that respond selectively to ions in solutions of electrodes vary from the anode to the cathode and the resulting ionic adsorption behaviours may be different.

Table 3.1 Atomic concentration of functional groups in O 1s XPS spectrum

Sample	O 1s %	
	O-C	O=C
Pristine	1.09	2.336
Aged anode	3.369	7.519
Aged cathode	1.491	3.846

The pH values of the electrolytes before and after the degraded or recovered cycles (0, 30, and 30 + 10 cycles) are all around 7.5, implying that the overall acidity of the electrolyte is stable in the CDI system. Although the pH environment in the vicinity of the single electrodes is reported to be unstable (i.e. becomes basic near the negative electrode and acidic near the positive electrode,[69, 70]) the negligible pH change of the bulk

solution in this work may be because the bulk solution is well mixed, the applied voltage (1 V) is low and the cycling time (~6 days) is short. These results are consistent with others who also indicate that the overall pH change of the electrolyte is not evident during cycling and that any interference of pH on the electrolyte/solution conductivity is insignificant under certain conditions.[68]

3.3.2 Inversion effect and GCS model fitting

The desalination behavior during the long-term operation of 64 cycles (256 hours) is shown in Figure 3.4, and the conductivity changes during earlier cycles (15th and 16th cycle, namely 60 and 64 hours) and later cycles (52nd and 53rd cycle, namely 208 and 212 hours) are presented in Figure 3.5 a and b, respectively. The overall conductivity profile indicates that the performance of the cell decreased by more than 50% after 50 cycles (200 hours), which is comparable to others' results.[92, 107, 108] The earlier cycles display typical CDI behavior where the solution conductivity decreases during the charging phase from 202 to 76 μS/cm and increases to 202 μS/cm during the discharging phase (Figure 3.5a). However, an inversion effect appears over prolonged periods of cycling where the conductivity at the start of the adsorption phase rises (indicated by a single asterisk), and a gradual decrease is seen at the end of the desorption phase (two asterisks) (Figure 3.5b). Bouhadana et al.[108] report that the PZC of the anode continuously changes due to its surface oxidation, leading to this inversion effect. The inversion peak is caused by the desorption of co-ions in the beginning of the charging stage, while the decrease of conductivity in the discharge phase is caused by re-adsorption of these co-ions.[67, 105]
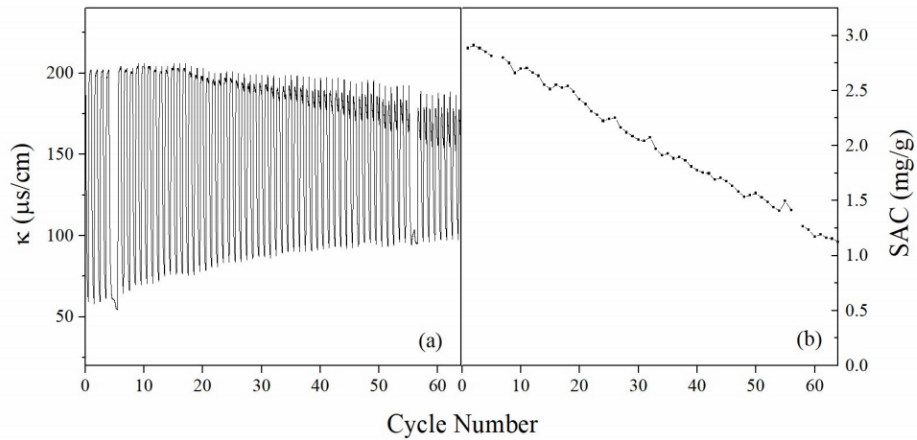
Figure 3.4 Variation of conductivity and salt adsorption capacity (SAC) over 64 cycles
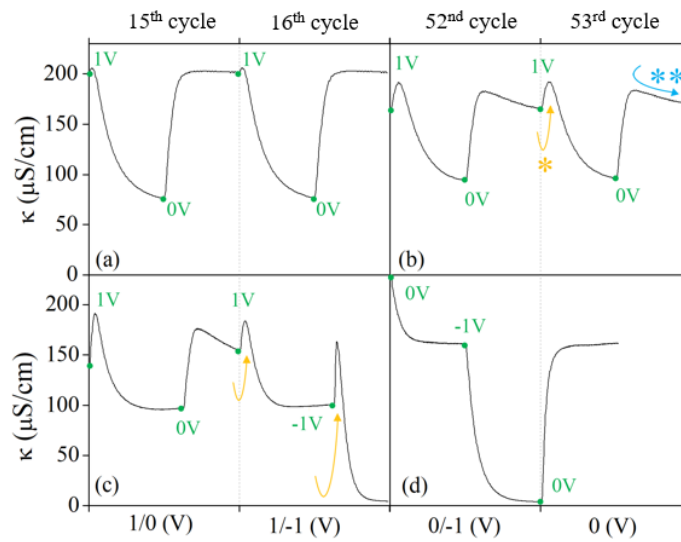
Figure 3.5 Variation of conductivity (a) in earlier cycles (15th and 16th) and (b) in later cycles (52nd and 53rd); variation of conductivity in the cycles involving the voltage inversion phase (c) after the charging phase (1/−1 V) and (d) after the discharging phase (0/−1 V) of aged electrodes.

A schematic illustration of the inversion effect involving surfaces charges based on the classical GCS model is depicted in Figure 3.6. This schematic illustration includes both oxygenated groups (from others[67, 69, 90]) and salt ions (from section 3.3.1 in this

chapter). The Figure 3.6a (stage 0) shows the net charge distribution at the surface of the aged anode. Large circles refer to solvated salt ions while small circles refer to de-solvated or partly de-solvated counter charges (oxygenated functional groups) at IHP. It has been proved that there is a layer of counter charges accumulated at IHP after long-term cycling. As Na^+ ions are attracted by Coulombic forces from counter charges, they also exist in the anode. In this case, the inversion effect shown in Figure 3.5c can be schematically illustrated in Figure 3.6, which demonstrates the dynamic movement of ions and their induced corresponding conductivity changes in stages I-VI. Under 0V, the counter charges can absorb a small number of positive ions (stage 0). When applying 1V (stage I and II), the electrode firstly repels the adsorbed positive ions (stage I), causing a small peak in conductivity while these counter charges are still fixed on the electrodes. In the later part of the charging phase (stage II), the typical behavior of conductivity is observed. However, as the counter charges partly compensate for the applied voltage, the SAC of the cell decreases compared with thoes in the initial cycles. When short-circuiting the cell (stage III and IV), the release of mobile salt ions causes the typical increase in conductivity seen in the early desorption phase (stage III). Then, the adsorption of positive ions causes a gradual decrease in the later desorption phase (stage IV). Importantly, the schematic illustration explains that the counter charges further enhanced the negative electric field created by applying -1.0V, resulting in a dramatic desalination ability (stage VI). Furthermore, the possible ion/charge distribution for both electrodes is shown in Figure 3.7.
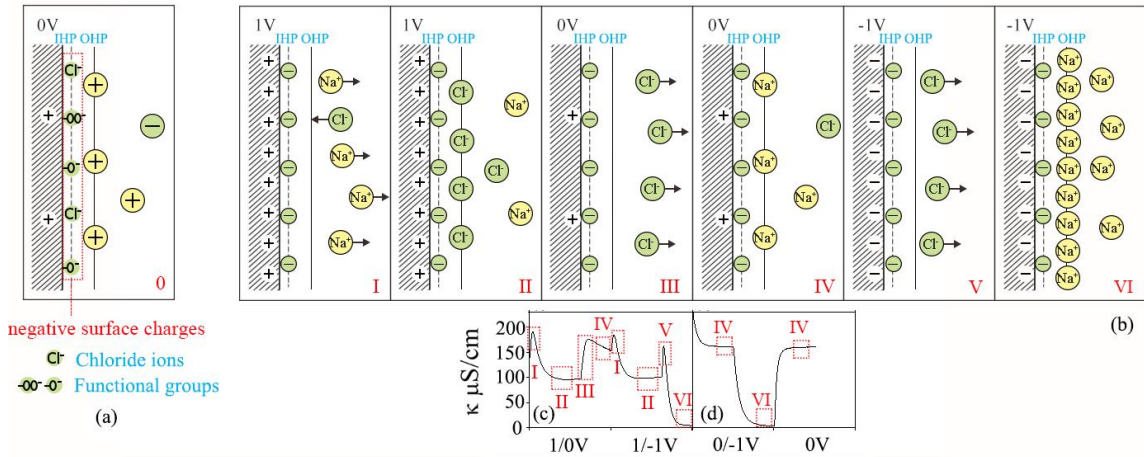
Figure 3.6 A dynamic illustration of ions at the surface of the aged anode based on the classic double-layer model in (a) the neutral state, and (b) under three working conditions (1 V-charging, 0 V-discharging and −1 V-reversed charging). (c) and (d) are extracted from Figure 3.5.
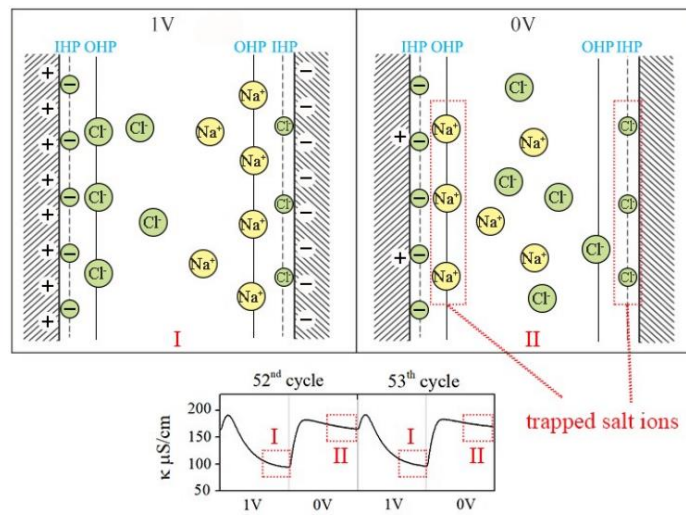
Figure 3.7 The schematic illustration of ion/charge distribution at the surface of degraded electrodes based on classic double-layer model under two working conditions (1V-charging, 0V-discharging)

This model fit well with the results from Section 3.3.1. Since the extracted Na^+ from the anodes are attracted by surface charge and are mobile, these ions should be in the OHP or diffuse layer. This is in accordance with the Donnan models in which salt ions are proposed to be in the Stern layer, i.e. Helmholtz layer.[83, 109] Based on the fact that surface charges are negligible in the cathode[67] and Cl^- ions in the cathode are metastable, Cl^- ions are likely to be specifically adsorbed in the IHP and are relatively stable and cannot be extracted with DI water.[76, 106] However, the exact states and location of trapped salt ions still need to be further investigated through other advanced charaterization methods. With respect to model fitting, the basic GCS model is chosen rather than the modified Donnan (mD) model since the molecular structure of the Helmholtz layer (not diffuse layer) has been the focus of the ionic interactions.[109]

3.3.3 V_{ncc} test

Based on the illustration in Figure 3.6, the applied voltage (1V) used for ion adsorption in the charging phase is partly offset by surface charges. Only the excess applied voltage is capable of controlling ion adsorption. This causes the conductivity decrease over prolonged cycling. The applied voltage, the electric field created by the surface charges, and the conductivity change of the solution are all correlated. To investigate the link between surface charges and conductivity, a simple voltage sweep test (0.1-0.8V) is employed, during which the conductivity of the solution is recorded. As shown in Figure 3.8a, when lower voltages (~0.1-0.3V) are applied, the conductivity goes up, indicating that the CDI cell is repelling ions. In contrast, the CDI cell is adsorbing salt ions when higher voltages (~0.4-0.8V) are applied. The conductivity change ($\Delta\kappa$) in each

step is plotted in Figure 3.8b. The positive value of Δκ signals that the electrodes are repelling ions while the negative value indicates the electrodes are adsorbing ions.
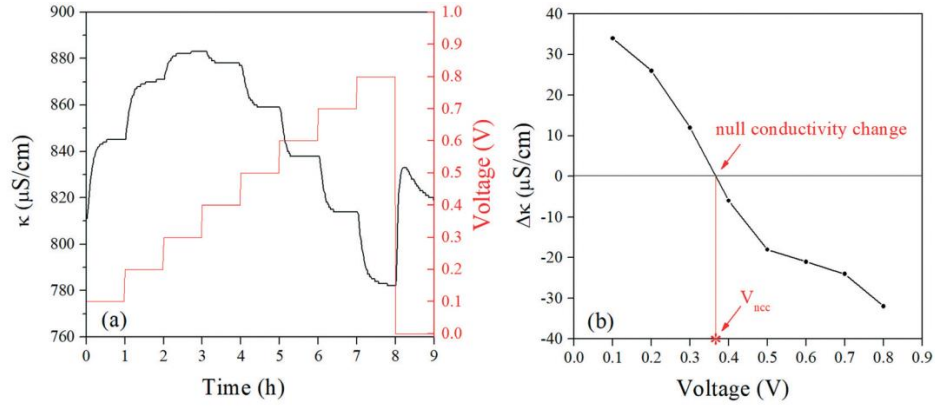
Figure 3.8 The voltage of null conductivity change (V_{ncc}) test: (a) the voltage steps with an interval of 0.1 V is applied to an aged electrode in the range from 0.1 V to 0.8 V and the corresponding conductivity variation is recorded over time. (b) The change in the conductivity (Δκ) is plotted versus each voltage step and the intercept value of the x-axis is defined as V_{ncc}

According to Figure 3.6 (stage 0), the applied voltages of 0.1-0.3V are repelling ions because these voltages can partly compensate for the electric field created by the negative charges in IHP. Therefore, mobile salt ions attracted at the end of 0V-discharging phase can be released to the electrolyte solution, causing the increase of the conductivity. Furthermore, the applied voltages of 0.4-0.8V are sufficient to overcome the electric field created by the negative charges. Therefore, salt ions can be adsorbed at these potentials. From these results, it can be deduced that there is one specific voltage between ~0.3-0.4V which can perfectly compensate the field offered by negative charges. This voltage is termed the "V_{ncc}" here, indicating the voltage of null conductivity change. By plotting the conductivity change versus the applied voltage as shown in Figure 3.8b, a quick

estimation of V_{ncc} can be attained. When the conductivity change is 0 µS/cm, there is neither attraction nor repulsion of salt ions. Thus, the intercept value of x-axis can be considered as the V_{ncc}. Since the V_{ncc} and the active voltage window for attracting salt ions can be understood as the two parts of the applied voltage, the V_{ncc} test provides an estimated active voltage window of a CDI cell. This V_{ncc} test is very simple to operate by just involving the two active electrodes. Through this method, the active voltage change of electrodes can be easily tested during long-term operations.

3.3.4 The relationship between V_{ncc} and salt adsorption capacity

V_{ncc} tests were done during long-term operations of CDI (Figure 3.9a). Both the SAC and active voltage window are plotted versus cycle numbers in Figure 3.9b. The black dots in Figure 3.9b indicate that the SAC of the CDI cell decreases over time in 30 cycles. After ten reversed cycles (-1.0/0V), the CDI cell recovers most of its SAC. Then the SAC decreases again over time following approximately the same fading rate as seen previously. The active voltage window (red dots) decreases from 1 V to 0.5 V over time in the first 30 cycles. During the reversed cycles, the active voltage window increases from 0.5 V to 0.8 V. Then, the active voltage window decreases again with the prolonged normal cycles. Figure 3.9c shows that there is a negative quasi-linear relationship between V_{ncc} and salt adsorption capacity, regardless of cycling history. Therefore, the electrode state can be speculated by simply conducting a V_{ncc} test. Although the PZC of an electrode can be measured by cyclic voltammetry (CV) or electrochemical impedance spectroscopy (EIS) measurement (three-electrode cells) reported by others,[90, 110-112] the utility of these measurements during operations may be challenging because of CDI's traditional two

electrode configuration. The new V_{ncc} test conveniently employs just the active electrodes to achieve the simultaneous and direct measurement of electrodes' active voltage window during long-term operations.
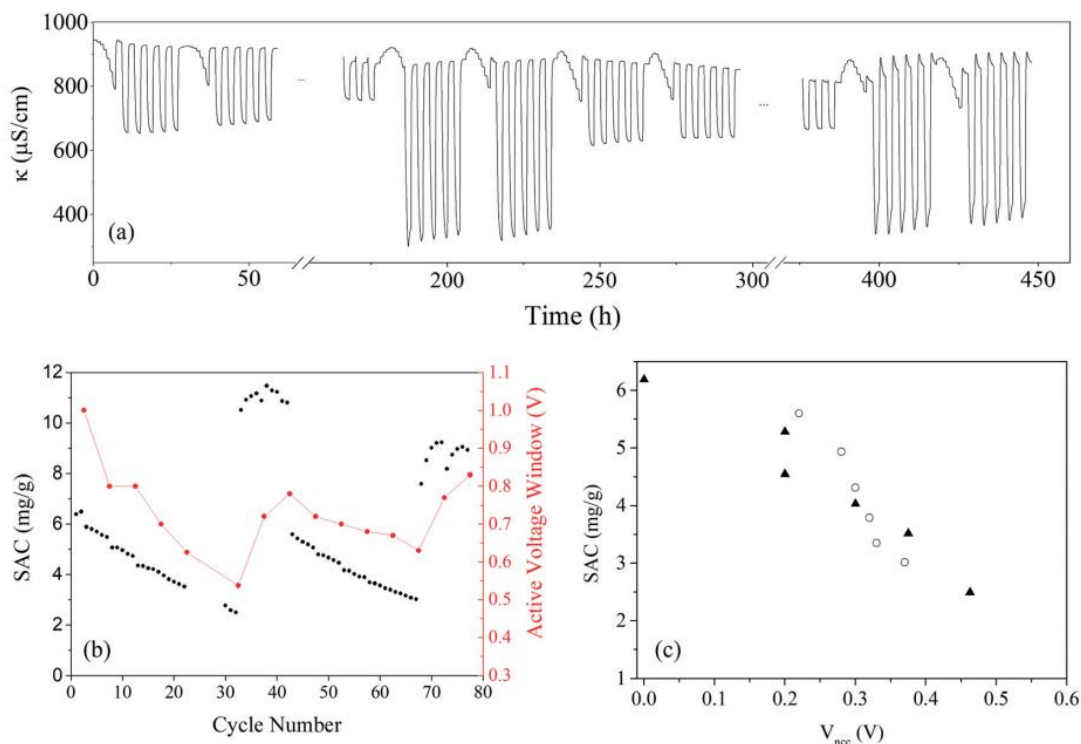
Figure 3.9 (a) Long-term operations of the CDI cell that consist of four steps: 30 normal cycles – 10 reversed voltage cycles – 25 normal cycles – 10 reversed voltage cycles. V_{ncc} tests were conducted every 5 cycles. (b) The variation of the SAC (black) and active voltage window (red) versus cycle number. (c) The negative quasi-linear relationship between the SAC and V_{ncc}. The filled triangles are the V_{ncc} in the first normal 30 cycles while the hollow circles are the V_{ncc} in later normal 25 cycles.

Combining with Figure 3.6, the results of the V_{ncc} test indicate that there is an increasing number of counter charges accumulating at the surface of the anode during operation. The increased counter charges lead to a smaller active voltage window during

prolonged cycling. Although the applied voltage is consistent at 1.0 V, the value of voltage contributing to the adsorption of ions is decreasing as part of the applied voltage is consumed to compensate the electric field offered by negative charges, thereby decreasing the SAC over time.

3.4 Conclusions

This chapter explains electrode stability degradation by extending existing double layer models. The model combines both the latest study of others, based on functional group activity at the electrode surface, and the results of this paper, which suggest a transient behavior by salt-ions in porous carbon. This model can expand the understanding of stability degradation to a broader audience. Furthermore, the concept of intermittent V_{ncc} testing is introduced to empirically quantify the active voltage window of the electrodes during long-term operation. Thus, this method can serve as an indicator of the electrode state in both laboratory experiments and in practical applications where only two-terminal configurations are available.

Chapter IV

Performance recovery in degraded carbon-based electrodes for capacitive deionization*

* This chapter is published: Li, B.; Zheng, T.; Ran, S.; Sun, M.; Shang, J.; Hu, H.; Lee, P. H.; Boles, S. T., Performance Recovery in Degraded Carbon-Based Electrodes for Capacitive Deionization. Environ Sci Technol 2019.

4.1 Introduction

Traditional CDI relies on inexpensive carbon-based electrodes which are composed of materials such as activated carbon and carbon aerogels.[113, 114] One problem hindering the scalability of CDI is the short lifetime of these carbon-based electrodes. In the absence of any membrane enhancements, the sufficient desalination capacity of the electrodes only sustains for hundreds of cycles of the current lab-scale CDI systems.[36, 70, 90, 115] The Faradaic reactions occurred on both electrodes are recognized as the reason for the degradation. Cohen et al.[67] proved that the anodes are gradually oxidized and their pore systems are damaged during the cycling, resulting in the asymmetric distribution of the potential and the effect of excessive co-ion expulsion. This effect is often recognized as the signal of electrode degradation,[68, 93] which is also well-elaborated by dynamic illustrations in Li et al.[43] He et al.[69, 116] demonstrated that the generation of H_2O_2 occurs at the cathode by oxygen reduction, contributing to pH fluctuations and deterioration of electrode stability.

To alleviate the degradation rate, the most commonly used method is to employ ion-exchange membranes, i.e. MCDI system. The employment of membrane limits the oxidant (e.g. O_2, H_2O_2) diffusion to the anode, alleviating the anode oxidation reaction.

Since this method is simple and efficient, MCDI are adopted as commercial CDI products.[63, 64] The drawbacks of this method is that the price of membrane is high and membrane always has fouling problem. Aside from employing membrane, N_2 is pumped into the reservoir in some lab research to increase the stability, so that the dissolved oxygen can be removed and Faradaic reactions can be limited.[68, 101] This method provides a strictly controlled condition for research, but cannot be employed in the industry as the cost of pumping N_2 is too high. Moreover, reversal polarization also works because the cathode is oxidized during the reversed cycles, such that the differences between two electrodes are minimized and the degradation rate slows down.[92, 105] This operation method can be employed widely, but requires more operation design of CDI system. Furthermore, lower voltages can be employed, such that some Faradaic reactions can be avoided and the degradation rate can be alleviated.[67] However, this method also causes the SAC decrease. Although the above-mentioned methods are able to extend the lifetime of the electrodes to some extent, the electrodes will degrade and lose their SACs eventually due to irreversible carbon oxidation. Since stability degradation is inevitable in CDI, the exploration of novel regeneration methods for the lifetime extension of carbon electrode is vital and beneficial.

According to the carbon community, industrial-scale thermal treatment is widely applied for activated carbon regeneration.[117] This method functions through the desorption and/or the decomposition of the adsorbate molecules.[117, 118] Furthermore, thermal treatment is also used to modify carbon materials surface through decomposing volatile species.[106] Since the excess oxides formed on aged electrodes of CDI systems are related to its stability degradation, thermal treatment has a great potential to regenerate

aged electrodes. However, thermal treatment of recovering aged CDI electrodes has not been studied to the best of our knowledge.

In this chapter, thermal treatments are explored to understand their ability to regenerate aged CDI electrodes under a low-to-moderate thermal treatment temperature range (100-700 °C), considering that the carbon surface may form hairline cracks and become hydrophobic when exposed to high-temperatures (800-1000 °C).[74, 119] Systematic electrode replacement experiments are conducted to separate the effects of thermal treatment on the anode and cathode. To investigate the regeneration mechanism, oxygen-containing functional groups of the electrodes before and after thermal treatment are characterized by x-ray photoelectron spectroscopy (XPS) and Boehm titration. Quantification of the surface charges that originate from the formation/decomposition of functional groups is confirmed by the modified Donnan (mD) model. The changes of chemical and physical properties for the electrodes are explored accordingly using gas adsorption techniques, a three-electrode system, etc. To this end, the understanding of the regeneration mechanism offers insights for minimizing electrode degradation and *in-situ* degradation regeneration.

4.2 Materials and methods

4.2.1 Batch-mode CDI

All the tests are run in a batch-mode CDI system as illustrated in Figure 4.1. The aqueous salt solution in the reservoir was circulated in a loop from the CDI cell by using a peristaltic pump. The flow rate was kept at 3 mL min^{-1} for all tests. The reservoir contained 15mL of 10mM NaCl to simulate brackish water and was covered with Parafilm

to reduce water evaporation. A magnetic stirrer was employed to keep the solution well-mixed. The conductivity of the solution in the reservoir was recorded every one minute by the conductivity meter (Jenway, 4520, UK). The voltage of the CDI cell was controlled by a potentiostat (VMP300, Biologic Technologies, France).
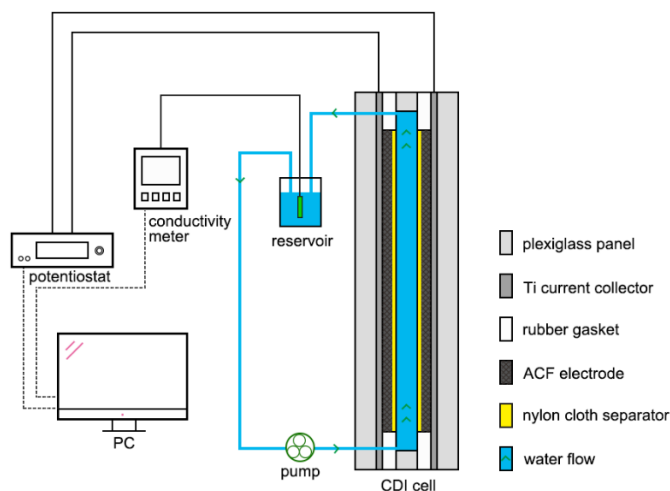
Figure 4.1 Schematic illustration of the batch-mode CDI system

The CDI cell had a symmetrical and multilayer structure, consisting of plexiglass panels, Ti current collectors, activated carbon fiber (ACF) (CH900-20, Kuraray, Japan) electrodes, and nylon cloth (100 mesh) separators from outside-in (Figure 4.1). The size of one ACF electrode was $3\times3\times0.05$ cm^3 with a weight of 0.13 (±0.01) g. Each electrode is covered by a separator with the size of $3.5\times3.5\times0.01$ cm^3. ACF electrodes are saturated in DI water overnight to ensure wettability before assembly. The feed solution was circulated between two electrodes and the reservoir for 30 mins to achieve the equilibrium before charging-discharging cycles.

4.2.2 Thermal treatment tests

To study the effect of thermal treatment on the stability regeneration, the CDI cell was first to run for 20 cycles to reach a degraded state. A single cycle consisted of a 1-hour charging at 1 V and a 1-hour discharging at 0 V. After 20 cycles, the aged anode and cathode were denoted as "20(+)" and "20(-)", respectively. Subsequently, the electrodes were cleaned by pumping deionized water (DI) into the CDI cell until a conductivity less than 5 μS/cm was reached at the outlet. Then, the electrodes were taken out from the cell and dried in an oven at 60 °C overnight.

For the thermal treatment, the electrodes were heated using a tube furnace with the heating rate of 10 °C min^{-1} and then held at a target temperature for 1 hour in Ar atmosphere. After the thermal treatment, the regenerated electrodes were assembled back to the CDI cell and tested for 10 more cycles to evaluate the performance. For the sake of clarity here, temperature values are appended to "20(+) " or "20(-) " for denoting sample history. The effect of gas conditions on degradation regeneration was also explored. The above steps were kept the same except that three kinds of gas (Ar, H$_2$, air) were used and the temperature was kept at 300 °C during the thermal treatment.

To distinguish the role of the anode and the cathode, systematic electrode replacement tests were designed as illustrated in Figure 4.3b. The pristine ACF electrodes were first to run for 20 cycles. Each of the two aged electrodes was paired with a pristine electrode and then tested for another 10 cycles. The aged electrodes after thermal treatment under 300 and 500 °C were also paired with a pristine electrode and run for 10 cycles to evaluate their performance. To determine the performance of the electrodes, the SAC Γ (mg g^{-1}) was calculated by the Equation 4.1.

$$\Gamma = \frac{(C_0 - C)V}{M} \qquad \text{(Equation 4.1)}$$

Where C_0 and C (mg L^{-1}) are the initial and final concentrations of the reservoir, respectively. V (L) is the volume of the reservoir, and M (g) is the mass of the two electrodes. The SAC retention rate was the ratio of Γ/Γ_0. Γ and Γ_0 (mg g^{-1}) are the SAC at each specific cycle and at the first cycle, respectively. The details of SAC calculation are provided as follows.
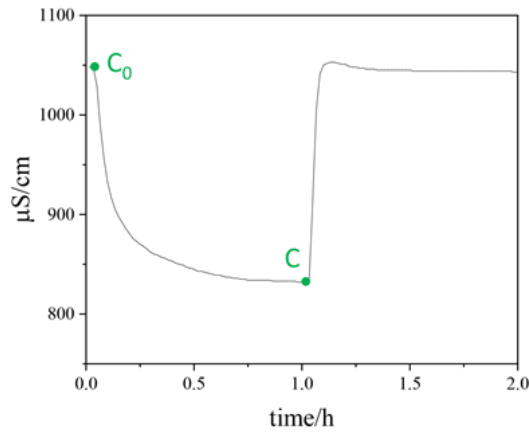
Figure 4.2 The conductivity change of the 1st cycle during cycling (extracted from Figure 4.4a). The curve exhibits typical features of a batch mode CDI system

The unit transfer from $\mu S/cm$ to $mmol/L$ refers to the standard curve for NaCl at 25 °C in book *Electrochemistry*[75] (Chapter 2, Table 2.2),

$$C_0 = 1048 \, \mu S/cm = 8.82 mmol/L$$

Since molar mass of NaCl is 58.5 g/mol, the unit of mmol/L can be transfer to mg/L,

$$C_0 = 8.82 \, mmol/L \times 58.5 \, g/mol = 515.97 \, mg/L$$

Similarly,

$$C = 832 \, \mu S/cm = 407.45 \, mg/L$$

Thus, the SAC Γ (mg g^{-1}) was calculated by the Equation 5.1,

$$\Gamma = \frac{(C_0 - C)V}{M} = \frac{(515.97 - 407.45)\ mg/L\ \times 0.015\ L}{0.2772\ g}$$

$$= 5.87\ mg/g$$

Where V (0.015 L) is the volume of the reservoir, and M (0.2772 g) is the mass of the two electrodes.

4.2.3 Characterization

4.2.3.1 Surface morphology

The morphologies of electrodes before and after thermal treatment were tested by scanning electron microscopy (SEM) (MAIA3, Tescan, Czech Republic), using a 5 kV accelerating voltage. The same position (upper middle part, ~1×0.5 cm^2) of each electrode was cut for SEM characterization. The pore size distribution and specific surface area were analyzed by nitrogen gas adsorption-desorption at 77 K (3Flex Physisorption, Micromeritics, USA). Before gas adsorption-desorption tests, samples were cut into small pieces, weighed around 0.1 g and heated at 90 °C overnight to further remove adsorbed water. Since micropores are predominant in this ACF, the Langmuir equation was used to calculate the surface area and the Horvath-Kawazoe (HK) model was employed to determine the pore volume. ACF pores are classified into three basic groups: pores with diameters (1) less than 2 nm (micropores), (2) between 2 and 50 nm (mesopores), and (3) more than 50 nm (macropores).[120]

4.2.3.2 Surface functionality

The surface chemistry of ACF was analyzed by Boehm titration, which was based on assumptions that NaOH neutralizes lactonic, carboxylic and phenolic groups; Na_2CO_3 neutralizes carboxylic and lactonic groups; and $NaHCO_3$ neutralizes only carboxylic groups.[121] Before the titration, an ACF electrode was dried at 60 °C overnight and cut into

small pieces. 0.03 g sample was weighed and saturated into 10 mL 0.01 M NaOH, NaHCO$_3$, HCl and 0.005 M Na$_2$CO$_3$, respectively. All samples were shaken at room temperature overnight and then filtered to 5 mL solution, after which 10 mL 0.01 M HCl was added to samples in NaOH, NaHCO$_3$, and Na$_2$CO$_3$ for back titration.[122, 123] In the last step, all samples were bubbled with N$_2$ for 1 h to remove CO$_2$ and then titrated with 0.01 M NaOH with bubbling continued.

X-ray photoelectron spectroscopy (XPS) characterization was carried out to investigate the presence of surface chemistries, with a Mg Kα achromatic x-ray source. Samples were cut into 1×1 cm^2 piece and dried at 60 °C overnight before analyses. A Gaussian-Lorentzian mix function and Shirley background subtraction were conducted for spectrum deconvolution. The maximum constraint of the full width at half-maximum (FWHM) was set as 2 eV.

4.2.3.3 Electrochemistry tests

The electrochemical performance of electrodes was evaluated with a conventional three-electrode system. Samples were cut into 1×1 cm^2 pieces before tests. A Pt plate of the same size and an Ag/AgCl electrode were employed as the counter and the reference electrode, respectively. 1 M NaCl was used as the electrolyte for cyclic voltammetry (CV) and galvanostatic charge-discharge (GCD) tests, while 10 mM NaCl was served for potential of zero charge (PZC) analyses. For CV tests, scan rates of 1, 2, 5, 10 mV s^{-1} were conducted with the potential window of -0.2 to 0.4 V (vs Ag/AgCl). The gravimetric capacitance C_s (F g^{-1}) was calculated using the Equation 4.2.

$$C_s = \frac{\int i dV}{2v\Delta VM}$$

(Equation 4.2)

Where i (A) is the charge/discharge current, ΔV (V) is the potential window, v (V s^{-1}) is the scan rate and M (g) is the mass of the sample at working electrode. The charge/discharge currents were set as 5/-5 mA for GCD tests and the voltage range was 0-0.6 V. The resistance R (Ω) was calculated via the Equation 4.3,

$$R = \frac{\Delta V}{\Delta I}$$ (Equation 4.3)

Where ΔV is the voltage drop and ΔI is the current change at the beginning of the discharge phase. For PZC analyses, the electrochemical impedance spectroscopy (EIS) was carried out in the potential range of -0.3 to 0.3 V with an interval of 0.05 V. The frequency was scanned from 1 Hz to 10 mHz and each scan was repeated for 3 times at each potential. The data at 10 mHz in the third cycle were selected to calculate the differential capacitance C_d (F) according to the Equation 4.4,

$$C_d = \frac{1}{\omega Z''}$$ (Equation 4.4)

Where ω is the angular frequency and Z'' is the imaginary part of the impedance spectroscopy. The PZC was the value of the potential at which C_d reached the minimal.[110]

4.2.4 The modified Donnan model for batch-mode CDI

The modified Donnan model (mD) was employed to understand the role of surface functionalities. In traditional Gouy-Chapman-Stern (GCS) double layer model, a double layer formed on the solution side of the phase boundary contains a compact layer (Stern layer, or Helmholtz layer) and a diffuse layer. The thickness of the Stern layer is the diameter of solvent molecule while that of the diffuse layer is affected by solution concentration. Since dilute solution is commonly used in CDI, in which the length of the diffuse layer exceeds the micropore diameter, mD model is employed instead of

69

traditional GCS model, with the former considering the overlap of diffuse layer in micropore.

4.2.4.1 Equilibrium model

In mD model,[83, 84] the Stern potential ($\Delta\phi_S$, dimensionless) indicates the potential drop in Stern layer, while the Donnan potential ($\Delta\phi_D$, dimensionless) refers to the potential difference between outside and inside the micropore. For a CDI cell consisting two electrodes, assume each electrode is in potential balance before applying the voltage (i.e., $V_{cell} = 0$ V),

$$\Delta\phi_S + \Delta\phi_D = 0 \qquad \text{(Equation 4.5)}$$

Considering the immobile chemical charge (σ_{chem}, an estimated value of 100 mM is used for pristine anode and cathodes in this study) is in the charge balance, thus in micropore,

$$\sigma_{elec} + \sigma_{chem} + \sigma_{ionic} = 0 \qquad \text{(Equation 4.6)}$$

Where σ_{ionic} (mM) is the ionic charge and σ_{elec} (mM) is the electronic charge. σ_{elec} relates to the Stern potential ($\Delta\phi_S$) by,

$$\Delta\phi_S \cdot C_s \cdot V_T = \sigma_{elec} \cdot F \qquad \text{(Equation 4.7)}$$

Where C_s is the Stern capacity (0.145 GF/m^3, using the same value from references which also use micropore carbon as electrodes[78, 97]), V_T is the thermal voltage ($V_T = RT/F = 0.0256V$), and F is Faraday's number (96485 C/mol). σ_{ionic} relates to the Stern potential ($\Delta\phi_D$) by,

$$-2 \cdot c_\infty \cdot sinh(\Delta\phi_D) = \sigma_{ionic} \qquad \text{(Equation 4.8)}$$

Where c_∞ is salt concentration outside micropores (measured at $V_{cell} = 0$ V, 8.83 mM for pristine electrode). Equations 5.5 to 5.8 can be solved for both electrodes to determine

their $\Delta\phi_S$, $\Delta\phi_D$, σ_{elec} and σ_{ionic} at V_{cell} = 0 (4 equations and 4 variables for each electrode). The above coupled equations can be solved simultaneously by Matlab$^@$.

4.2.4.2 Ion-transport model

In a transport model,[62] the current I is given by

$$V_{cell} = I \times R + V_T \times (\Delta\phi_{D,A} + \Delta\phi_{S,A} + \Delta\phi_{D,C} + \Delta\phi_{S,C}) \quad \text{(Equation 4.9)}$$

Where subscript "A" and "C" refers to either anode or cathode, V_{cell} is 1 V at the charging phase, and R is the resistance in the system, which is determined by fitting the model to the data. Current I relates to electronic charge (σ_{elec}) by

$$v_{mi} \frac{\partial \sigma_{elec}}{\partial t} = -\frac{I}{F} \quad \text{(Equation 4.10)}$$

Where v_{mi} is active micropore volume of a single electrode (0.75 β cm^3 g^{-1}× 0.13g), and β is the ratio of active micropore volume to the total pore volume, which can be solved by fitting the model to data and kept the same (0.504 in this study) for all the calculations. To simply the calculation, we do not consider the change of pore volume among samples. In a batch-mode, ions balance for electrodes is as follows

$$v_{mi} \frac{\partial C_{ion,mi}}{\partial t} + v_{st} \frac{\partial C_\infty}{\partial t} = 0 \quad \text{(Equation 4.11)}$$

Where v_{st} is the volume of stirred tank (15mL), and $c_{ion.mi}$ is salt concentration in micropore (mM). $c_{ion.mi}$ relates to σ_{ionic} and c_∞ according to,

$$c_{ions,mi}^2 = \sigma_{ionic}^2 + 4 \cdot c_\infty^2 \quad \text{(Equation 4.12)}$$

Equations (4.6)(4.7)(4.8)(4.10)(4.11)(4.12) are applicable for both electrodes, while equation 4.9 is used for the whole cell. By coupling these equations, unknowns can be solved for each time interval (t=1s). (13 equations and 13 variables in total. Compared with the equilibrium model, the added variables in the transport model are $c_{ion.mi}$ and c_∞ for two electrodes and I for the cell). Different from the equilibrium model, c_∞ is a

variable in the ion-transport model. The salt concentration outside micropores (c_∞) is calculated by

$$c_\infty = \frac{1}{2}(c_{\infty,A} + c_{\infty,C})$$ (Equation 4.13)

Where $c_{\infty,A}$ and $c_{\infty,C}$ are the salt concentrations outside micropore contributed by the anode and the cathode, respectively.

4.3 Results and Discussion

4.3.1 Regeneration of ACF through thermal treatment.

The effects of thermal treatment temperatures under Ar atmosphere on SAC regeneration are shown in Figure 4.3. The electrodes lost more than 50% desalination ability (from ~6 to ~2.5 mg/g) after 20 cycles in the experimental conditions (Raw conductivity data and SAC data in the unit of mg/g are shown in Figure 4.4 and 4.5, respectively). The fast degradation may be caused by anode oxidation during cycling (no pretreatment was employed to remove dissolved oxygen, which can oxidize the anode under CDI working potential).[67, 70] Figure 4.3a also show that the degradation rates are slightly different for individual electrodes during the first 20 cycles. This experimental error may come from the weight error between different electrodes (± 0.01 out of 0.13 g causes ~ 15% error). However, since the same pair of electrodes is used before and after thermal treatment, the performance improvement is not affected by this weight error. Other than the weight error, the operation error for assembling cell each time (cell pressure, electrode alignment, etc.) and the small difference of surface chemistry between electrodes may also cause the fluctuation of the degradation rate. In this study, some error is intrinsic due to these factors, but the regeneration ability stemming from thermal

treatments is self-consistent. The inset of Figure 4.3a summarizes the SAC recovery rates (the difference of SAC retention rate Γ/Γ_0 (%) before and after thermal treatment) under different temperatures. Thermal treatment under all temperatures exhibits some SAC recovery ability. Generally, a trend is observed whereby the higher the temperature, the higher the regeneration ability. A thermal treatment temperature of 700 °C has the highest regeneration ability (60%), while the regeneration abilities at lower temperatures (200 to 500 °C) are also significant (~40%). Figure 4.3a shows that the thermally treated electrodes will lose the recovered SACs subsequently in the following cycles, and the degradation rate varies to some extent. The recovered SACs decrease sharply right after the thermal treatment (21st and 22nd cycles) except for the temperature of 500 °C, which may be caused by the experimental fluctuations before reaching the steady-state.[47] Considering the degradation rate at subsequent cycles (23rd - 30th cycles), the electrodes treated by 500 and 700 °C have higher stability while those treated by 200 to 400 °C have relatively lower stability. With similar regeneration abilities, lower temperatures are always preferred in industrial settings considering energy consumption and operation simplicity. Therefore, 300 and 500 °C are chosen to represent two different regeneration regimes to be further studied here.
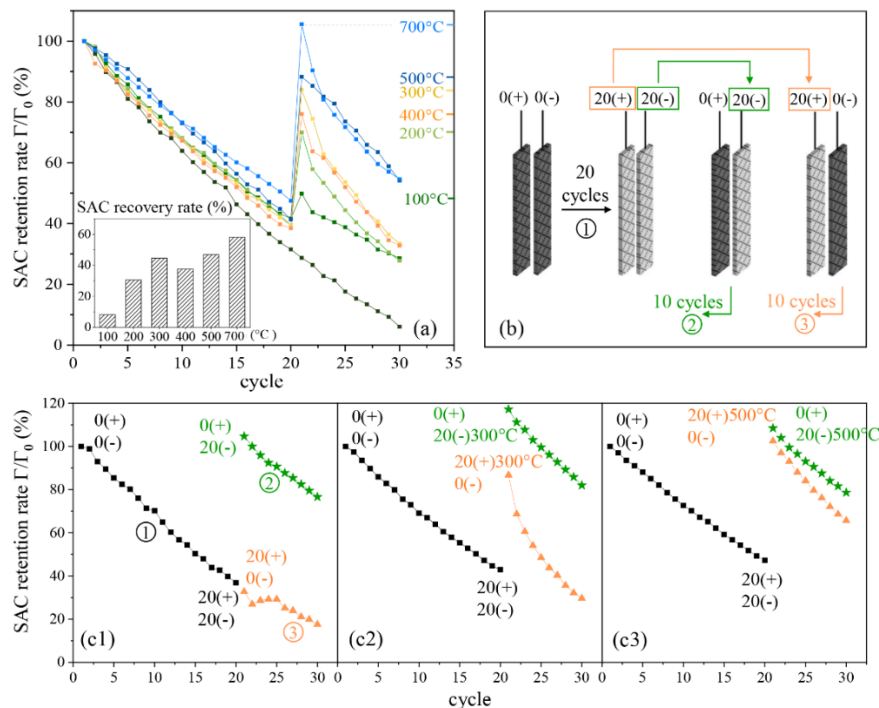
Figure 4.3 (a) The SAC retention rate (%) over cycling. The thermal treatment was done

after the 20th cycle. The inset is the SAC recovery rate (%) at different heating

temperatures. SAC recovery rate was the difference of SAC retention rate Γ/Γ_0 (%)

between the 21st cycle and the 20th cycle (before and after thermal treatment). (b) The

illustration of the systematic electrode replacement experiment. The fresh electrodes

were cycled for 20 cycles first. Then the aged anode (20(+)) and the aged cathode

(20(-)) were paired with a fresh electrode respectively and run for another 10 cycles. (c)

The cycling performance of systematic electrode replacement experiment (c1) without

thermal treatment. (c2) with thermal treatment at 300 °C. (c3) with thermal treatment at

500 °C.
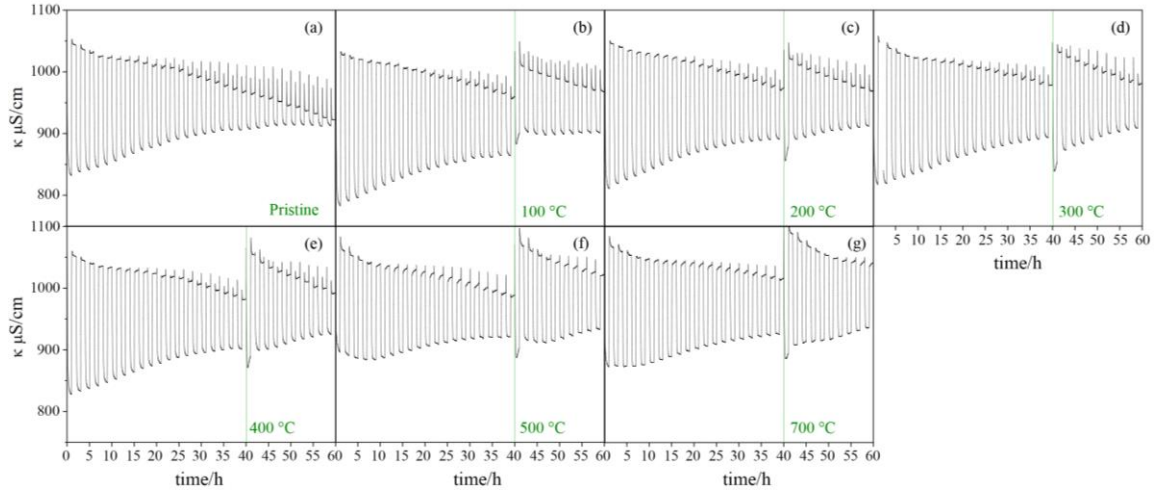
Figure 4.4 Measured conductivity change during cycling for calculations of SAC data used in Figure 4.3: The performance of electrodes decreases over cycling. The thermal treatment was done after the 20th cycle (Noted with green line).
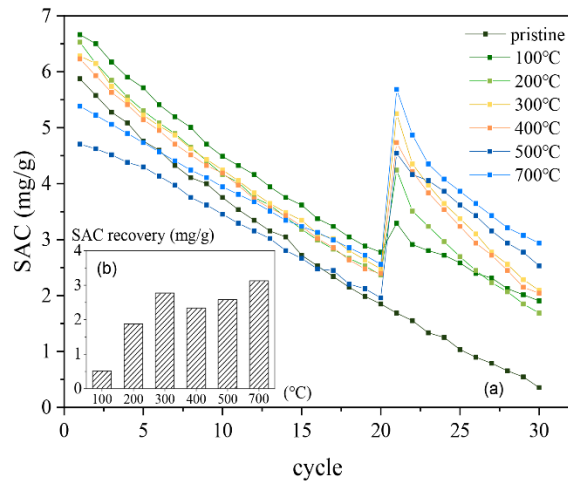
Figure 4.5 (a) The SAC (mg/g) over cycling. The thermal treatment was done after the 20th cycle. The inset is the SAC change (mg/g) at different heating temperatures. SAC change was the difference of SAC between the 21st cycle and the 20th cycle (before and after thermal treatment).

The impact of different gas conditions at 300 °C on SAC regeneration is illustrated in Figure 4.6. Three different gas atmospheres were tested, namely Air (oxidant), Ar (inert), and H_2 (5%, reductant). As shown in Figure 4.6, The SAC recovery rates and stabilities of aged electrodes treated in different gases are very similar. Thus, it can be learned that gas properties do not affect the regeneration performance when the heating temperature is low. This is maybe because that low temperature cannot provide enough energy for intensive interactions between gas molecules and carbon surface.[106]
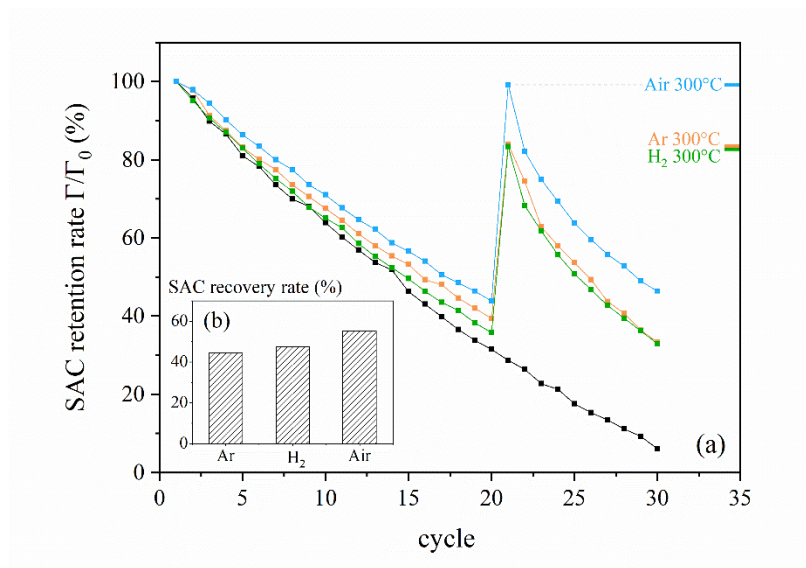
Figure 4.6 (a) The SAC retention rate (%) change over cycling. The thermal treatment was done after the 20th cycle. (b) SAC recovery rate (%) at different heating gas conditions. SAC recovery rate was the difference of SAC retention rate Γ/Γ_0 (%) between the 21st cycle and the 20th cycle (before and after thermal treatment.).

The roles of the anode and the cathode are analyzed separately by systematic electrode replacement experiments. The experiment process is illustrated in Figure 4.3b and the results are shown in Figure 4.3c (Raw conductivity data and SAC data in the unit

of mg/g are in Figure 4.7 and 4.8, respectively). Figure 4.3 c1 illustrates that when the aged anode is paired with a pristine cathode (orange triangles), the SAC keeps decreasing continuously. However, when the aged cathode is paired with a pristine anode (green stars), the SAC reaches the same level as the 1st cycle. This implies that almost all the degradation happens only at the anode while the cathode keeps the same SAC as the pristine ACF. Figure 4.3 c2 supports that the temperature of 300 °C can recover the SAC retention rate of the aged anode from 40% to 90%. However, although the recovered SAC at the 21st cycle is high, it decreases much faster than the pristine ACF, which causes the relatively low SAC retention rate at the 30th cycle. Figure 4.3 c3 illustrates that the temperature of 500 °C can recover nearly all the lost SAC for the aged anode without evident stability loss. This is consistent with the results in Figure 4.3 a, showing that 500 °C has a better regeneration ability. After the thermal treatment of 300 and 500 °C, the SACs of the cathode remain similar to the pristine electrode, implying that thermal treatment does not result in performance change of the cathode. (The recovery in SAC of >100% of the aged cathode at 300 °C is likely caused by a minor experimental error when the mass of replaced pristine electrode is accidently larger than others.) Furthermore, the impact of thermal treatment (500 °C) on pristine electrodes is studied. As seen from Figure 4.9, the pristine electrodes which are thermally-treated at 500°C before cycling have a similar performance compared with those untreated pristine electrodes. This illustrates that the thermal treatment only improves the performance of degraded anodes. From literature, the activation process usually involves temperatures higher than 500 °C during the manufacturing process of activated carbon.[120] Thus, it can be speculated that the volatile functional groups on the activated carbon surface which cannot tolerant high

temperature have already been removed during the manufacturing process. Therefore, the thermal treatment only improves the performance of degraded electrode as new volatile functional groups are formed during cycling and can be modified by thermal treatment (The connection between functional groups and performance is illustrated in the next section).

The stability degradation is likely caused by the Faradaic reactions occurring in both electrodes (e.g., carbon oxidation in the anode and oxygen reduction in the cathode).[79, 124] The systematic electrode replacement tests (Figure 4.3c) clarify that although Faradaic reactions occur in both electrodes, only the anode is degraded while the performance of the cathodes barely changes. Furthermore, the thermal treatment employed in this study seems to be an effective and simple method for the aged anode recovery. Therefore, the properties of the aged anode before and after thermal treatment is key to understanding the regeneration mechanism.
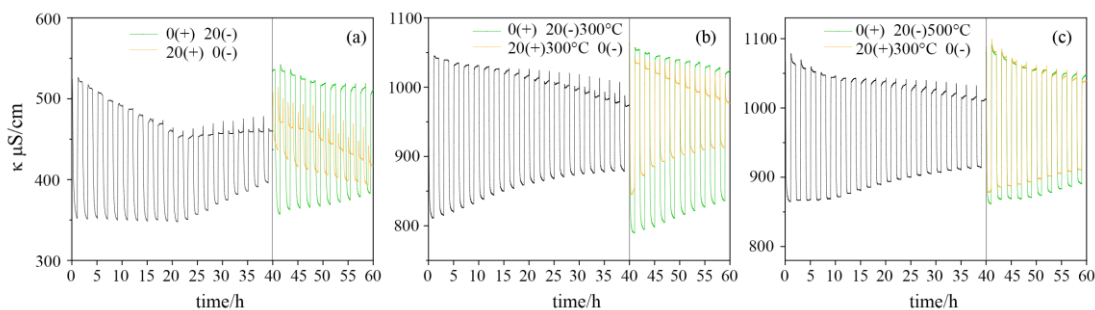
Figure 4.7 Measured conductivity change during cycling for calculation of SAC data used in Fig. 4.3c: The cycling performance of systematic electrode replacement experiment (a) without thermal treatment. (b) with thermal treatment at 300 °C. (c) with thermal treatment at 500 °C.
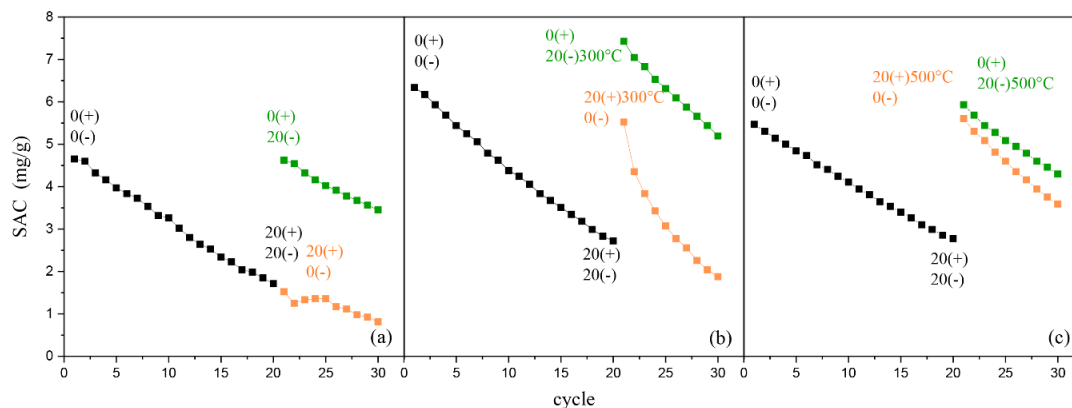
Figure 4.8 The cycling performance of systematic electrode replacement experiment (a) without thermal treatment. (b) with thermal treatment at 300 °C. (c) with thermal treatment at 500 °C. (Figure 4.7a and 4.8a show that when 5 mM NaCl solution is employed instead of 10 mM, the regeneration trend is similar. This means that thermal treatment also contributes to performance recovery at a lower salt concentration.)
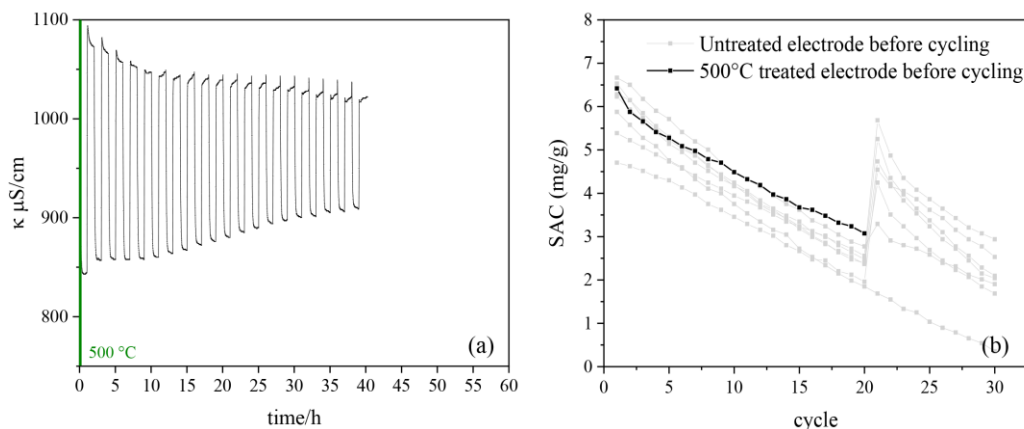
Figure 4.9 The impact of thermal treatment (500 °C) on pristine electrodes. (a) Measured conductivity. (b) Degradation of SAC compared with other untreated electrodes before cycling.

4.3.2 The impact of thermal treatment on surface functionality of aged electrodes

4.3.2.1 Oxygen-containing functional groups

Oxygen contents detected by XPS are shown in Figure 4.10a with the detailed deconvolution data available in Figure 4.11 and Table 4.1. The results indicate that the oxygen content increases from 3% to 11% in the anode after cycling. This increase suggests that oxygen-containing functional groups are formed during cycling, which can be supported by previous studies.[67, 101] After thermal treatment, the oxygen contents decrease to 7% and 6% at 300 and 500 °C, respectively, meaning that the formed oxygen functional groups are partly decomposed. As for the cathode, its oxygen contents remain nearly unchanged during the cycling and the heating, which is in good agreement with the results of Section 4.3.1 regarding desalination ability of the cathode. In the following parts, the cathode will not be discussed further due to its inactive role.

Oxygen-containing functional groups on the carbon surface can be categorized as acidic and basic. Carboxylic acid, carboxylic anhydride, lactone, phenolic hydroxyl, etc. contribute to the surface acidity, while chromene, ketone, pyrone, etc. give rise to surface basicity.[106, 118] Furthermore, basicity can also originate from the basal planes of carbon which can adsorb protons.[78] Boehm titration (Figure 4.10b) illustrates that the concentration of acidic groups in the anode doubles after 20 cycles' running (0.40 vs 0.17 mmol/g), which mainly comes from the formation of carboxylic and lactone groups. This is similar to results obtained by Chen el at.[125] Thermal treatment at 300 and 500 °C reduces the concentration of acidic groups to 0.3 mmol/g and 0.25 mmol/g, respectively, implying that these acidic groups are not stable and can be removed through thermal treatment, and

a relatively higher treatment temperature could result in more complete removal of these acidic functional groups. As for the basic groups, its amount fluctuates without a clear trend during the cycling and the heating of both electrodes (Figure 4.10c). Therefore, the variations of the oxygen contents mainly come from the variations of the acidic groups in this study. Figure 4.10d illustrate that the SAC is inversely correlated with the concentrations of oxygen functional groups and acidic groups in the anode. The removal of the surface functionalities (acidic groups) results in the regeneration of the desalination performance.

Different kinds of oxygen functional groups have different thermal stabilities. In general, functional groups containing two-oxygen atoms (carboxyl, lactones, etc.) are evolved as CO_2 at lower temperatures (100-800 °C), while these containing single-oxygen atom (phenols, quinones, etc.) are evolved as CO at higher temperatures (400-1000 °C).[106] In terms of acidity, strong acidic oxygen functionalities (such as carboxylic, anhydrides) start to decompose at lower temperatures (~250 °C), while weak acidic groups (such as phenolic) begin to decompose at relatively higher temperatures (~500 °C).[118, 126, 127] Compared with acidic groups, basic surface oxides decompose at even higher temperatures (900-1200 °C).[106] Therefore, it can be speculated that the decrease of acidic groups at 300 °C in this study is probably mainly from the partial decomposition of two-oxygen functional groups (e.g. strong acidic groups: carboxylic acids, carboxylate anions, etc.). At 500 °C, functional groups containing both one and two oxygen atoms (e.g. anhydrides, carboxyl, phenol, aldehyde, etc.) are further decomposed. However, this temperature is evidently not sufficient to remove all the functional groups. It can also be speculated that higher temperatures (>500 °C) are capable of decomposing more

functional groups, thus the desalination performance may see enhanced recovery. Despite the enhancement, one should realize that a certain concentration of surface functional groups is needed for carbon electrodes to ensure hydrophilicity, which facilitates water molecules to penetrate sufficiently into the pores.[117] Therefore, it is important to control surface groups at a reasonable concentration range to balance hydrophilicity and other critical properties of the electrode. On the other hand, the category change of surface functional groups may also affect the degradation rate after thermal treatment, which is also of interest for further studies.
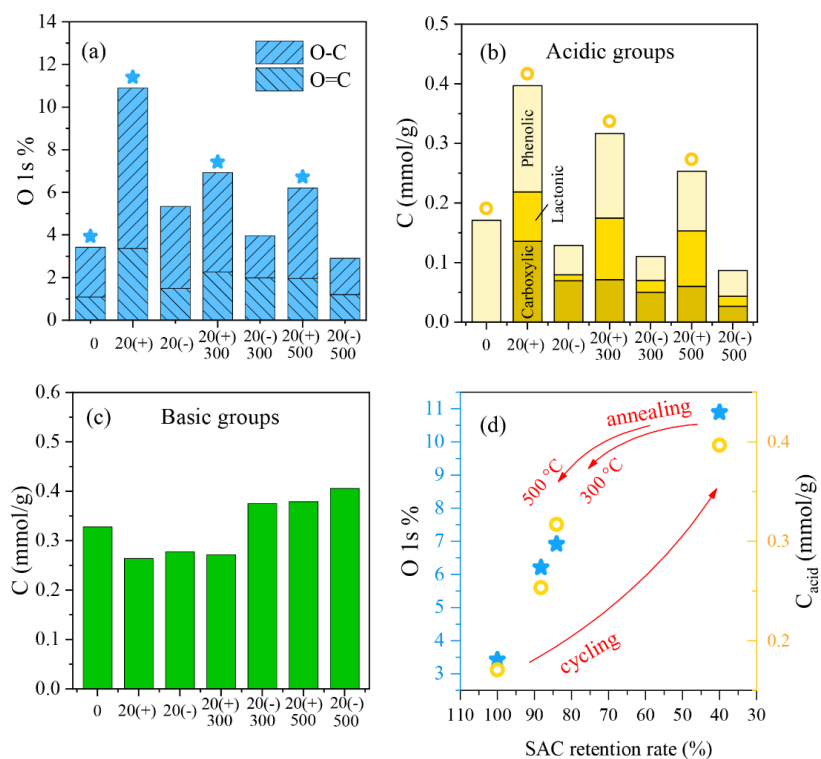
Figure 4.10 The impact of thermal treatment on the surface chemistry of electrodes. (a) Relative contents of functional groups in O 1s from XPS spectra. (b) Concentrations of acidic groups, and (c) basic groups. (d) Correlation between surface chemistry in anodes and SAC retention rate. The filled stars are O contents, and the hollow circles are concentrations of acid groups (marked data in Figure 4.10 a and b are plotted).
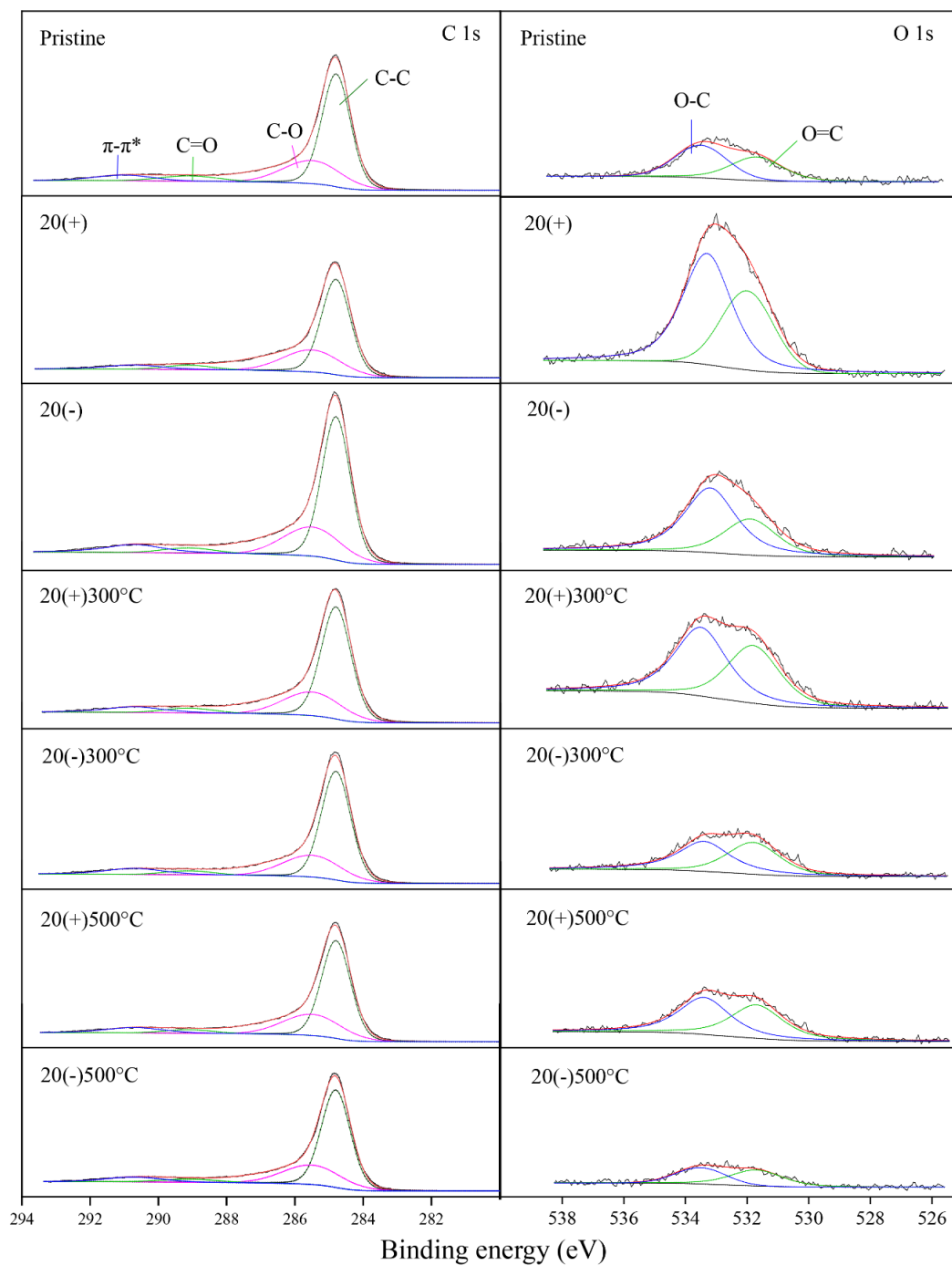
Figure 4.11 impact of thermal treatment on surface chemistry for electrodes through XPS deconvolution of C 1s region (left) and O is region (right). C 1s spectrum is deconvoluted into the following peaks: (1) Carbon in graphite/aromatics at 284.8 eV. (2) Carbon in phenols or ethers (C-O) at 285.5 eV. (3) Carbon in ketones or quinones

(C=O) at 287.2 eV. (4) Carbon in carboxyl, carboxylic anhydrides, or esters (O-C=O) at 289.1 eV. (5) Carbon in aromatic compounds at 290.7 eV (π-π* transition). O 1s spectrum is deconvoluted into the following peaks: (1) Oxygen in quinones, ketones or aldehydes (O=C) at 531.6 eV. (2) Oxygen in ethers or phenols (O-C) at 533.2 eV.

Table 4.1 Atomic concentration of functional groups in C 1s and O 1s from XPS spectrum

Sample	C 1s %				O 1s %	
	C-C, C-H	C-O	C=O	O-C=O	O-C	O=C
Pristine	55.51	24.15	5.76	5.29	1.09	2.336
20(+)	47.66	24.01	8.01	4.97	3.369	7.519
20(-)	53.58	24.11	6.34	5.14	1.491	3.846
20(+)300°C	52.08	23.56	6.29	5.22	2.255	4.661
20(-)300°C	55.97	23.98	5.63	5.21	1.987	1.961
20(+)500°C	52.47	25.24	5.68	5.04	1.953	4.258
20(-)500°C	57.12	24.37	5.33	4.89	1.206	1.698

Since oxygen concentration is low in general, the scale of C-O, C=O and O-C=O concentration variation in C 1s region is small. Thus, the concentrations of O-C and O=C from O 1s region are used for analysis.

4.3.2.2 Surface charges

The oxygen functional groups can act as surface charges for CDI electrodes, which is believed to be the major factor relating stability degradation.[93] To further study the role of functional groups and quantify the surface charges originated from these functional groups, the mD model was used to fit the desalination curve before and after the thermal treatment. Since the performances of cathodes and pristine electrode are similar, and the acidic/basic groups' concentrations are similar as well, we assume that the surface charges on the cathode and pristine electrode are the same. The PZC of the pristine electrode is -0.05 V (Figure 4.12), meaning that there is a small number of positive charges in the pristine electrode. Therefore, we assume the chemical charges (σ_{chem}) is 100 mM for the pristine anode and cathodes. We first fit the data of pristine electrodes to obtain the parameters for the CDI system (resistance, active micropore volume, etc). Then through only changing the quantity of immobile surface charges in the anodes, we fit the data of degraded and recovered electrodes (Figure 4.13). All the fitted values of the immobile surface charges are in the rational range compared to other studies.[78, 128] (With different assumed values of chemical charges, the fitted values of surface charges shift, but the trend is the same). This fitting result shows that the surface charges of the anode change from positive to negative (100 to -370 mM) after cycling, indicating that the formed acidic functional groups can significantly increase the concentration of negative surface charges. Simultaneously, the PZC is shifted from -0.05 to 0.08V. Since these negative charges on the aged anode can adsorb positive ions (co-ions for the anode), the higher applied voltage is required for compensating co-ion expulsion, thereby retarding counter-ion adsorption

in the charging phase. Therefore, performance degradation is coupled directly with the increase in acidic functional groups during cycling.

The thermal treatments of 300 and 500 °C reduce the chemical charges to -150 and -80 mM, respectively, while the PZC is shifted to 0.06 and 0.05V, respectively. Simultaneously, the conductivity curve also shows that the inversion effect is alleviated. The results support that thermal treatment causes the decomposition of oxygen-containing functional groups, thus decreasing the concentration of negative surface charges and thereby contributing to the regeneration of the electrodes. The results of surface charges also raise questions such as what is the connection between oxygen-containing functional groups (concentration, category, etc.) and surface charges, which warrants further investigations.
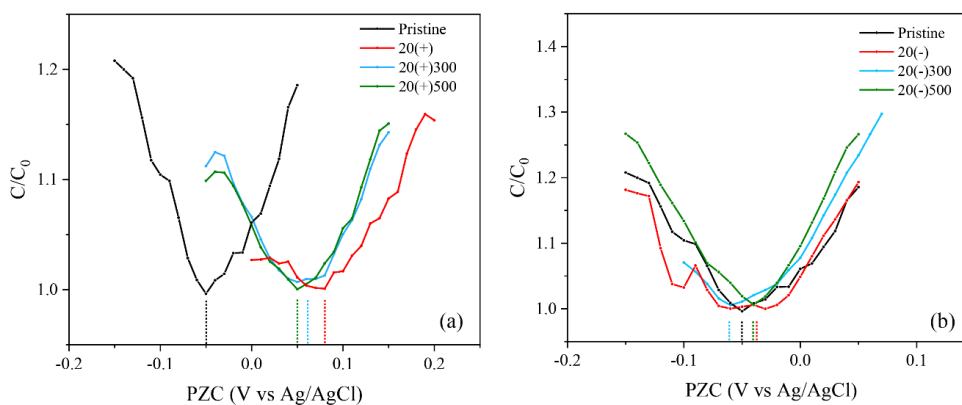
Figure 4.12 The impact of thermal treatment on PZC for electrodes
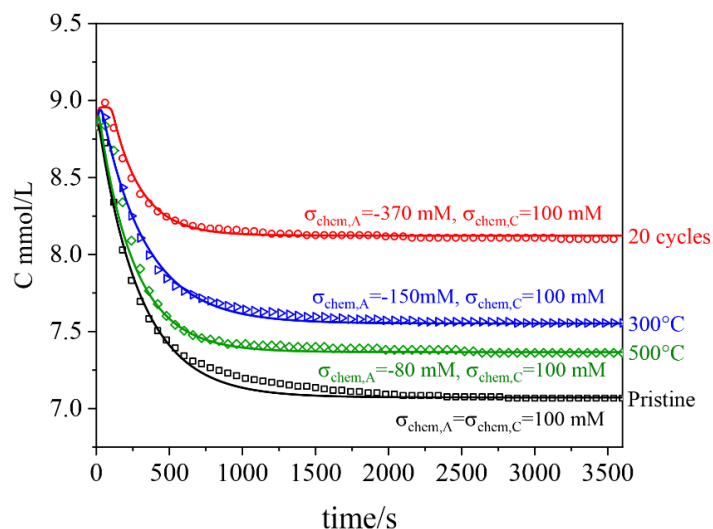
Figure 4.13 The mD transport model for batchmode CDI involving chemical surface

charge in both electrodes. Scatters are data. Lines are fits using the mD model.

4.3.3 The impact of thermal treatment on the physical properties of aged electrodes

4.3.3.1 Morphology

The morphology studied by SEM (Figure 4.14) shows that there is no visible fiber break or cracks on the carbon surface for all tested samples. Literature shows that some hairline cracks are observed on ACF surfaces after heating at 850 °C.[119] Our results support that the macro surface structure of carbon is well-preserved within the moderate-temperature regime (300-500 °C), though its surface functionality is significantly modified.
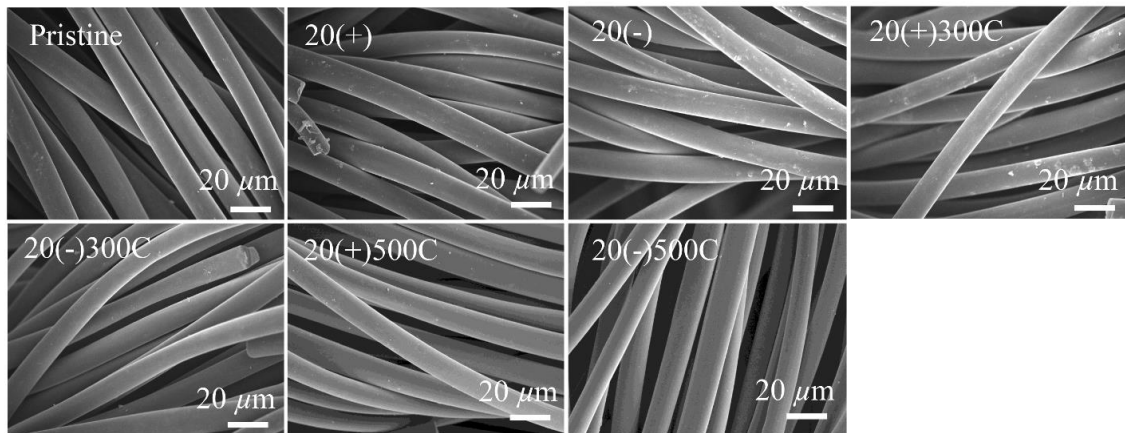
Figure 4.14 The impact of thermal treatment on surface morphology for electrodes

Since ACF consists of micropores where the Debye length is larger than the pore size, its SAC is more related to pore volume rather than the surface area.[89] Thus, the changes of pore volume before and after the thermal treatment are explored. As shown in Figure 4.16 the total pore volume of the anode decreases from 0.78 to 0.73 cm^3 g^{-1} after cycling. Thermal treatments at 300 and 500 °C increase the total pore volume to 0.75 and 0.77 cm^3 g^{-1}, respectively (Raw adsorption-desorption isotherm curves are in Figure 4.15). The increase at 300 °C is mainly from meso- and macropores, while the increase observed at 500 °C also has a significant contribution coming from micropores. This implies that in addition to the decomposition of functional groups, there may be a thermos-mechanical effect which also opens the pores up to some extent. Figure 4.18c (Green triangles) shows that the pore volume is in good correlation with SAC. It can be speculated that the formed functional groups and adsorbed co-ions occupy the active adsorption area after cycling,[43] causing the decrease of the SAC. The thermal decomposition of functional groups recovers the lost active area, increasing the SAC. However, the relative pore volume change is smaller than that of SAC (7% vs 60%). Since the SAC is theoretically

88

proportional to pore volume, the pore volume change may contribute to 11.7% (7/60) of the SAC loss/recovery.
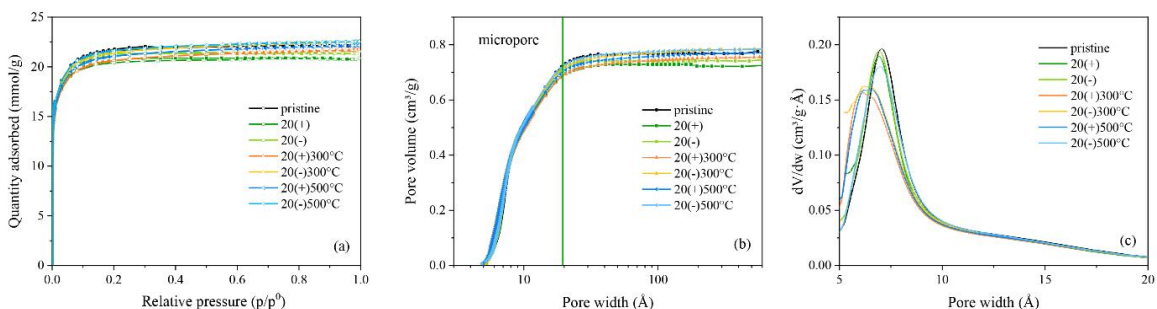
Figure 4.15 The impact of thermal treatment on: (a) Adsorption-desorption isotherm curve. (b) Pore volume change calculated from isotherm curve by the Horvath-Kawazoe (HK) model. (c) Pore volume distribution of micropore.

From Figure 4.15 b, the micropore volumes of electrodes are values at the intersections with green line (pore width smaller than 2 nm). The total pore volume of electrodes are values at the intersection of the right y-axis.
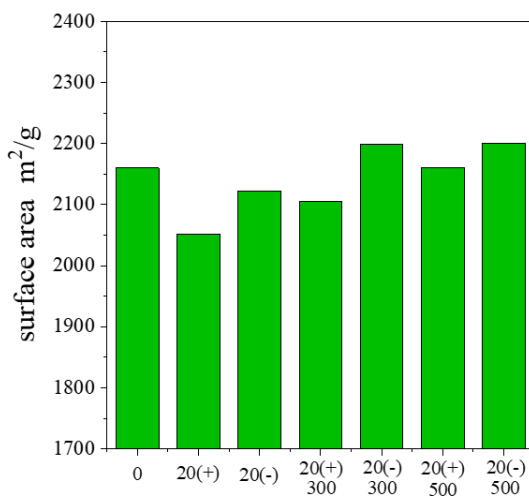
Figure 4.16 The impact of thermal treatment on surface area for electrodes

4.3.3.2 Resistance

The resistance change of electrodes tested by GCD is shown in Figure 4.18b. The resistance of the anode increases from 4.48 to 6.91 Ω after the cycling. Combining with XPS data, probably, the introduction of the excess surface functionalities cause the disruption of the conjugated pi network.[126] This agrees with other researchers who also see a resistance increase after cycling.[67] The resistance of the whole CDI system is tested by EIS (the Nyquist plot is in Figure 4.17). The total resistance (including setup, contact, and transmission line resistances) is 23 Ω for the CDI system in this study based on the equivalent circuit proposed by Qu et at.[91] Thus, the resistance of electrodes is estimated to account for ~40% of the total resistance. The increase of the anode resistance after cycling results in a growing asymmetry in the resistance of the electrodes. This may contribute to the asymmetric potential distribution, thus decreasing the SAC.

Figure 4.18b shows that the resistance is reduced to 5.76 and 4.94 Ω after heating at 300 and 500 °C, respectively. The reduction of resistance may be caused by two reasons. On one hand, surface oxides are decomposed during the thermal treatment process, thus the area for electrical connection is restored and the resistance is decreased.[126, 129] On the other hand, the aromatic hydrocarbon may also decompose during the heating, causing the reformation of C=C and more ordered carbon crystalline structure, thereby increasing the resistance.[106] Figure 4.18c illustrates that the SAC and the resistance of the anode are strongly correlated, which may be caused by the restoration of symmetric potential distribution. Therefore, the reduction of the resistance by the thermal treatment can recover the SAC.
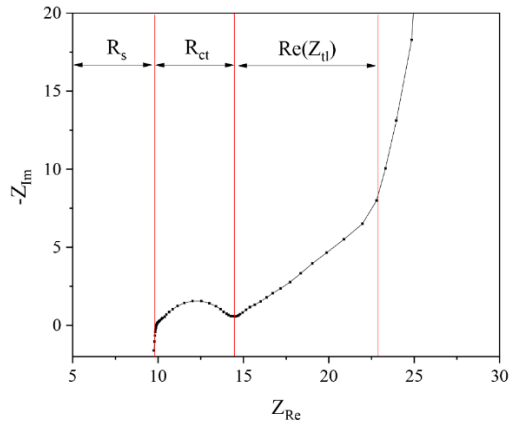
Figure 4.17 Nyquist plot of the CDI system with pristine electrodes

R_s: Set-up resistance

R_{ct}: contact resistance

Z_{tl}: transmission line impedance

4.3.3.3 Capacitance

The changes of CV curves before and after thermal treatment at 1 mV/s are plotted in Figure 4.18d. The current response of the pristine electrode is symmetric in the voltage window (-0.2 to 0.4 vs Ag/AgCl). The deformation of the CV curve happens in the anode after cycling. The deformation is likely caused by the negative surface charges as the current response is enhanced at a negative voltage window and is reduced at a positive voltage range. The asymmetric current response in the CV curve infers that the effective desalination potential window of the aged anode is shifted. In a desalination process, the anode works in a positive voltage window (~0.5 V when the applied voltage is equally distributed). As illustrated in Figure 4.18d, the aged anode has a lower capacitance (smaller integral area of CV curve) at a positive potential range (0.3-0.4 V) compared with that of the pristine electrode. Therefore, there is a decline in SAC of aged anode. The

91

thermal treatment increases the capacitance of the aged anode at the positive voltage window, subsequently recovering its performance.

CV curves at a scan rate of 5 mV/s are shown in Figure 4.18e. The capacitance of the aged anode at a higher scan rate (5 mV/s) decreases and the current spends a longer time to reach a plateau. This is affected by the resistance as the curvature of CV is decided by the time constant (RC). As the thermal treatment recovers the increased resistance of the anode (Figure 4.18b), the capacitance restoration at 5 mV/s becomes more evident accordingly. The overall capacitance change at the scan rate of 1 to 10 mV/s is shown in Figure 4.18f. In short, the capacitance variation agrees with the SAC degradation and regeneration, which is affected by the surface charges and resistance of the electrode.
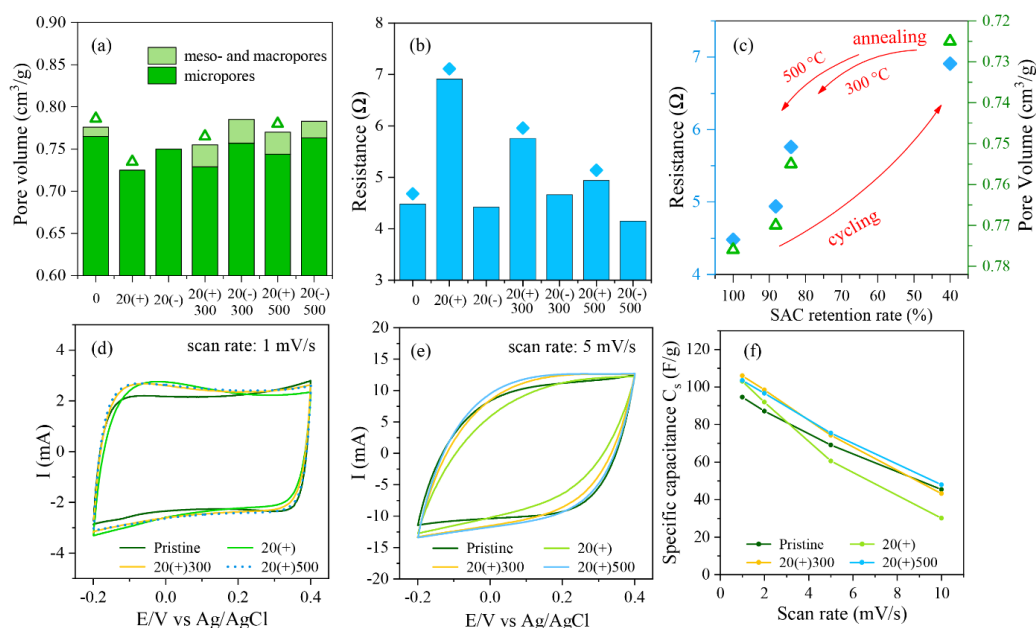
Figure 4.18 The impact of thermal treatment on (a) pore volume and (b) resistance of electrodes. (c) Correlation between physical properties in anodes and SAC retention rate. The filled diamonds are resistances, the hollow triangles are pore volume (marked data in Figure 4.18 a and b). (d) CV curves of anodes at a scan rate of 1 mV/s, and (e) 5 mV/s. (f) Specific capacitances of anodes at scan rates from 1 to 10 mV/s.
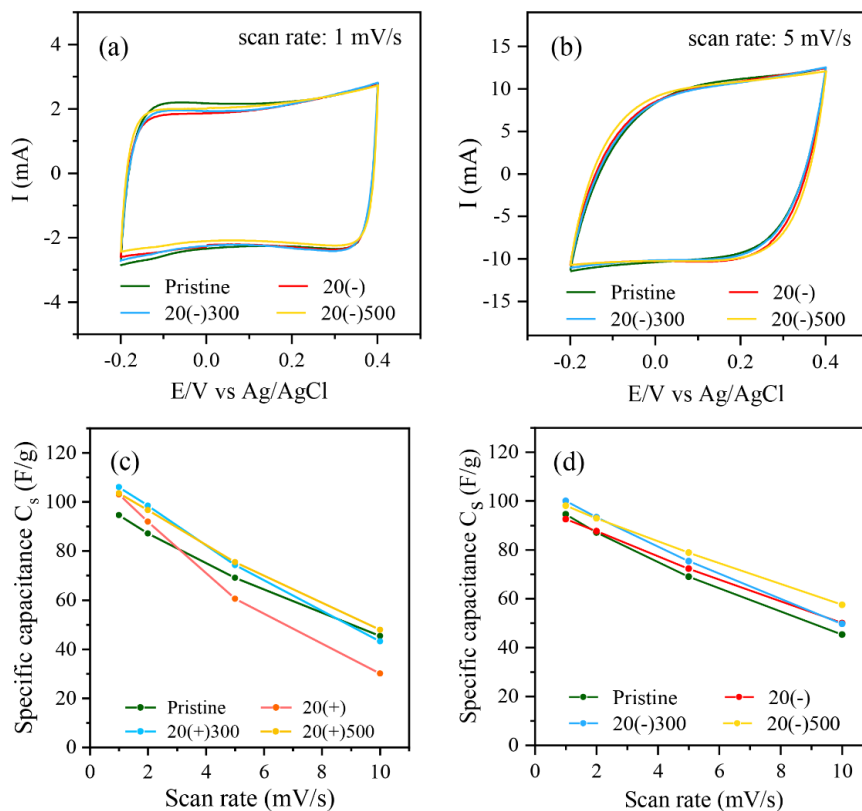
Figure 4.19 CV curves of cathodes at scan rate of (a) 1 mV/s. (b) 5 mV/s. (c) Specific capacitances of anodes at different scan rates. (d) Specific capacitances of cathodes at different scan rates.

4.3.4 Environmental Implications

Our study provides an industrially scalable method (thermal treatment) to recover the degraded performance of aged CDI electrodes. The suggested temperature (500 °C) functions in performance regeneration, as it can decompose some of the excess oxygen-containing functional groups, which are correlated with SAC through affecting some key properties (surface charges, pore volume, resistance, etc.) of electrodes. Based on the reported regeneration mechanism, other strategies based on the modification of surface

functionalizes can also be proposed for electrode regeneration such as ammonia treatment,[118] chemical methods (using reductants).[130, 131] Some of these strategies also hold potential for *in-situ* restoring the degraded anode.

Chapter V

The effect of electrode form and ion-storage mechanism on the desalination performance

5.1 Introduction

Carbon-based material is the most commonly used electrode material for commercial electrochemical capacitor and has the greatest potential to be commercialized as CDI electrode.[115, 132, 133] Activated carbon fiber (ACF) is one of the most popular carbon-based material and has been studied for years.[68, 124] Compared with granular activated carbon (GAC), ACF has less macropore and has uniformly developed micropore and mesopore of higher volumes as shown in Figure 5.1a (The product used in our experiment is Grade20). The SEM picture of ACF (Figure 5.1b) also supports that there are compact pores on the surface of ACF and most of pores are mesopores and micropores. Since micropore and mesopore exhibit higher salt adsorption capacity than macropore,[66, 134] ACF is expected to have high salt storage capacity. ACF is in the form of fiber, and it can be woven to the free-standing structure such as cloth or felt. The SEM pictures of ACF felt and cloth are shown in Figure 5.1 c and d, respectively. Compare with ACF felt, ACF cloth is denser and regular. Both ACF cloth and felt have free-standing structure. Therefore, ACF has the advantage that it can be employed directly as electrodes without any pretreatment or fabrication process.[73, 135, 136] Differently, binder and conductive material are always employed in commercial electrode fabrication process for GAC,[60, 137] and it can make the carbon electrode a very compact structure. Compared with directly employed ACF, this fabrication process decreases the thickness of the electrode, thereby

decreasing the resistance and distance of ion transportation. However, the binder and the conductive additive employed in the fabrication process increase the electrode weight and may also occupy the active sites of the active material. Therefore, it is of interest to compare which electrode form is better for CDI application.
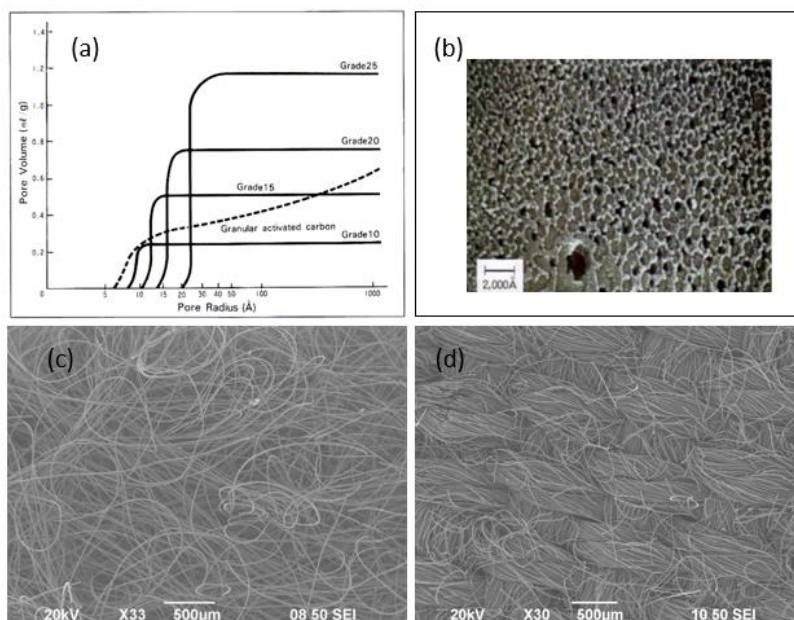
Figure 5.1 (a) Pore size distribution of GAC and ACF. (b) SEM picture of ACF surface. (c) SEM picture of ACF felt. (d) SEM picture of ACF cloth. (a) and (d) are from Kuraray company.[138]

On the other hand, novel intercalation materials also gain attention in the application of water desalination in recent decades.[53, 139, 140] The ion-storage mechanism of carbon-based material based on the double-layer formation, while intercalation materials store ions via ion insertion into a host lattice. One specific example of intercalation materials is Prussian Blue (PB) and its analogues (PBAs, e.g. NiHF, CuHCF). This kind of material is proven to have higher differential charge values than carbon-based materials. Since

PB(As) have crystal lattices with fixed dimensions, it also shows ions selectivity during ion storage.[141, 142] Another intercalation material is MXenes (e.g. $Ti_3C_2T_x$, T refers to a surface-terminated group such as O, OH or F), which are 2D materials, and can store ions of different sizes and valences.[143-145] MXenes are fabricated by extracting "A" layers from layered carbides or carbonitrides, known as MAX phases (M represents a transition metal, A refers to a III A or IV A element, X represents C and/or N). The excellent properties of MXenes such as high electrical conductivity, large interlayer spacing make it a promising material for energy storage. Since only cations or anions can react with intercalation materials, intercalation materials have higher selectivity compared with carbon-based material. This implies that the co-ion repulsion happened during the charging phase for carbon-based electrodes, a phenomenon which decreases the charge efficiency, can be possibly alleviated for intercalation material. However, there is a lack of direct comparison between carbon-based material and intercalation material under similar experimental conditions regarding to the desalination performance.[115]

In this chapter, ACF felt is used as reference electrode. ACF slurry (made by conventional fabrication process) and MXene are compared with ACF felt respectively in a single-pass mode CDI system under similar experimental conditions. The important performance metrics (SAC, energy consumption, charge efficiency, etc.) in CDI technology are studied to compare their performance. The modified Donnan model and electrochemistry tests are employed to further analyze the performance difference. To end this, the strength of each material and their potential applications in water desalination are discussed.

5.2 Material and methods

5.2.1 Single-pass mode CDI system

All the tests in this chapter are run in a single-pass mode CDI system as illustrated in Figure 5.2. The salt solution in the reservoir singly pass through the CDI reactor by using a peristaltic pump, after which the salt solution is discarded. The reservoir contained 1 L of 10 mM NaCl to simulate brackish water and the flow rate was 0.5 mL min^{-1}. The conductivity meter (Jenway, 4520, UK) was located at the exit of the CDI and the micro-probe was employed to make sure the instantaneous conductivity measurement of the effluent. The conductivity at outlet was recorded at time interval of 1 s. The voltage of the CDI cell was controlled by a potentiostat (VMP300, Biologic Technologies, France).

The CDI cell had a symmetrical structure and was designed as a flow-by architecture. As shown in Figure 5.2, two electrodes (3×3 cm^2) were placed in parallel and separated by a plexiglass spacer (0.5 mm), where salt water flows by. Each electrode was covered by a separator (celgard 3501, NC, USA) with the size of 3.5×3.5 cm^2. Two titanium plates were used as current collector and the whole cell was covered by two plexiglass panels. The rubber plates were also added to make the easy seal of the CDI cell.
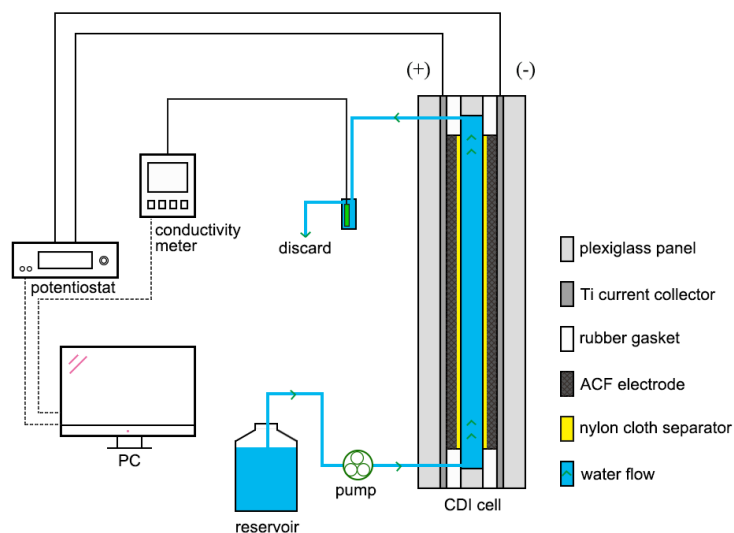
Figure 5.2 Schematic illustration of the single-pass mode CDI system

5.2.2 Electrode preparation

The pristine activated carbon felt (CH900-20, Kuraray, Japan) woven by ACF is used as reference electrode. The ACF felt was peeled to the fixed weight of 0.033 ($\pm$0.001) g. Then the peeled ACF felt were tested in both constant voltage mode and constant current mode. In constant voltage mode, the charging and the discharging phases last for 10 minutes. The voltages of 0.6, 0.8, 1.0 and 1.2 V are used for the charging phase, while the cell is short-circuited in the discharging phase. Three repeated cycles were run at each voltage and the data in the 3rd cycle is used for performance study. In constant current mode, the charging and discharging phases last for 8 minutes under the current of 2/-2, 3/-3, 4/-4 mA. The voltage limit is set as 0 and 1.6 V. 5 cycles were repeated at each current and the data in the 4th cycle is used for calculation.

To make ACF slurry electrode, the pristine ACF was first cut and then milled in a mortar into ACF power. After that, ACF powder, carbon black and polyvinylidene

fluoride (PVDF) were weighed in the ratio of 8:1:1. These three materials were added into the N-methyl pyrrolidinone (NMP) in the order of PVDF, carbon black and ACF power with the time interval of ~30 min during the stirring. The mixture was stirred for another 4 hours to ensure the homogeneity. After that the ACF slurry was coated on the graphite foil. The electrode films were dried in an oven overnight at 60 °C. The CDI electrode is obtained by cutting the dried film into 3×3 cm^2 (the weight of active material, namely ACF powder, is 0.033g). The ACF slurry electrode was tested in the constant voltage mode under the voltage of 1 V.

The MXene film is provided by Haibo Hu in Anhui University. The synthesis process of MXene follows their previous method.[146] They first prepared colloidal solution containing fully delaminated few-layered $Ti_3C_2T_x$ flakes (0.1 mg/ml) with an average size of ~ 1.0 µm, as shown in Figure 5.3a. A SEM photo of the fully delaminated few layered $Ti_3C_2T_x$ flakes is shown in Figure 5.3b. Then the suspension was deposited on the filter paper by vacuum-assisted deposition. After washing by DI water and heating at 80 °C, the filter paper can be easily peeled off and the freestanding MXene can be obtained. The thickness of the MXene film depends on the loading amount of $Ti_3C_2T_x$ flakes, is ~40 µm in this study. The freestanding MXene film was cut into 3×3 cm^2 (0.033g) and used only for the cathode, while the same size ACF felt was used for the anode. The CDI cell with MXene cathode was tested in both constant voltage mode and constant current mode in the same operation conditions with the reference ACF felt electrodes except that one more charging/discharging current of 1/-1 mA is added.
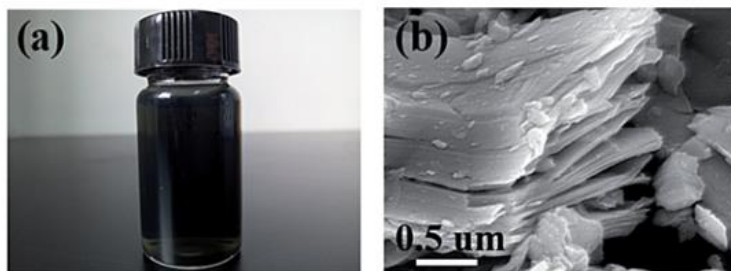
Figure 5.3 (a) by mild sonication in water, the exfoliated multi-layered MXene powders delaminate forming a stable colloidal solution containing fully delaminated few layered $Ti_3C_2T_x$ flakes; (b) a SEM photo of the fully delaminated few layered $Ti_3C_2T_x$ flakes, from ref [146]

5.2.3 Electrochemical characterization

The capacitance of electrodes was tested by cyclic voltammetry (CV) method in a conventional three-electrode system. Electrodes were cut into 1×1 cm^2 pieces before tests. A Pt plate of the same size and an Ag/AgCl electrode were employed as the counter and the reference electrode, respectively. 1 M NaCl was used as the electrolyte. Scan rates of 1, 2, 5, 10, 20 and 50 mV s^{-1} were conducted with the potential window of -0.2 to 0.4 V (vs Ag/AgCl). The gravimetric capacitance C_s (F g^{-1}) was calculated using the Equation 5.1.

$$C_s = \frac{\int i dV}{2v \Delta V M} \qquad \text{(Equation 5.1)}$$

Where i (A) is the charge/discharge current, ΔV (V) is the potential window, v (V s^{-1}) is the scan rate and M (g) is the mass of the sample at working electrode.

The resistance of the whole CDI cell was studied by the electrochemical impedance spectroscopy (EIS). The 10 mV amplitude sinusoidal potential perturbation was applied.

The frequency was scanned from 1 MHz to 10 mHz. The CDI cell was filled with 1 M NaCl during the test.

5.2.4 CDI performance study

To determine the performance of the electrodes, the salt removed over one cycle (ΔN_d, mmol) is calculated,

$$\Delta N_d = \Phi \times \int (C_0 - C)\, dt \qquad \text{(Equation 5.2)}$$

Where C_0 and C (mmol L^{-1}) are the constant influent and changing effluent concentration, respectively. Φ (L s^{-1}) is the volume flow rate. The SAC Γ (mg g^{-1}) was calculated by the Equation 5.3,[116]

$$\Gamma = \frac{\Delta N_d \cdot M}{m} \qquad \text{(Equation 5.3)}$$

Where M (g mol^{-1}) is the molar mass of the salt, and m (g) is the mass of the two electrodes. The threshold of the concentration (C_{thresh}, water below which concentration was defined as desalinated water, while above which concentration was defined as concentrated water) was chosen to make water recovery between ~50%. The average concentration reduction (Δc, mmol L^{-1}) was given by [72]

$$\Delta c = \frac{\Delta N_d}{V_d} \qquad \text{(Equation 5.4)}$$

Where V_d (L) is the volume of desalinated water. The charge efficiency (Λ) was given by

$$\Lambda = \frac{F \cdot \Delta N_d}{\int I\, dt} \qquad \text{(Equation 5.5)}$$

Where F is Faraday's constant (96485 C mol^{-1}), and I (A) is the current in the charging phase. The volumetric energy consumption (E_v, Wh m^{-3}) was calculated by [72]

$$E_{in} = \int IV dt \quad Where\ IV > 0 \qquad \text{(Equation 5.6)}$$

$$E_{out} = \int IV dt \quad Where\ IV < 0 \qquad \text{(Equation 5.7)}$$

$$E_v = \frac{E_{in} - \eta E_{out}}{V_d} \qquad \text{(Equation 5.8)}$$

Where E_{in} (Wh) and E_{out} (Wh) are the total energy input and output, respectively, and were calculated by the current-voltage curve in the charging and discharging phases, respectively. η (0-1) is the fraction of E_{out} actually recovered. In this study, only the condition of $\eta=1$ was calculated. Since no extra pressure is input into the system except for a small pump, the pressure is not considered in total energy consumption. One example of energy consumption calculation is illustrated in Figure 5.4. When the constant current (Figure 5.4c) is applied, the electrolyte concentration (Figure 5.4a) and CDI cell voltage (Figure 5.4b) vary accordingly. The power (Figure 5.4d) equals current times voltage. The time integral of power is the energy. E_{in} and E_{out} are the energy consumption in charging phase and the energy which can be recovered in the discharging phase, respectively.
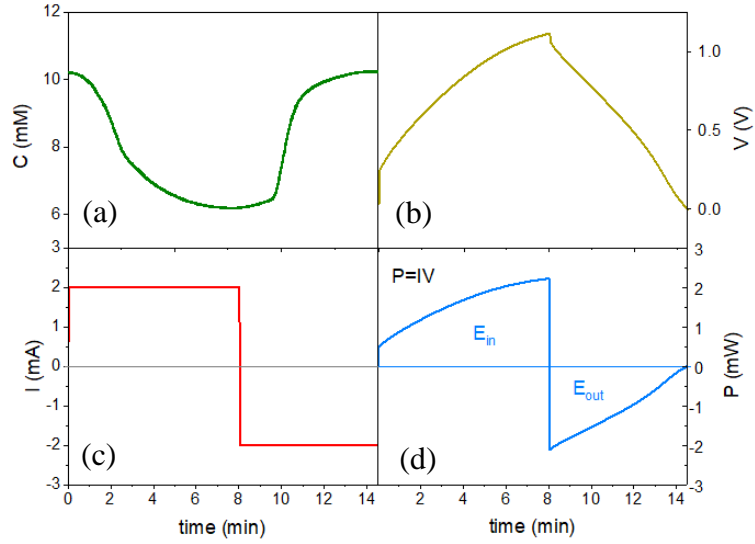
Figure 5.4 Calculation example of energy consumption (ACF felt electrode in 2/-2 mA constant charging/discharging mode) The variation of (a) electrolyte concentration, (b) CDI cell voltage, (c) applied constant current, and (d) power.

5.2.5 The modified Donnan model for single-pass mode operations

The mD model described in chapter 2 section 2.3.4 is used, which includes the potential drop at electrode ($\Delta\phi_{ele}$) and consumed for ions transfer in spacer ($\Delta\phi_{sp}$). In addition, the potential consumed for capacitance (V_{cap}) and resistance (V_{res}) over time is calculated by

$$V_{cap} = 2 \cdot V_T \cdot (\Delta\phi_D + \Delta\phi_S) \qquad \text{(Equation 5.7)}$$

$$V_{res} = I \cdot R_{ext} + 2 \cdot V_T \cdot (\Delta\phi_{elec} + \Delta\phi_{sp}) \qquad \text{(Equation 5.8)}$$

Since the sum of V_{res} and V_{cap} is the applied voltage, the instantaneous voltage distribution can be obtained by these two equations.

5.3 Results and discussion

5.3.1 The effect of fabrication process on desalination performance

The conductivity variations of ACF felt under constant voltage mode and constant current mode are shown in Figure 5.5. As shown in Figure 5.5b, in the beginning of the constant voltage mode, the effluent conductivity keeps decreasing as the fresh electrodes are adsorbing the salt ions. Then the effluent conductivity increases gradually as the adsorbed salt amount is approaching the adsorption capacity of the electrodes. As expected, a higher voltage causes a higher magnitude of the conductivity variation. In constant current mode (Figure 5.5d), the effluent concentration is more stable as the applied constant current translates into a constant ionic current in the cell, which is correlated with the adsorption speed of salt ions. A higher current causes a lower effluent concentration in the charging phase and a higher effluent concentration in the discharging phase.
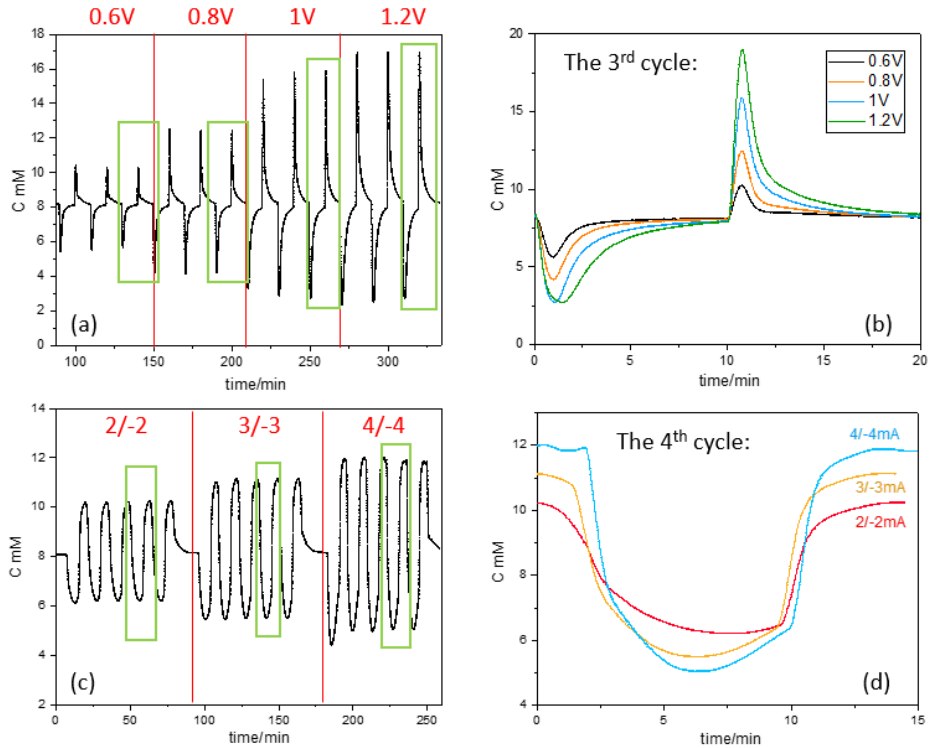
Figure 5.5 (a) Conductivity variation of ACF felt in constant voltage mode. (b) The 3rd cycle of constant voltage mode. (c) Conductivity variation of ACF felt in constant current mode. (d) The 4th cycle of constant current mode

The conductivity variations of ACF slurry in constant voltage mode under 1 V show the similar trend with that of ACF felt, as seen from Figure 5.6a. Compared with ACF felt, ACF slurry electrodes result in a lower effluent concentration in the charging phase (Figure 5.6b). Figure 5.6c also shows that the s of ACF slurry is a little higher than that of ACF felt (8.1 vs 7.5 mg). This means that the conventional fabrication method leads to a higher desalination capacity of the electrode material in the experimental conditions. The charge efficiency of ACF slurry electrodes is also higher (~80%), while that of the ACF felt electrodes is only ~60%. As for the energy consumption, Figure 5.6d implies that with the same energy input (~70 kWh/m^3), ACF felt electrodes can achieve the

average concentration reduction of ~1.5 mM while ACF slurry electrodes can achieve ~2.0 mM. All these CDI performance indicators illustrate that the fabrication process strongly affects the desalination performance of the electrodes. Compared with the direct employment of the woven materials, the conventional slurry method not only improves the SAC, but also increases the charge efficiency, and saves the energy consumption of the CDI cell in the experimental conditions.
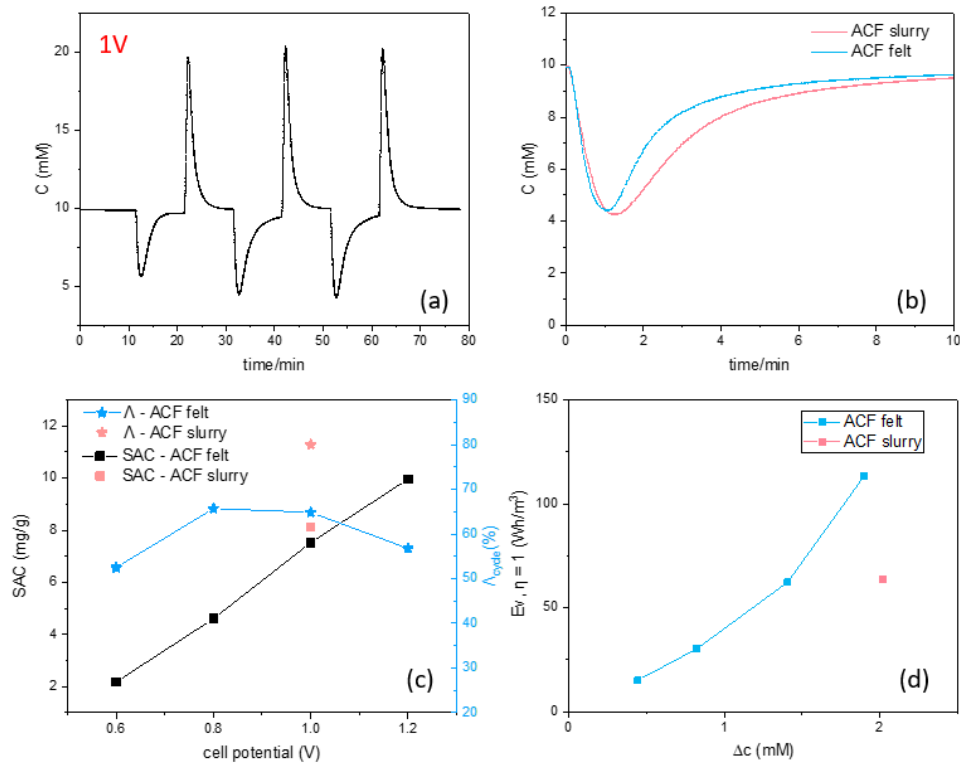
Figure 5.6 (a) Conductivity variation of ACF powder in constant voltage mode. (b) The comparison of the conductivity variation between ACF felt and ACF slurry. (c) The energy consumption of ACF felt and ACF slurry. (d) The SAC and charge efficiency of ACF felt and ACF slurry

5.3.2 The impact of fabrication process on the physical properties of electrodes

The conductivity variations of ACF felt and ACF slurry are fitted by mD model, as shown in Figure 5.7 a and b. The potential distribution over time is also calculated from the fitted model. As illustrated in Figure 5.7c, when using ACF slurry electrodes, more applied potential is spent for ions storage (V_{cap}) rather than resistance (V_{res}), compared with that of ACF felt electrodes. This explains the reason why the charge efficiency is higher and the energy consumption is lower for ACF slurry electrodes. EIS study also supports that the contact resistance (the diameter of the semicircle) of the CDI cell using ACF slurry electrodes is much smaller than that using ACF felt electrodes. Since these two electrodes use the same active material and only fabrication method is different, electrical resistance is the main difference between them, while other key factors such as surface area, pore distribution are the same of these two electrodes. This implies that the conventional fabrication process can contribute to a better desalination performance via improving the conductance of the electrodes. This is in accordance with others who found that the electrical conductivity of the electrode materials is linearly related to their electrosorption capacity and charge efficiency.[147]

The large resistance of ACF felt should be caused by its loose structure. As shown in Figure 5.1c, single fibers inside ACF felt are tangled but not are tightly contacted with each other. The overall resistance of ACF felt can be large due to the loose contact between fibers. However, as for ACF slurry, the binder physically connects every single fiber, decreasing the resistance evidently. Therefore, the charge efficiency and desalination performance of ACF slurry are improved.

The experimental and the modelling results illustrate that with the same active material, the electrical conductivity of the electrode is a key factor during the fabrication process. Considering the industrial application, the increase of the loading amount of electrode materials, which boosts the productivity, can decrease the conductance of the electrode, thus increasing the energy consumption. Therefore, a good fabrication method is important to sufficiently decreasing the resistance meanwhile achieving a high productivity. In this preliminary study, only one loading amount of electrode material is studied. It is of interest to find a good fabrication methods in the future when loading amounts and electrode conductivity are both considered. [148]
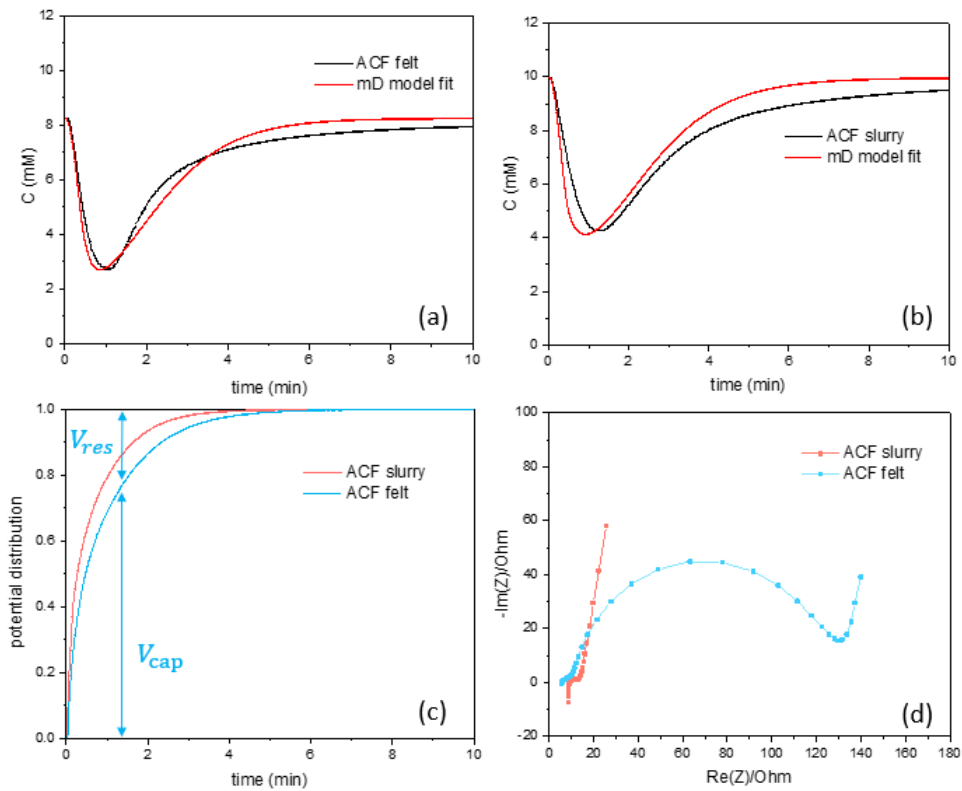
Figure 5.7 The fitting by mD model of (a) ACF felt, and (b) ACF slurry. (c) The potential distribution over time of ACF felt and ACF slurry. (d) The system resistance of ACF felt and ACF slurry

5.3.3 Performance comparison between ACF and MXene

The conductivity variations when using MXene as cathodes under constant voltage mode and constant current mode are shown in Figure 5.8. In constant voltage mode (Figure 5.8b), the conductivity curve of MXene spent more time reaching the lowest concentration compared with ACF felt electrodes (Figure 5.5b). Generally, the gap of the V-shape curve in the charging phase of MXene is shallower and wider. This implies that the CDI cell with MXene cathode has lower desalination speed and needs more time to reach its maximum capacity under constant voltage mode. In constant current mode, the CDI cell with MXene cathode spent less than 8 min reaching the voltage limit under the charging current of 3 and 4 mA. Compared with ACF felt cathode, the effluent concentration of MXene cathode is more stable.
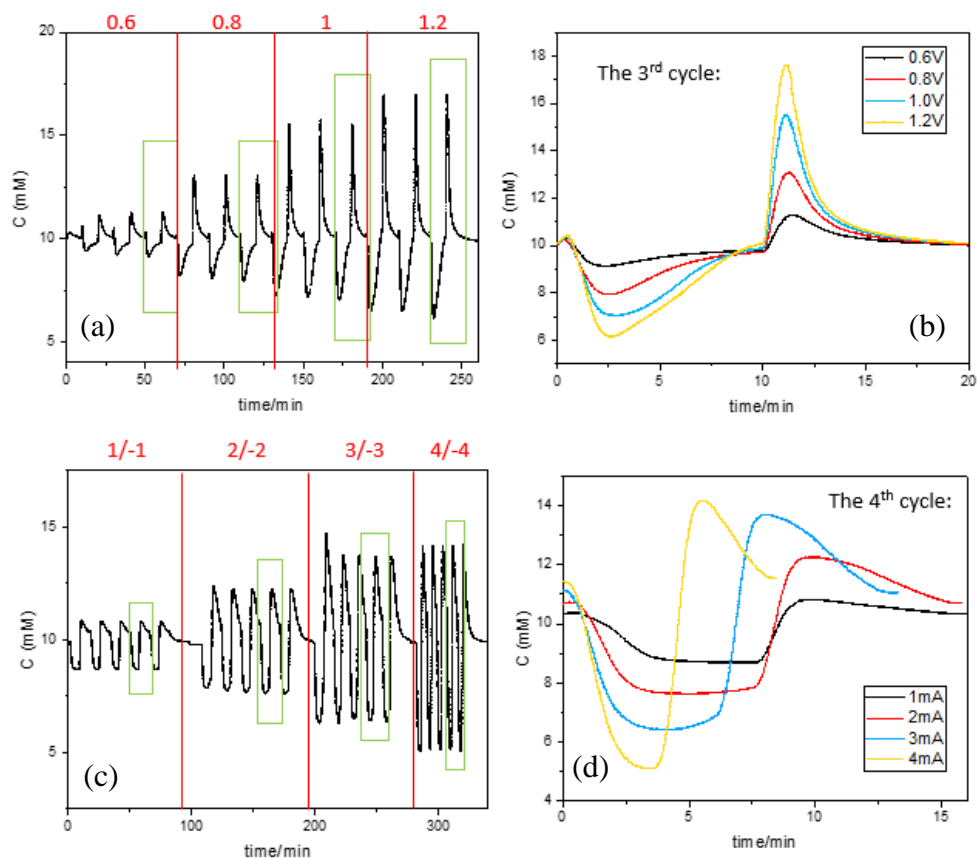
Figure 5.8 (a) Conductivity variation by employing MXene as cathode in constant voltage mode. (b) The 3rd cycle of constant voltage mode. (c) Conductivity variation by employing MXene as cathode in constant current mode. (d) The 4th cycle of constant current mode

The performance comparison between MXene and ACF felt electrodes are shown in Figure 5.9a. As illustrated in Figure 5.9a, the SAC of MXene cathode is smaller than that of ACF felt cathode under constant voltage mode. The SAC of MXene cathode is ~7 mg/g under 1.2 V while that of ACF felt is ~10 mg/g. The charge efficiency of MXene cathode is smaller than that of ACF felt cathode under the voltage between 0.6-1.0 V but higher under 1.2 V (Figure 5.9c). As for the energy consumption shown in Figure 5.7e, with

similar energy input, MXene cathode shows similar average concentration reduction under voltage range of 0.6-1.0 V while show a little higher average concentration reduction under voltage 1.2 V in constant voltage mode compared with ACF felt cathode. The performance indicators of constant voltage mode imply that ACF felt cathode has better performance at voltages below 1 V. Although the SAC of ACF felt cathode is higher than that of MXene cathode at 1.2 V, the energy consumption is also higher. Furthermore, ACF felt cathode also has a faster desalination rate compared with MXene cathode, which is recognized as one of advantages of carbon-based material.[115]

The situation is different under constant current mode. The SAC of MXene cathode is a little higher than that of ACF felt cathode under the constant current of 2 and 3 mA but much smaller under 4 mA (Figure 5.9b). At 4 mA, the CDI cell with MXene cathode only spend ~4 min reaching the voltage limit, before which the electrodes are not saturated by salt ions. Moreover, the charge efficiency of MXene cathode is evidently higher than that of ACF felt electrodes under the experimental current range (Figure 5.9d). As illustrated in Figure 5.9e, the average concentration reduction of MXene cathode is higher than that of ACF felt under the constant current mode, and the difference is even larger at higher charging current. The performance indicators illustrate that MXene has better desalination performance than ACF felt under constant current mode.
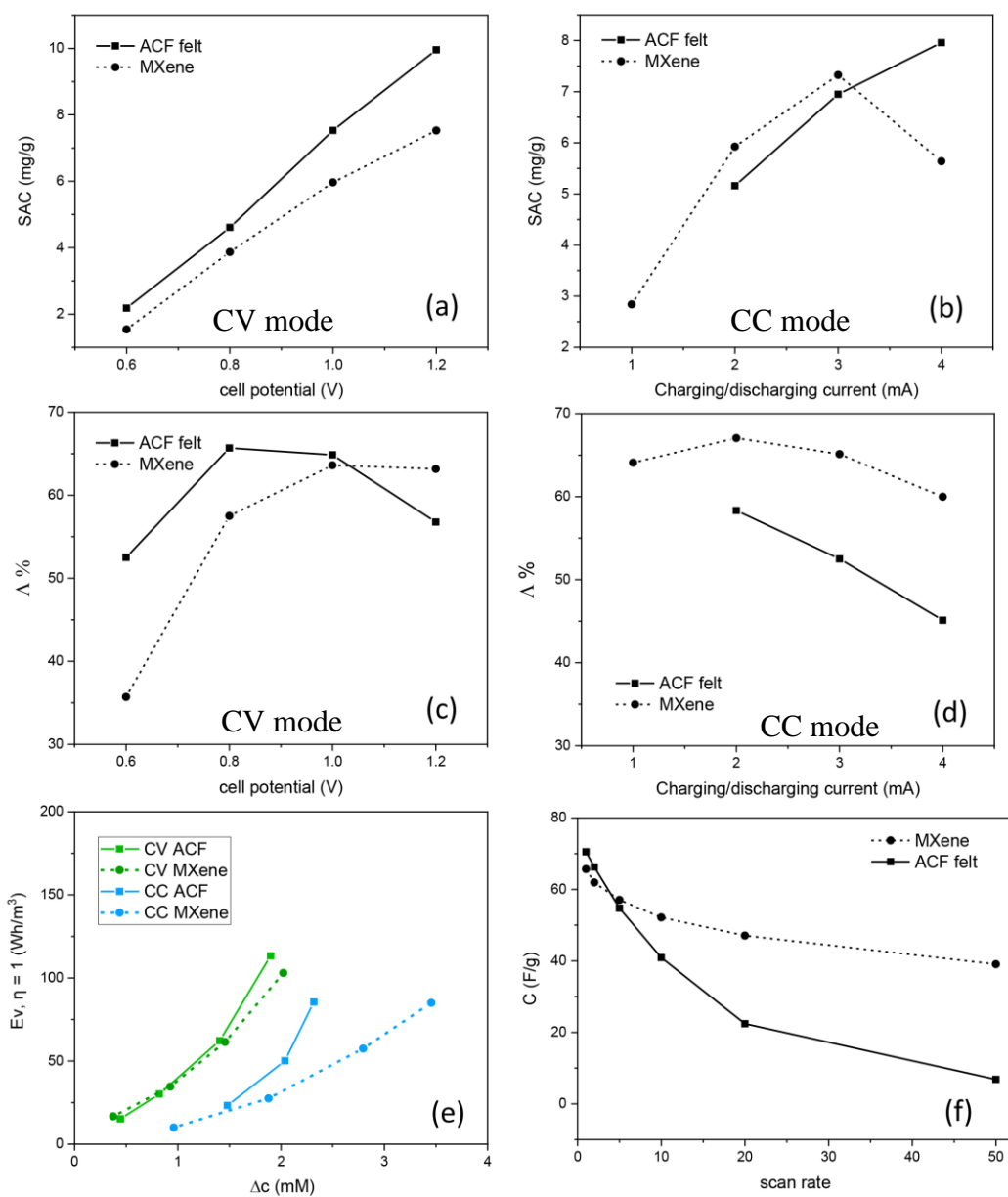
Figure 5.9 (a) SAC and (c) charge efficiency comparison between ACF felt and MXene
under CV mode. (b) SAC and (d) charge efficiency comparison between ACF felt and
MXene under CC mode. (e) Energy consumption comparison between ACF felt and
MXene. (f) Capacitances of ACF felt and MXene.

In comparison, the phenomenon that MXene cathode has better performance than ACF felt under constant current may be caused by three reasons: (1) MXene electrode has ion selectivity and only adsorb cations, thereby its charge efficiency is improved. (2) As the MXene electrode is very compact and thin (~40 µm), its resistance in the direction perpendicular to the electrode surface is very small. Therefore, the energy consumed by resistance is smaller for MXene electrode, compared with ACF electrode. (3) In constant voltage mode, the desalination rate of MXene is limited by the ion intercalation speed. Differently, in constant current mode, the applied constant current contributes to a constant ionic current in the cell, fitting the ion intercalation speed of MXene. This is also the reason why the advantage of ACF felt (faster desalination) disappears in constant current mode. This preliminary comparison between MXene and ACF illustrates that the employment of the intercalation material can decrease the energy consumption in constant current mode.

The capacitances of both electrodes are studied by CV method and the results are shown in Figure 5.7f. At slower scan rates, the capacitance of ACF felt is a little higher, while at scan rates higher than 10 mV/s, the capacitance of MXene is higher. The decrease of ACF felt capacitance over scan rate is caused by the resistance of the ACF felt while that of the MXene is caused by the intercalation speed of cations. In general, the MXene has similar capacitances with the ACF felt, contributing to their similar SACs under both constant current and constant voltage mode. On the other hand, the resistance of carbon-based materials can be further decreased by improving the fabrication forms. Thus, the performance of ACF can be further improved. In the future, other important experimental conditions, e.g. loading amount of electrode material, and different salt concentrations,

are of interest to be further considered to make a more comprehensive comparison between carbon-based material and intercalation material.

Chapter VI

Conclusions and perspectives

6.1 Conclusions

This thesis focuses on studying the degradation mechanism and improving the performance of carbon-based electrodes for CDI technology, considering that carbon-based materials hold the greatest potential to be wildly employed in commercialized CDI devices. The thesis studied carbon-based electrodes mainly from three aspects: (1) mechanism causing the stability degradation, (2) regeneration method to extend the electrode lifetime, and (3) performance improvement by modifying electrode fabrication process and employing intercalation material. Meantime, the theoretical model is employed to further understand the experimental results.

In chapter 3, the effect of trapped salt ions on CDI stability is studied. The results show that different concentrations of Na^+ and Cl^- in aged positive and negative electrodes are responsible for a significant part of the stability degradation. Furthermore, the trapped salt ions, which account for the loss in salt adsorption capacity, are metastable and under certain operating conditions may be released from the electrode surface. To demonstrate the role of salt ions in terms of stability degradation, we extend the classical Gouy-Chapman-Stern (GCS) double layer model and show the dynamic movement of salt ions schematically. This illustration can help to understand the stability degradation mechanism in a straightforward manner. Furthermore, a new method (offset-voltage test) is developed to simultaneously track the potential shift without changing the configuration of a two-terminal CDI cell. In this way, a thorough investigation of electrodes' potential shifts (due to metastable salt adsorption) during long-term operation is achieved. This

facile methodology contributes to both mechanism study and industrial operations of CDI system.

Chapter 4 demonstrates that the degraded performance of aged electrodes can be recovered through an industrially scalable method: thermal treatment. In this chapter, we investigate the SAC recovery and stability by modulating treatment temperature and ambient gas conditions. Through studying the nature of the surface functionalities and pore structure of the electrodes, we confirm that the acidic oxygen-containing groups formed in an anode during cycling can be precisely removed by thermal treatment at a moderate temperature (~500 °C), resulting in the regeneration of the aged electrode. We also employ the modified Donnan (mD) model to further quantify the surface charges originating from the formation and the decomposition of the oxygen-containing functional groups, directly demonstrating the impact of the decomposition of negative surface charges on the recovery of desalination performance.

In chapter 5, the CDI electrodes made from particle material by conventional fabrication method is compared with electrodes made from freestanding material. The results illustrate that the resistance of the electrode is significantly decreased in the compact electrode made by conventional fabrication method. Thus, its charge efficiency is improved and energy consumption is reduced, while the SAC keeps the same. The binder and conductive additives have neglected adverse effect on the performance of electrodes. Furthermore, the novel intercalation material (MXene) is compared with carbon-based material. The SACs of these two materials are similar under experimental conditions. Regarding to the energy consumption, MXene is more competitive than active carbon felt under constant current mode. This maybe because that MXene has ion

selectivity and high conductivity, thereby improving the charge efficiency. Therefore, the employment of the intercalation material can make CDI technology more energy efficient.

In conclusion, this thesis conducts a comprehensive study on carbon-based material for CDI technology. At the first, the effect of trapped salt ions on CDI stability is originally explored. The study makes a complementary to current electrode degradation theory and develops a new method to test active voltage. Secondly, a novel regeneration method is explored. This study not only proposes an industrial regeneration method, but also provides the rigorous scientific confirmation of the underlying mechanism, offering insights for minimizing electrode degradation and in-situ degradation regeneration. Lastly, different typical electrodes are compared. This is the first study which compares freestanding carbon material vs traditionally fabricated carbon material, and carbon material vs intercalation material under the same experimental condition. The result illustrates that the resistance and the ion-selectivity are two important considerations for electrode selection/fabrication. Overall, this thesis enhances the understanding of the degradation mechanism, and provides the method to extend the lifetime and to improve the performance of carbon-based electrode, making CDI technology more competitive for commercial application.

6.2 Future perspectives

At current stage, the majority of current study focuses on lab research of CDI technology (e.g., novel electrode materials and theoretical models). However, questions regarding to the real application of CDI technology lack of attention and exploration. In this section, several interesting and important future research directions are proposed to

further develop CDI technology. These directions are all relating to the scale-up of CDI technology, which are based on four questions: (1) Will the degradation rate change when scaling up the CDI facilities? (2) Is there any in-situ regeneration method? (3) How to balance productivity and charge efficiency for the electrode fabrication? (4) What will be the problems when employing CDI in treating real water? These four directions are discussed in details as follows.

(1) Factors affecting the degradation rate

Although the degradation mechanism of carbon-based electrode is well-explored by this study and others, there is a lack of study regarding the factors affecting the degradation rate. To specific, our CDI cell can be run for over one week in the conditions of 9×9 cm^2 electrode size, 100 mL 2 mM NaCl (tests in chapter 3), while the CDI cell can only be run for 2-3 days in the conditions of 3×3 cm^2 electrode size, 15 mL 10 mM NaCl (tests in chapter 4). The comparison implies that the lifetime of the electrode may be affected by factors such as electrolyte volume, electrolyte concentration, total salt amount, electrode loading amount and/or the ratio between water volume and electrode loading amount. Factors regarding to the degradation rate directly relates to the lifetime of the electrode. It could be a possibility that a larger loading amount of the electrode materials causes a longer lifetime of a CDI cell, in which case the stability degradation may not be a severe problem hindering the scalability of this technology. The question "how factors affect the degradation rate" is key to the industrial application of CDI technology, as well as the build-up of a pilot-scale CDI module for further academic study.

(2) In-situ regeneration methods

The regeneration mechanism of carbon-based electrode is well-elaborated and the regeneration method (thermal treatment) is proposed in this study. However, thermal treatment has some limitations: (1) electrodes need to be ex-situ heated. (2) not all the electrodes can tolerant the high temperatures (binders are used for electrodes made by particle materials). Therefore, in-situ regeneration methods are still of interest to be further explored. The studies in other fields, such as carbon community (regarding carbon reduction) and supercapacitor (regarding carbon surface modification), imply that carbon may be reduced by the chemicals, and the modification of carbon surface may reduce the oxidation rate of the anode. A simple method for in-situ regeneration can make CDI technology more competitive.

(3) The relationship between productivity and charge efficiency

The increase of the loading amount of electrode materials can increase the productivity of a single CDI device, but it also increases the electrode resistance, thereby decreasing the charge efficiency. Thus, it is important to find a balance between the productivity and the charge efficiency. However, there is a lack of study regarding to this question. The relationship between productivity and charge efficiency is also closely related to the fabrication form of the electrode. For example, a good woven form of activated carbon fiber may contribute to a large loading amount of electrode materials with a relatively low resistance. While many work developing advanced carbon materials focus on parameters such as pore structure and pore volume, the relationship between their loading amount (determining productivity) and the conductance (determining charge efficiency) may also affect the performance a lot. In another word, the fabrication form of

the materials may be another key consideration for judging the advanced electrode material.

(4) The application of CDI technology in treating real water

Although CDI technology are reported to be energy-efficient and cost-effective, there remain questions relating to its application in real water treatment. For example, the requirements of the inflow to CDI devices are unknown. The effect of some key water parameters (COD, BOD, suspended solids, etc.) on CDI performance deserves to be studied. In the condition that CDI cell is not sensitive to those contaminates, the application of this technology can be wider. Another question is that how to design a water treatment process employing CDI technology for a target water. The experimental study on treating real water can be very supportive and informative to the real application of CDI technology.

Appendix

A: Modification of carbon-based electrodes with gold nanoparticles

Gold nanoparticles (AuNP) may have some possible positive effect on carbon electrode: (1) increase the electrode conductivity, (2) change the carbon surface tension/potential and (3) cause some physical block to micropores, thus having the possibility to decrease the undesired metastable salt ions adsorption. Therefore, the effect of gold nanoparticles on carbon electrodes was studied. To coat carbon electrodes with AuNP, two ACF electrodes (2×2.5 cm^2) were saturated in 10 mL stirred gold colloid (gold nanoparticles of 5 nm diameter suspended in citrate buffer) for 5 days. Then, the desalination performance of pristine and modified electrodes was studied under the same conditions: electrolyte of 5 mL 10 mM NaCl, flow rate of 0.5 mL/min, and applied voltage of 1V(1h)/0V(1h).
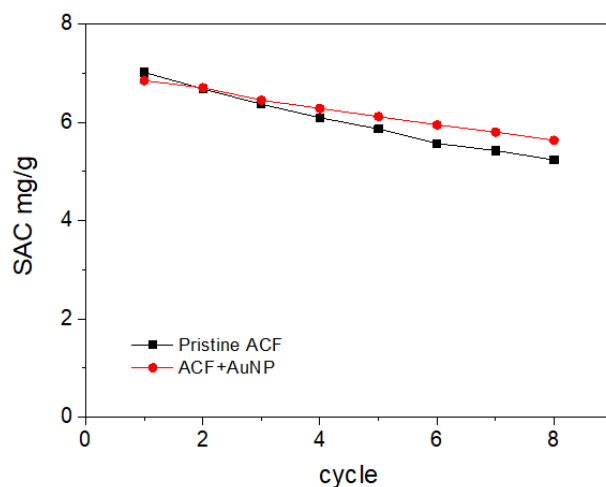
Figure A1 The SAC comparison between pristine ACF and ACF coated with AuNP

As shown in Figure A1, the SAC of AuNP-coated ACF is similar to that of pristine ACF, implying that coating AuNP has limited positive effect on ACF performance. The

difficulties in this experiment are: (1) AuNP has diameter of 5 nm, which is bigger than micropore diameter (<2 nm) of ACF, so maybe AuNP is too large to be used for modifying micropore carbon. (2) It is difficult to avoid AuNP aggregation and control their locations on carbon surface. Thus, the active coating amount of AuNP is unknown. (3) AuNP is stabilized in citrate buffer. Saturating ACF in AuNP may be an inefficient way to coat ACF with AuNP. From this preliminary experiment, we know that modifying ACF with AuNP by this proposed method is not a good modification method. The efficient modification method still needs to be further explored.

B: Performance study of a carbon nanotube electrode

Conventional CDI electrodes are the mixture of active material, conductive material and binder. The intrinsic drawback of this structure is that the conductive material and the binder may occupy the active sites of the active material. Carbon nanotubes (CNTs) own excellence in terms of mechanical, thermal and electrical properties. CNTs have great potential to be used as an additive material in CDI electrodes, working as supportive material and also increasing the conductivity of the composites. In this preliminary experiment, the performance of pure CNTs is explored. The CNT sheets were supplied by Prof. Choi (Seoul National University), fabricated by using the direct spinning method with a vertical-type chemical vapor deposition (CVD) apparatus. The surface morphology of pristine CNTs was characterized by scanning electron microscopy (SEM). The pristine CNT sheets were hydrophobic, so they were treated by an acid mixture of H_2SO_4 and HNO_3 at 55℃ (a-CNT) to improve the hydrophilicity before the CDI experiments. For CDI experiment, 6 ml 0.05 mM NaCl was used as the electrolyte. A normal cycle consists of 1-hour charging at 1.0V and 1-hour discharging at 0V.
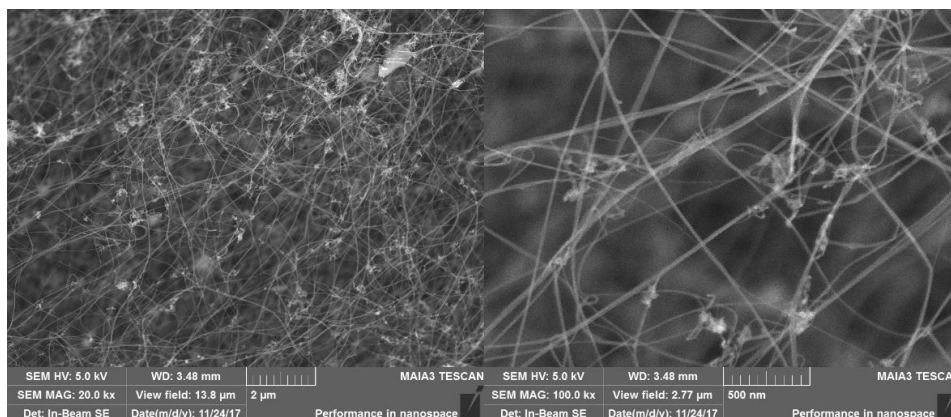
Figure B1. SEM images of CNTs in two different magnifications

Figure B1 shows the continuous and non-aligned structure of CNTs. This structure implies that the CNT sheet has a great potential to be used as a supportive and conductive materials for CDI electrode.
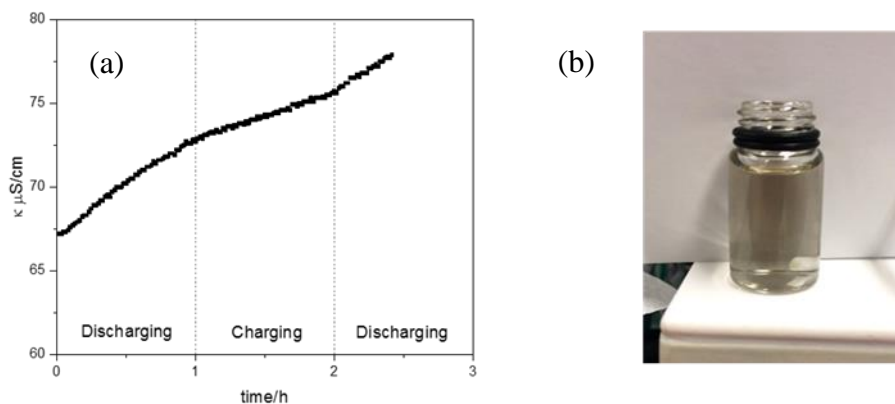
Figure B2. (a) Conductivity variation of a-CNT electrodes. (b) The water reservoir turns to grey after the cycling.

The Figure B2a shows that there is a clear slope change of the conductivity curve during charging phases. Probably, the slope change is caused by the desalination ability of a-CNT. However, its desalination ability is very small, and it does not cause an evident conductivity drop. This may be because that the material is pure CNTs without any active materials (e.g. activated carbon). Furthermore, the conductivity keeps increasing over time, and the water reservoir turns to grey after cycling, implying that CNTs are not stable and some CNTs are falling into the solution during cycling. These preliminary results indicate that CNTs are promising to be employed as supportive and conductive additive for carbon-based CDI electrodes. Before being employed, the falling problem of CNTs needs to be solved.

C: The regeneration study of inserting a Ti-mesh as a third electrode

The 3×3 cm^2 Ti mesh was employed as the third electrode and inserted between two electrodes. During normal CDI cycles, the voltage was applied on the anode and the cathode as usual (shown in Figure C1 a) in 100 mL 10 mM NaCl. The electrodes were first run for 20 normal cycles. After that, the DI water was pumped into the cell to wash the aged electrode until a conductivity of less than 5 µS/cm was reached at the outlet. The DI water keeps pumping during regeneration cycles. As shown in Figure C1 b, the reversed voltage was applied between the anode and the Ti mesh to try to regenerate the aged anode during regeneration cycles. The hypothesis is based on that the degradation of the performance is contributed by the gradual oxidation of the anode during cycling, leading to the formation of functional groups. Therefore, when the aged anode is connected as the cathode, reduction reactions of the formed functional groups may occur and the aged anode has the possibility to be reduced. The Ti mesh is employed as the counter electrode to avoid the oxidation of the carbon electrode. The regeneration ability of reversed voltages between 1 to 2 V with the interval of 0.2 V was studied and each voltage lasted for one hour. After that, 3 normal cycles were run to evaluate the performance of the electrodes after applying each regeneration voltage.
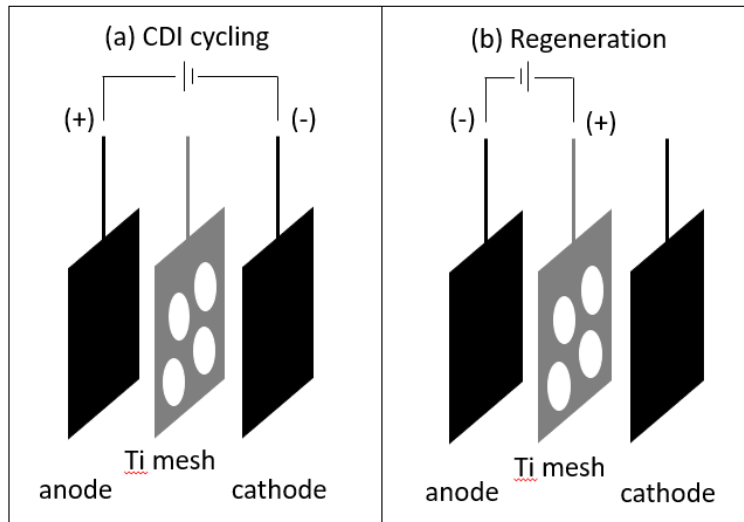
Figure C1. Demonstration of the regeneration experiment. (a) The voltage is applied on

the anode and the cathode during normal CDI cycles. (b) A reversed voltage is applied

on the previous anode and the Ti mesh electrode.
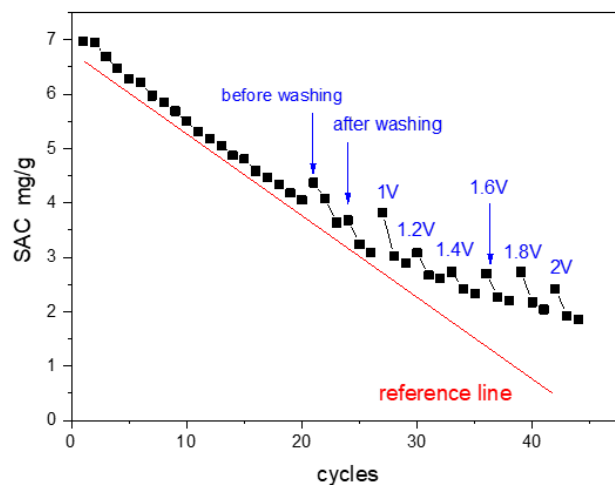
Figure C2. The regeneration study of inserting a Ti-mesh as a third electrode

The result of the regeneration study is shown in Figure C2. Generally, although the

SAC in the first cycle increases after applying the reversed voltages, the increase is small

and SAC in the following cycles decreases evidently. This result implies that the voltage

range of 1 to 2 V does not have evident regeneration ability under the experimental

condition. Better in-situ methods to reduce or regenerate the aged anode deserve to be

further explored.

References

1.   Dos Anjos, N. D. F. R., Source book of alternative technologies for freshwater augmentation in Latin America and the Caribbean. *International Journal of Water Resources Development* **1998,** *14*, (3), 365-398.

2.   Tang, S., Dual water supply in Hong Kong. **2000**.

3.   Tang, S.; Yue, D. P.; Ku, D. C., *Engineering and costs of dual water supply systems*. IWA publishing: 2007.

4.   Sadhwani, D.; Chau, J.; Loh, C.; Kilburn, M.; Lawson, A., Liquid assets: Water security and management in the Pearl River Basin and Hong Kong. *Hong Kong: Civic Exchange. Retrieved August* **2009,** *5*, 2010.

5.   Water supply and sanitation in Hong Kong.

6.   Voutchkov, N., *Desalination engineering: planning and design*. McGraw Hill Professional: 2012.

7.   Li, X.; Luk, S.; Tang, S., Sustainability of toilet flushing water supply in Hong Kong. *Water and Environment Journal* **2005,** *19*, (2), 85-90.

8.   Department, E. P. Sludge Treatment Facilities.

9.   Department, D. S., Yuen Long Sewage Treatment Works. In http://www.dsd.gov.hk/TC/Files/publications_publicity/publicity_materials/leaflets_booklets_factsheets/YLSTW.pdf.

10.   Tang, S.; Lee, T., Treatment of mixed (fresh and salt) wastewater. **2002**.

11.   Yue, D. P.; Tang, S., Sustainable strategies on water supply management in Hong Kong. *Water and Environment Journal* **2011,** *25*, (2), 192-199.

12.   AlMarzooqi, F. A.; Al Ghaferi, A. A.; Saadat, I.; Hilal, N., Application of capacitive deionisation in water desalination: a review. *Desalination* **2014,** *342*, 3-15.

13.   El-Dessouky, H. T.; Ettouney, H. M., *Fundamentals of salt water desalination*. Elsevier: 2002.

14.   Srimuk, P. Faradaic electrode materials for next-generation electrochemical water desalination. 2019.

15.   Maalouf, S. Planning and design of desalination plants effluent systems. UCLA, 2014.

16. Shenvi, S. S.; Isloor, A. M.; Ismail, A. F., A review on RO membrane technology: Developments and challenges. *Desalination* **2015,** *368*, 10-26.

17. Huehmer, R.; Lozier, J.; Henthorne, L.; Wang, F.; Lee, H.; Chan, C. In *Evaluation of conventional media and membrane SWRO pretreatment in Hong Kong, China*, IDA World Congress on Desalination and Water Reuse, Maspalomas, Gran Canaria, 2007; 2007.

18. Kong, L. C. o. H. Water conservation.

19. Water Supplies Department, T. G. o. H. K. S. Tseung Kwan O Desalination Plant Project.

20. Caudle, D. D., *Electrochemical demineralization of water with carbon electrodes*. US Dept. of the Interior;[for sale by the Superintendent of Documents, US …: 1966.

21. Bales, C.; Kovalsky, P.; Fletcher, J.; Waite, T. D., Low cost desalination of brackish groundwaters by Capacitive Deionization (CDI) – Implications for irrigated agriculture. *Desalination* **2019,** *453*, 37-53.

22. Caudill, L.; Omosebia, A.; Gao, X.; Landon, J.; Liu, K., In-situ Deaeration Towards Performance Stability of Capacitive Deionization Cells. *The Electrochemical Society* **2018**.

23. Dykstra, J. E.; Porada, S.; van der Wal, A.; Biesheuvel, P. M., Energy consumption in capacitive deionization - Constant current versus constant voltage operation. *Water Res* **2018,** *143*, 367-375.

24. Zhang, X.; Zuo, K.; Zhang, X.; Zhang, C.; Liang, P., Selective ion separation by capacitive deionization (CDI) based technologies: a state-of-the-art review. *Environmental Science: Water Research & Technology* **2020**.

25. Oren, Y., Capacitive deionization (CDI) for desalination and water treatment — past, present and future (a review). *Desalination* **2008,** *228*, (1-3), 10-29.

26. Tang, W.; Liang, J.; He, D.; Gong, J.; Tang, L.; Liu, Z.; Wang, D.; Zeng, G., Various cell architectures of capacitive deionization: Recent advances and future trends. *Water Res* **2018,** *150*, 225-251.

27.   Suss, M. E.; Porada, S.; Sun, X.; Biesheuvel, P. M.; Yoon, J.; Presser, V., Water desalination via capacitive deionization: what is it and what can we expect from it? *Energy & Environmental Science* **2015,** *8*, (8), 2296-2319.

28.   Welgemoed, T. J.; Schutte, C. F., Capacitive Deionization Technology™: An alternative desalination solution. *Desalination* **2005,** *183*, (1-3), 327-340.

29.   Farmer, J.; Fix, D.; Mack, G.; Pekala, R.; Poco, J., Capacitive deionization of NH 4 ClO 4 solutions with carbon aerogel electrodes. *Journal of applied electrochemistry* **1996,** *26*, (10), 1007-1018.

30.   Jande, Y.; Kim, W.-S., Predicting the lowest effluent concentration in capacitive deionization. *Separation and Purification Technology* **2013,** *115*, 224-230.

31.   Gao, X.; Omosebi, A.; Ma, Z.; Zhu, F.; Landon, J.; Ghorbanian, M.; Kern, N.; Liu, K., Capacitive deionization using symmetric carbon electrode pairs. *Environmental Science: Water Research & Technology* **2019,** *5*, (4), 660-671.

32.   Krüner, B.; Srimuk, P.; Fleischmann, S.; Zeiger, M.; Schreiber, A.; Aslan, M.; Quade, A.; Presser, V., Hydrogen-treated, sub-micrometer carbon beads for fast capacitive deionization with high performance stability. *Carbon* **2017,** *117*, 46-54.

33.   Qu, Y.; Campbell, P. G.; Hemmatifar, A.; Knipe, J. M.; Loeb, C. K.; Reidy, J. J.; Hubert, M. A.; Stadermann, M.; Santiago, J. G., Charging and Transport Dynamics of a Flow-Through Electrode Capacitive Deionization System. *J Phys Chem B* **2018,** *122*, (1), 240-249.

34.   Wang, L.; Dykstra, J. E.; Lin, S., Energy Efficiency of Capacitive Deionization. *Environ Sci Technol* **2019,** *53*, (7), 3366-3378.

35.   Wang, L.; Lin, S., Theoretical framework for designing a desalination plant based on membrane capacitive deionization. *Water Res* **2019,** *158*, 359-369.

36.   Gao, X.; Omosebi, A.; Landon, J.; Liu, K., Surface charge enhanced carbon electrodes for stable and efficient capacitive deionization using inverted adsorption–desorption behavior. *Energy & Environmental Science* **2015,** *8*, (3), 897-909.

37.   Gao, X.; Omosebi, A.; Landon, J.; Liu, K., Voltage-Based Stabilization of Microporous Carbon Electrodes for Inverted Capacitive Deionization. *The Journal of Physical Chemistry C* **2018,** *122*, (2), 1158-1168.

38.   Ma, J.; He, C.; He, D.; Zhang, C.; Waite, T. D., Analysis of capacitive and electrodialytic contributions to water desalination by flow-electrode CDI. *Water Res* **2018,** *144*, 296-303.

39.   Yang, F.; Ma, J.; Zhang, X.; Huang, X.; Liang, P., Decreased charge transport distance by titanium mesh-membrane assembly for flow-electrode capacitive deionization with high desalination performance. *Water Res* **2019,** *164*, 114904.

40.   Yoon, D. J.; Choi, J. H., A new standard metric describing the adsorption capacity of carbon electrode used in membrane capacitive deionization. *Water Res* **2019,** *148*, 126-132.

41.   Zhao, R.; Biesheuvel, P. M.; Miedema, H.; Bruning, H.; van der Wal, A., Charge Efficiency: A Functional Tool to Probe the Double-Layer Structure Inside of Porous Electrodes and Application in the Modeling of Capacitive Deionization. *The Journal of Physical Chemistry Letters* **2009,** *1*, (1), 205-210.

42.   Zhao, R.; Biesheuvel, P. M.; van der Wal, A., Energy consumption and constant current operation in membrane capacitive deionization. *Energy & Environmental Science* **2012,** *5*, (11).

43.   Li, B.; Zheng, T.; Ran, S.; Lee, P.-H.; Liu, B.; Boles, S. T., Role of metastable-adsorbed charges in the stability degradation of carbon-based electrodes for capacitive deionization. *Environmental Science: Water Research & Technology* **2018,** *4*, (8), 1172-1180.

44.   Li, B.; Zheng, T.; Ran, S.; Sun, M.; Shang, J.; Hu, H.; Lee, P. H.; Boles, S. T., Performance Recovery in Degraded Carbon-Based Electrodes for Capacitive Deionization. *Environ Sci Technol* **2020**.

45.   Jung, H.-H.; Hwang, S.-W.; Hyun, S.-H.; Lee, K.-H.; Kim, G.-T., Capacitive deionization characteristics of nanostructured carbon aerogel electrodes synthesized via ambient drying. *Desalination* **2007,** *216*, (1-3), 377-385.

46.   Xu, P.; Drewes, J. E.; Heil, D.; Wang, G., Treatment of brackish produced water using carbon aerogel-based capacitive deionization technology. *Water research* **2008,** *42*, (10-11), 2605-2617.

47.   Porada, S.; Weinstein, L.; Dash, R.; van der Wal, A.; Bryjak, M.; Gogotsi, Y.; Biesheuvel, P. M., Water desalination using capacitive deionization with microporous carbon electrodes. *ACS Appl Mater Interfaces* **2012,** *4*, (3), 1194-9.

48.   Li, H.; Zou, L.; Pan, L.; Sun, Z., Novel graphene-like electrodes for capacitive deionization. *Environmental science & technology* **2010,** *44*, (22), 8692-8697.

49.   Zhang, D.; Wen, X.; Shi, L.; Yan, T.; Zhang, J., Enhanced capacitive deionization of graphene/mesoporous carbon composites. *Nanoscale* **2012,** *4*, (17), 5440-5446.

50.   Li, L.; Zou, L.; Song, H.; Morris, G., Ordered mesoporous carbons synthesized by a modified sol–gel process for electrosorptive removal of sodium chloride. *Carbon* **2009,** *47*, (3), 775-781.

51.   Mayes, R. T.; Tsouris, C.; Kiggans Jr, J. O.; Mahurin, S. M.; DePaoli, D. W.; Dai, S., Hierarchical ordered mesoporous carbon from phloroglucinol-glyoxal and its application in capacitive deionization of brackish water. *Journal of Materials Chemistry* **2010,** *20*, (39), 8674-8678.

52.   Wimalasiri, Y.; Zou, L., Carbon nanotube/graphene composite for enhanced capacitive deionization performance. *Carbon* **2013,** *59*, 464-471.

53.   Chen, F.; Huang, Y.; Guo, L.; Sun, L.; Wang, Y.; Yang, H. Y., Dual-ions electrochemical deionization: a desalination generator. *Energy & Environmental Science* **2017,** *10*, 2081--2089.

54.   Yu, F.; Wang, L.; Wang, Y.; Shen, X.; Cheng, Y.; Ma, J., Faradaic Reactions in Capacitive Deionization for Desalination and Ion Separation. *Journal of Materials Chemistry A* **2019**.

55.   Kim, S.; Yoon, H.; Shin, D.; Lee, J.; Yoon, J., Electrochemical selective ion separation in capacitive deionization with sodium manganese oxide. *Journal of colloid and interface science* **2017,** *506*, 644-648.

56.   Ding, Z.; Xu, X.; Li, Y.; Wang, K.; Lu, T.; Pan, L., Significantly improved stability of hybrid capacitive deionization using nickel hexacyanoferrate/reduced graphene oxide cathode at low voltage operation. *Desalination* **2019,** *468*, 114078.

57.   Porada, S.; Shrivastava, A.; Bukowska, P.; Biesheuvel, P.; Smith, K. C., Nickel hexacyanoferrate electrodes for continuous cation intercalation desalination of brackish water. *Electrochimica Acta* **2017,** *255*, 369-378.

58.   Malik, R., Maxing out water desalination with MXenes. *Joule* **2018,** *2*, (4), 591-593.

59.   Guo, L.; Wang, X.; Leong, Z. Y.; Mo, R.; Sun, L.; Yang, H. Y., Ar plasma modification of 2D MXene Ti3C2Tx nanosheets for efficient capacitive desalination. *FlatChem* **2018,** *8*, 17-24.

60.   Lee, J.; Kim, S.; Kim, C.; Yoon, J., Hybrid capacitive deionization to enhance the desalination performance of capacitive techniques. *Energy & Environmental Science* **2014,** *7*, (11), 3683-3689.

61.   Xing, W.; Liang, J.; Tang, W.; He, D.; Yan, M.; Wang, X.; Luo, Y.; Tang, N.; Huang, M., Versatile applications of capacitive deionization (CDI)-based technologies. *Desalination* **2020,** *482*.

62.   Porada, S.; Zhao, R.; van der Wal, A.; Presser, V.; Biesheuvel, P. M., Review on the science and technology of water desalination by capacitive deionization. *Progress in Materials Science* **2013,** *58*, (8), 1388-1442.

63.   Voltea company.

64.   EST company.

65.   CDI international conference 2019.

66.   Tsouris, C.; Mayes, R.; Kiggans, J.; Sharma, K.; Yiacoumi, S.; DePaoli, D.; Dai, S., Mesoporous carbon for capacitive deionization of saline water. *Environ Sci Technol* **2011,** *45*, (23), 10243-9.

67.   Cohen, I.; Avraham, E.; Bouhadana, Y.; Soffer, A.; Aurbach, D., Long term stability of capacitive de-ionization processes for water desalination: The challenge of positive electrodes corrosion. *Electrochimica Acta* **2013,** *106*, 91-100.

68.   Cohen, I.; Avraham, E.; Bouhadana, Y.; Soffer, A.; Aurbach, D., The effect of the flow-regime, reversal of polarization, and oxygen on the long term stability in capacitive de-ionization processes. *Electrochimica Acta* **2015,** *153*, 106-114.

69.   He, D.; Wong, C. E.; Tang, W.; Kovalsky, P.; Waite, T. D., Faradaic Reactions in Water Desalination by Batch-Mode Capacitive Deionization. *Environmental Science & Technology Letters* **2016,** *3*, (5), 222-226.

70.   Tang, W.; He, D.; Zhang, C.; Kovalsky, P.; Waite, T. D., Comparison of Faradaic reactions in capacitive deionization (CDI) and membrane capacitive deionization (MCDI) water treatment processes. *Water Res* **2017,** *120*, 229-237.

71.   Zhang, W.; Mossad, M.; Zou, L., A study of the long-term operation of capacitive deionisation in inland brackish water desalination. *Desalination* **2013,** *320*, 80-85.

72.   Hawks, S. A.; Ramachandran, A.; Porada, S.; Campbell, P. G.; Suss, M. E.; Biesheuvel, P. M.; Santiago, J. G.; Stadermann, M., Performance metrics for the objective assessment of capacitive deionization systems. *Water Res* **2019,** *152*, 126-137.

73.   Huang, Z.-H.; Wang, M.; Wang, L.; Kang, F., Relation between the charge efficiency of activated carbon fiber and its desalination performance. *Langmuir* **2012,** *28*, (11), 5079-5084.

74.   Aslan, M.; Zeiger, M.; Jackel, N.; Grobelsek, I.; Weingarth, D.; Presser, V., Improved capacitive deionization performance of mixed hydrophobic/hydrophilic activated carbon electrodes. *J Phys Condens Matter* **2016,** *28*, (11), 114003.

75.   Hamann, C. H.; Hamnett, A.; Vielstich, W., *Electrochemistry*. Wiley: 1998.

76.   Bard, A. J.; Faulkner, L. R., ELECTROCHEMICAL METHODS Fundamentals and Applications. **2001**.

77.   Grahame, D. C., The electrical double layer and the theory of electrocapillarity. *Chemical reviews* **1947,** *41*, (3), 441-501.

78.   Biesheuvel, P., Activated carbon is an electron-conducting amphoteric ion adsorbent. *arXiv preprint arXiv:1509.06354* **2015**.

79.   He, F.; Biesheuvel, P. M.; Bazant, M. Z.; Hatton, T. A., Theory of water treatment by capacitive deionization with redox active porous electrodes. *Water Res* **2018,** *132*, 282-291.

80.   Suss, M. E.; Biesheuvel, P. M.; Baumann, T. F.; Stadermann, M.; Santiago, J. G., In situ spatially and temporally resolved measurements of salt concentration between

charging porous electrodes for desalination by capacitive deionization. *Environ Sci Technol* **2014,** *48*, (3), 2008-15.

81.   Biesheuvel, P. M.; Fu, Y.; Bazant, M. Z., Diffuse charge and Faradaic reactions in porous electrodes. *Phys Rev E Stat Nonlin Soft Matter Phys* **2011,** *83*, (6 Pt 1), 061507.

82.   Biesheuvel, P. M.; Zhao, R.; Porada, S.; van der Wal, A., Theory of membrane capacitive deionization including the effect of the electrode pore space. *J Colloid Interface Sci* **2011,** *360*, (1), 239-48.

83.   Biesheuvel, P. M.; Hamelers, H. V. M.; Suss, M. E., Theory of Water Desalination by Porous Electrodes with Immobile Chemical Charge. *Colloids and Interface Science Communications* **2015,** *9*, 1-5.

84.   Biesheuvel, P.; Van Limpt, B.; Van der Wal, A., Dynamic adsorption/desorption process model for capacitive deionization. *The journal of physical chemistry C* **2009,** *113*, (14), 5636-5640.

85.   Mizoguchi, H.; Ueda, K.; Orita, M.; Moon, S.-C.; Kajihara, K.; Hirano, M.; Hosono, H., Decomposition of water by a CaTiO3 photocatalyst under UV light irradiation. *Materials Research Bulletin* **2002,** *37*, (15), 2401-2406.

86.   Jeon, S.-i.; Park, H.-r.; Yeo, J.-g.; Yang, S.; Cho, C. H.; Han, M. H.; Kim, D. K., Desalination via a new membrane capacitive deionization process utilizing flow-electrodes. *Energy & Environmental Science* **2013,** *6*, (5).

87.   Ma, J.; He, D.; Tang, W.; Kovalsky, P.; He, C.; Zhang, C.; Waite, T. D., Development of Redox-Active Flow Electrodes for High-Performance Capacitive Deionization. *Environ Sci Technol* **2016,** *50*, (24), 13495-13501.

88.   Shi, W.; Zhou, X.; Li, J.; Meshot, E. R.; Taylor, A. D.; Hu, S.; Kim, J.-H.; Elimelech, M.; Plata, D. L., High-Performance Capacitive Deionization via Manganese Oxide-Coated, Vertically Aligned Carbon Nanotubes. *Environmental Science & Technology Letters* **2018,** *5*, (11), 692-700.

89.   Porada, S.; Borchardt, L.; Oschatz, M.; Bryjak, M.; Atchison, J. S.; Keesman, K. J.; Kaskel, S.; Biesheuvel, P. M.; Presser, V., Direct prediction of the desalination performance of porous carbon electrodes for capacitive deionization. *Energy & Environmental Science* **2013,** *6*, (12), 3700-3712.

90.   Duan, F.; Du, X.; Li, Y.; Cao, H.; Zhang, Y., Desalination stability of capacitive deionization using ordered mesoporous carbon: Effect of oxygen-containing surface groups and pore properties. *Desalination* **2015,** *376*, 17-24.

91.   Qu, Y.; Baumann, T. F.; Santiago, J. G.; Stadermann, M., Characterization of Resistances of a Capacitive Deionization System. *Environ Sci Technol* **2015,** *49*, (16), 9699-706.

92.   Gao, X.; Omosebi, A.; Holubowitch, N.; Landon, J.; Liu, K., Capacitive Deionization Using Alternating Polarization: Effect of Surface Charge on Salt Removal. *Electrochimica Acta* **2017,** *233*, 249-255.

93.   Gao, X.; Omosebi, A.; Landon, J.; Liu, K., Dependence of the Capacitive Deionization Performance on Potential of Zero Charge Shifting of Carbon Xerogel Electrodes during Long-Term Operation. *Journal of The Electrochemical Society* **2014,** *161*, (12), E159-E166.

94.   Wang, L.; Lin, S., Membrane Capacitive Deionization with Constant Current vs Constant Voltage Charging: Which Is Better? *Environ Sci Technol* **2018,** *52*, (7), 4051-4060.

95.   Wang, L.; Lin, S., Mechanism of Selective Ion Removal in Membrane Capacitive Deionization for Water Softening. *Environmental Science & Technology* **2019,** *53*, (10), 5797-5804.

96.   Suss, M. E.; Baumann, T. F.; Bourcier, W. L.; Spadaccini, C. M.; Rose, K. A.; Santiago, J. G.; Stadermann, M., Capacitive desalination with flow-through electrodes. *Energy & Environmental Science* **2012,** *5*, (11).

97.   Biesheuvel, P. M.; Porada, S.; Levi, M.; Bazant, M. Z., Attractive forces in microporous carbon electrodes for capacitive deionization. *Journal of Solid State Electrochemistry* **2014,** *18*, (5), 1365-1376.

98.   Srimuk, P.; Ries, L.; Zeiger, M.; Fleischmann, S.; Jäckel, N.; Tolosa, A.; Krüner, B.; Aslan, M.; Presser, V., High performance stability of titania decorated carbon for desalination with capacitive deionization in oxygenated water. *RSC Advances* **2016,** *6*, (108), 106081-106089.

99.   Tang, W.; Kovalsky, P.; He, D.; Waite, T. D., Fluoride and nitrate removal from brackish groundwaters by batch-mode capacitive deionization. *Water research* **2015,** *84*, 342-349.

100.   Ma, D.; Wang, Y.; Han, X.; Xu, S.; Wang, J., Electrode configuration optimization of capacitive deionization cells based on zero charge potential of the electrodes. *Separation and Purification Technology* **2017,** *189*, 467-474.

101.   Zhang, C.; He, D.; Ma, J.; Tang, W.; Waite, T. D., Faradaic reactions in capacitive deionization (CDI) - problems and possibilities: A review. *Water Res* **2018,** *128*, 314-330.

102.   Cohen, I.; Avraham, E.; Noked, M.; Soffer, A.; Aurbach, D., Enhanced Charge Efficiency in Capacitive Deionization Achieved by Surface-Treated Electrodes and by Means of a Third Electrode. *The Journal of Physical Chemistry C* **2011,** *115*, (40), 19856-19863.

103.   Gao, X.; Omosebi, A.; Landon, J.; Liu, K., Enhanced salt removal in an inverted capacitive deionization cell using amine modified microporous carbon cathodes. *Environmental science & technology* **2015,** *49*, (18), 10920-10926.

104.   Lee, J.-H.; Bae, W.-S.; Choi, J.-H., Electrode reactions and adsorption/desorption performance related to the applied potential in a capacitive deionization process. *Desalination* **2010,** *258*, (1-3), 159-163.

105.   Farmer, J. C.; Fix, D. V.; Mack, G. V.; Pekala, R. W.; Poco, J. F., Capacitive Deionization of NaCI and NaNO3 Solutions with Carbon Aerogel Electrodes. *J Electrochem. Soc.* **1996,** *143*, 159-169.

106.   Kinoshita, K., Carbon: electrochemical and physicochemical properties. **1988**.

107.   Haro, M.; Rasines, G.; Macias, C.; Ania, C., Stability of a carbon gel electrode when used for the electro-assisted removal of ions from brackish water. *Carbon* **2011,** *49*, (12), 3723-3730.

108.   Bouhadana, Y.; Avraham, E.; Noked, M.; Ben-Tzion, M.; Soffer, A.; Aurbach, D., Capacitive deionization of NaCl solutions at non-steady-state conditions: inversion functionality of the carbon electrodes. *The Journal of Physical Chemistry C* **2011,** *115*, (33), 16567-16573.

109.   Gao, X.; Porada, S.; Omosebi, A.; Liu, K.-L.; Biesheuvel, P.; Landon, J., Complementary surface charge for enhanced capacitive deionization. *Water research* **2016,** *92*, 275-282.

110.   Wu, T.; Wang, G.; Zhan, F.; Dong, Q.; Ren, Q.; Wang, J.; Qiu, J., Surface-treated carbon electrodes with modified potential of zero charge for capacitive deionization. *Water Res* **2016,** *93*, 30-37.

111.   Avraham, E.; Noked, M.; Cohen, I.; Soffer, A.; Aurbach, D., The dependence of the desalination performance in capacitive deionization processes on the electrodes PZC. *Journal of The Electrochemical Society* **2011,** *158*, (12), P168-P173.

112.   Omosebi, A.; Gao, X.; Landon, J.; Liu, K., Asymmetric electrode configuration for enhanced membrane capacitive deionization. *ACS applied materials & interfaces* **2014,** *6*, (15), 12640-12649.

113.   Hawks, S. A.; Ceron, M. R.; Oyarzun, D. I.; Pham, T. A.; Zhan, C.; Loeb, C. K.; Mew, D.; Deinhart, A.; Wood, B. C.; Santiago, J. G.; Stadermann, M.; Campbell, P. G., Using Ultramicroporous Carbon for the Selective Removal of Nitrate with Capacitive Deionization. *Environ Sci Technol* **2019,** *53*, (18), 10863-10870.

114.   Guyes, E. N.; Malka, T.; Suss, M. E., Enhancing the Ion-Size-Based Selectivity of Capacitive Deionization Electrodes. *Environ Sci Technol* **2019,** *53*, (14), 8447-8454.

115.   Suss, M. E.; Presser, V., Water Desalination with Energy Storage Electrode Materials. *Joule* **2018,** *2*, (1), 10-15.

116.   Zhang, C.; He, D.; Ma, J.; Tang, W.; Waite, T. D., Comparison of faradaic reactions in flow-through and flow-by capacitive deionization (CDI) systems. *Electrochimica Acta* **2019,** *299*, 727-735.

117.   Jankowska, H.; Świątkowski, A.; Choma, J., *Active carbon*. Ellis Horwood Ltd: 1991.

118.   Shafeeyan, M. S.; Daud, W. M. A. W.; Houshmand, A.; Shamiri, A., A review on surface modification of activated carbon for carbon dioxide adsorption. *Journal of Analytical and Applied Pyrolysis* **2010,** *89*, (2), 143-151.

119.   Agartan, L.; Akuzum, B.; Mathis, T.; Ergenekon, K.; Agar, E.; Caglan Kumbur, E., Influence of thermal treatment conditions on capacitive deionization performance

and charge efficiency of carbon electrodes. *Separation and Purification Technology* **2018,** *202*, 67-75.

120.   Kwiatkowski, J. F., *Activated carbon: classifications, properties and applications*. Nova Science Publishers, Incorporated: 2011.

121.   Boehm, H. P., Chemical Identification of Surface Groups. In 1966; pp 179-274.

122.   Goertzen, S. L.; Thériault, K. D.; Oickle, A. M.; Tarasuk, A. C.; Andreas, H. A., Standardization of the Boehm titration. Part I. CO2 expulsion and endpoint determination. *Carbon* **2010,** *48*, (4), 1252-1261.

123.   Oickle, A. M.; Goertzen, S. L.; Hopper, K. R.; Abdalla, Y. O.; Andreas, H. A., Standardization of the Boehm titration: Part II. Method of agitation, effect of filtering and dilute titrant. *Carbon* **2010,** *48*, (12), 3313-3322.

124.   Shapira, B.; Avraham, E.; Aurbach, D., Side Reactions in Capacitive Deionization (CDI) Processes: The Role of Oxygen Reduction. *Electrochimica Acta* **2016,** *220*, 285-295.

125.   Chen, Z.; Zhang, H.; Yang, C.; Sun, X.; Guo, H.; Wu, C.; Xue, F.; Gao, L., Effects of ageing and incorporation of ion-exchange membrane on the electrosorption performance of activated carbon based electrodes modules. *Desalination and Water Treatment* **2013,** *51*, (16-18), 3489-3496.

126.   Nian, Y.-R.; Teng, H., Influence of surface oxides on the impedance behavior of carbonbased electrochemical capacitors. *Journal of Electroanalytical Chemistry* **2003,** *540*, 119-127.

127.   Kundu, S.; Wang, Y.; Xia, W.; Muhler, M., Thermal Stability and Reducibility of Oxygen-Containing Functional Groups on Multiwalled Carbon Nanotube Surfaces: A Quantitative High-Resolution XPS and TPD/ TPR Study. *J. Phys. Chem. C* **2008,** *112*, 16869–16878.

128.   Hemmatifar, A.; Oyarzun, D. I.; Palko, J. W.; Hawks, S. A.; Stadermann, M.; Santiago, J. G., Equilibria model for pH variations and ion adsorption in capacitive deionization electrodes. *Water research* **2017,** *122*, 387-397.

129.   Holubowitch, N.; Omosebi, A.; Gao, X.; Landon, J.; Liu, K., Quasi-steady-state polarization reveals the interplay of capacitive and faradaic processes in capacitive deionization. *ChemElectroChem* **2017,** *4*, (9), 2404-2413.

130.   Compton, O. C.; Nguyen, S. T., Graphene oxide, highly reduced graphene oxide, and graphene: versatile building blocks for carbon-based materials. *Small* **2010,** *6*, (6), 711-23.

131.   Park, S.; Ruoff, R. S., Chemical methods for the production of graphenes. *Nat Nanotechnol* **2009,** *4*, (4), 217-24.

132.   Huang, Z.-H.; Yang, Z.; Kang, F.; Inagaki, M., Carbon electrodes for capacitive deionization. *Journal of Materials Chemistry A* **2017,** *5*, (2), 470-496.

133.   Simoncelli, M.; Ganfoud, N.; Sene, A.; Haefele, M.; Daffos, B.; Taberna, P.-L.; Salanne, M.; Simon, P.; Rotenberg, B., Blue Energy and Desalination with Nanoporous Carbon Electrodes: Capacitance from Molecular Simulations to Continuous Models. *PHYSICAL REVIEW X* **2018,** *8*, (2), 2160-3308.

134.   Wei, X.; Jiang, X.; Wei, J.; Gao, S., Functional Groups and Pore Size Distribution Do Matter to Hierarchically Porous Carbons as High-Rate-Performance Supercapacitors. *Chemistry of Materials* **2016,** *28*, (2), 445-458.

135.   Ryoo, M.-W.; Seo, G., Improvement in capacitive deionization function of activated carbon cloth by titania modification. *Water Research* **2003,** *37*, (7), 1527-1534.

136.   Shim, J.-W.; Park, S.-J.; Ryu, S.-K., Effect of modification with HNO3 and NaOH on metal adsorption by pitch-based activated carbon fibers. *Carbon* **2001,** *39*, (11), 1635-1642.

137.   Chen, F.; Huang, Y.; Guo, L.; Ding, M.; Yang, H. Y., A dual-ion electrochemistry deionization system based on AgCl-Na0.44MnO2 electrodes. *Nanoscale* **2017,** *9*, (28), 10101-10108.

138.   Kuraray company.

139.   Srimuk, P.; Halim, J.; Lee, J.; Tao, Q.; Rosen, J.; Presser, V., Two-dimensional molybdenum carbide (MXene) with divacancy ordering for brackish and seawater desalination via cation and anion intercalation. *ACS Sustainable Chemistry & Engineering* **2018,** *6*, (3), 3739-3747.

140.   Singh, K.; Porada, S.; de Gier, H. D.; Biesheuvel, P. M.; de Smet, L. C. P. M., Timeline on the application of intercalation materials in Capacitive Deionization. *Desalination* **2019,** *455*, 115-134.

141.   Rassat, S. D.; Sukamto, J. H.; Orth, R. J.; Lilga, M. A.; Hallen, R. T., Development of an electrically switched ion exchange process for selective ion separations. *Separation and purification technology* **1999,** *15*, (3), 207-222.

142.   Liu, S.; Smith, K. C., Quantifying the trade-offs between energy consumption and salt removal rate in membrane-free cation intercalation desalination. *Electrochimica Acta* **2018,** *271*, 652-665.

143.   Lukatskaya, M. R.; Mashtalir, O.; Ren, C. E.; Dall'Agnese, Y.; Rozier, P.; Taberna, P. L.; Naguib, M.; Simon, P.; Barsoum, M. W.; Gogotsi, Y., Cation Intercalation and High Volumetric Capacitance of Two-Dimensional Titanium Carbide. *science advances* **2018,** *341*, 1502-10505.

144.   Bao, W.; Tang, X.; Guo, X.; Choi, S.; Wang, C.; Gogotsi, Y.; Wang, G., Porous Cryo-Dried MXene for Efficient Capacitive Deionization. *Joule* **2018,** *2*, (4), 778-787.

145.   Srimuk, P.; Kaasik, F.; Krüner, B.; Tolosa, A.; Fleischmann, S.; Jäckel, N.; Tekeli, M. C.; Aslan, M.; Suss, M. E.; Presser, V., MXene as a novel intercalation-type pseudocapacitive cathode and anode for capacitive deionization. *Journal of Materials Chemistry A* **2016,** *4*, (47), 18265-18271.

146.   Hu, H.; Hua, T., An easily manipulated protocol for patterning of MXenes on paper for planar micro-supercapacitors. *Journal of Materials Chemistry A* **2017,** *5*, (37), 19639-19648.

147.   Wang, G.; Dong, Q.; Wu, T.; Zhan, F.; Zhou, M.; Qiu, J., Ultrasound-assisted preparation of electrospun carbon fiber/graphene electrodes for capacitive deionization: Importance and unique role of electrical conductivity. *Carbon* **2016,** *103*, 311-317.

148.   Porada, S.; Bryjak, M.; van der Wal, A.; Biesheuvel, P. M., Effect of electrode thickness variation on operation of capacitive deionization. *Electrochimica Acta* **2012,** *75*, 148-156.